Magneto-transport and Photoresponse of 2D Semimetals

Zaiyao Fei

A dissertation
submitted in partial fulfillment of the
requirements for the degree of

Doctor of Philosophy

University of Washington

2017

Reading Committee:

David H. Cobden, Chair

Xiaodong Xu

Anton Andreev

Program Authorized to Offer Degree:
Department of Physics

University of Washington

Abstract

Magneto-transport and Photoresponse of 2D Semimetals

Zaiyao Fei

Chair of the Supervisory Committee:
Professor David H. Cobden
Department of Physics

A semimetal is a material with a small overlap between the bottom of the conduction band and the top of the valence band. Near the Fermi level, the density of state is almost negligible. Thus, in the two dimensional limit, the carrier densities can be substantially modulated by applying an electrostatic gate, affording new opportunities for tuning the electronic states as well as potential applications in next generation transistors and optoelectronics. On the other hand, the carrier mobilities in these 2D semimetals are usually extremely high, enabling observations of various quantum phenomena, such as the quantum Hall effect.

In this thesis, two 2D semimetals, graphene and single layer tungsten ditelluride (WTe_2), will be explored through optical and magneto-transport techniques. In the first part, we will introduce the discovery of a new type of photocurrent generated by the photo Nernst effect in graphene in both classical and quantum regimes. By generalizing the Song-Levitov result of the long-range photocurrent response to the case of non-vanishing magnetic field on strip shape devices, we were able to formulate the photocurrent and capture almost all features observed in the experiment. Thereafter, we will turn to the other semimetal, WTe_2, which was recently found to be a rich system, hosting a lot of exotic phenomena and interesting theoretic predictions, such as large magnetoresistance, type-II Weyl points, pressure driven supercon-

ductivity and nontrivial topology. Through investigating the generic magneto-transport properties of WTe_2 to the single layer limit, we discovered that the monolayer is likely a quantum spin Hall insulator near charge neutrality, while displays superconductivity for large electrostatic doping at sub-Kelvin temperatures.

TABLE OF CONTENTS

LIST OF FIGURES

LIST OF TABLES

ACKNOWLEDGMENTS

PhD life is a long journey and never easy, but is also fruitful. Looking back, I feel so lucky that I can meet so many nice people, without whom I would never be able to come to this point.

First and foremost, I would like to thank my advisor, Prof. David Cobden, who has always been so nice, responsible, encouraging and patient throughout my Ph.D. I am always impressed by his serious attitude towards science, which has been reflected for so many times by his masterpieces. The way he picks a project, approaches a difficult problem, plays with it, and never satisfies with what he has already learned are the most important legacies of my Ph.D. He is never tired of teaching me how to think as a scientist, suggesting me not to be bothered by some "noisy" results. I will never forget that he even came to the lab and supervised me the day before a Christmas Eve when we discovered something really exciting in monolayer WTe_2. I feel so grateful to have the opportunity to work in his lab.

Besides my advisor, I would like to thank Prof. Xiaodong Xu. There have been so many successful collaborations between our lab and the Xu lab. He is so enthusiastic, knowledgeable and is always ready to answer all my questions. It happened several times that when we were trying to figure out something new, and suddenly we realized Xiaodong had already published a paper on the same subject. He is also very responsible and supportive for my research. I do remember there are many times when I was performing measurements in the lab all by myself close to midnight, then Xiaodong came in (before he left for home), asked the progresses and gave me a lot of insightful ideas. I didn't feel alone during that time.

I am grateful to Prof. Anton Andreev. Whenever I had some theoretical questions, the first name came into my mind was always Anton. He knows "everything" and is so kind

and easy to communicate with. I would also like to extend my gratitude to other committee members, Prof. Jason Detwiler and Prof. Guozhong Cao. You are the best and most responsible committee members I've ever met.

I would like to thank all members from our lab and Xu's lab, past and present, including undergrads, graduates and postdocs. Sanfeng, how many times have we talked about physics in the restaurants on the Ave while waiting for food? Tauno, thank you for making the Oxford cryostat running again and kindly checking typos in my thesis; Wenjin, thank you for your hard work on the fabrication, I can't remember how many times we failed before we can finally make reliable pre-patterned metal contacts on hBN; Joe, you are the smartest undergrad I have met, thank you for working with me; Thanks to Boris Dzyubenko, Bosong Sun, Paul Nguyen, Joshua Kahn, Moira Miler, Dr. Talip Serkan Kasirga, Dr. Jae Park, Dr. Hao-Chun Lee, Dr. Chunming Huang, Stephen French, Xiao Lu, Dr. Xinghan Cai, Pasqual Rivera, Kyle Seyler, Genevieve Clark, Ding Zhong, Bevin Huang, Nathen Wilson, Tiancheng Song, Chenfeng Du, Dr. Helin Cao, Dr. Jason Ross etc, without you research and life would be much harder.

A special gratitude goes out to all our collaborators for their excellent work: Dr. Jiaqiang Yan and Dr. David Mandrus provided the WTe_2 crystals; Dr. Takashi Taniguchi and Dr. Kenji Watanabe provided the high quality hBN crystals; Dr. Yongtao Cui performed the scanning microwave impedance measurements; Ebrahim Sajadi and Prof. Joshua Folk conducted the ultra low temperature measurements on WTe_2; Prof. Di Xiao and Prof. Boris Spivak provided insightful theoretical guidances. Without them, most projects cannot be finished.

My sincere thanks go to all my friends in Seattle. Thanks for all sorts of games, parties, hiking, and travelings we did together, without you life would be much boring especially during the rainy seasons of Seattle.

Lastly, I want to thank my parents and my elder sister. Although I would call them and

talk to them every weekend, they are still worried about me and keep reminding me to stay safe when I am about to hang up. Thank you for your endless support.

DEDICATION

To my parents Zhangbao Fei and Xinglan Dai

Chapter 1

INTRODUCTION TO 2D ELECTRON GAS

1.1 Classical two dimensional electron gas

A two-dimensional electron gas (2DEG) is a gas of electrons free to move in two dimensions but are confined in the third dimension. Because of the quantum effect, energy levels in that direction are quantized, leading to a lot of interesting physical properties and potential applications of smaller and faster electronics.

The most common 2DEG is found in Si-MOSFETs. Figure 1.1a is an example of a typical NPN MOSFET. When the transistor is working in the inversion mode after applying a gate voltage (Fig. 1.1b), electrons underneath the oxide are confined to the semiconductor-oxide interface but are free to move within the interface, forming the 2DEG.

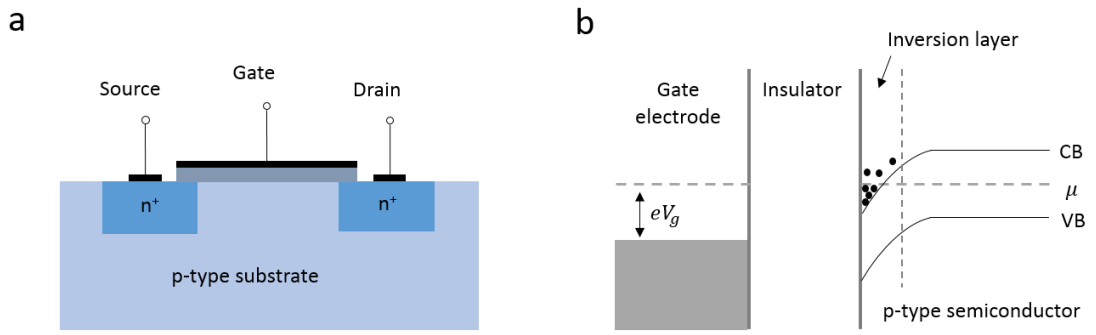

Figure 1.1: a, Cross section of a typical NPN Si-MOSFET structure. b, Band diagram of Si-MOSFET in inversion mode when $V_g > V_T$.

Other 2DEG systems include the surface of liquid helium and topological insulators, as well as high-electron-mobility-transistors (HEMTs). In HEMTs, electrons in heterojunctions

between two similar undoped semiconductors (GaAs/GaAlAs for example) are confined into a quantum well. More importantly, unlike in MOSFET, electrons in the undoped heterojunctions can transport without scattering from ionized impurities, resulting in extremely high electron mobility (typically 1,000,000 $cm^2/V \cdot s$ at 4 K). At the same time, the mean free path ($l = \sqrt{2\pi n}\hbar\mu/e$ for material with a parabolic dispersion) could be even larger than the size of the transmission channels, especially at cryogenic temperatures, leading to ballistic transport. The high electron mobility could also enable experimental observations of Shubnikov-de Hass oscillations and the quantum Hall effect (QHE) when the applied magnetic field approaches $1/\mu$.

A common issue of classical 2DEG systems, especially for HEMTs like GaAs/GaAlAs, is that the device fabrication processes are always very complicated, which could involve modulation doping and several steps of growth by molecular beam epitaxy (MBE). Making good electrical contacts to those materials is not trivial, and some are still not fully understood even after decades of investigations. A simpler 2DEG which does not have some of these limitations are thus required for better understanding of the fundamental physics and device applications.

1.2 Graphene - the first real 2D system

As we know, graphene, consisting of a single layer of carbon atoms, is the first two dimensional material ever found. It is the basic structure element of three dimensional graphite and charcoal, one dimensional carbon nanotubes and zero dimensional fullerenes [1]. Unfortunately, it was only isolated and identified recently using the Scotch tape technique. In 2004 graphene was first spotted on a chosen SiO_2 substrate [2], which gives visible contrast for searching with an ordinary microscope [3].

1.2.1 Lattice and band structure

In bulk graphite, neighboring graphene layers are connected by the weak Van de Wales interactions. However, within the graphene plane, carbon atoms are bonded by the sp^2 valence bond, forming hexagonal structure (see Fig. 1.2a). The p_z orbital (bond) is responsible for the conducting of the sheet. The structure can be seen as a triangular lattice with a basis of two atoms per unit cell. Although the six corners are all made of the same carbon atoms, the chemical environments are different for different sites, indicated as A and B.
The unit vectors can be written as ($\alpha = 1.42$ Å is the carbon-carbon distance)

$$a_1 = \frac{a}{2}(\sqrt{3}, 3), \quad a_2 = \frac{a}{2}(\sqrt{3}, -3), \tag{1.1}$$

the nearest neighbor vectors are

$$\delta_1 = \frac{a}{2}(1, \sqrt{3}),\ \delta_2 = \frac{a}{2}(1, -\sqrt{3}),\ \delta_3 = \frac{a}{2}(-2, 0). \tag{1.2}$$

The reciprocal unit vectors are then calculated to be

$$b_1 = \frac{2\pi}{3a}(1, \sqrt{3}), \quad b_2 = \frac{2\pi}{3a}(1, -\sqrt{3}), \tag{1.3}$$

and the Dirac points are

$$K = \frac{2\pi}{3a}(1, \frac{1}{\sqrt{3}}), \quad K' = \frac{2\pi}{3a}(1, -\frac{1}{\sqrt{3}}). \tag{1.4}$$

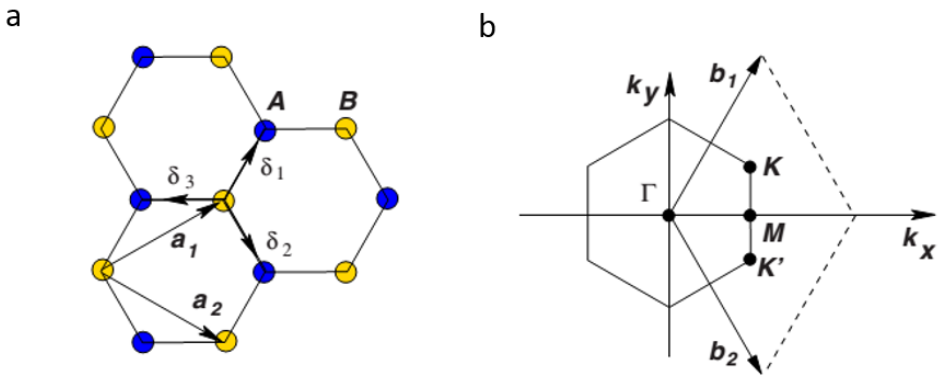

Figure 1.2: Honeycomb lattice and it's first Brillion zone. a, Lattice structure of graphene. a_1, a_2 are unit vectors, δ_i $(i = 1, 2, 3)$ are the nearest neighbor vectors. b, First Brillion zone, K and K' are the Dirac points; b_1 and b_2 are the reciprocal unit vectors. (Figure taken from Ref. [4])

According to the tight bonding model, considering the nearest neighbor and next-nearest neighbor hopping, the Hamiltonian would be [4]

$$H = -t \sum_{<i,j>,\sigma} (a_{i,\sigma} b^{+}_{j,\sigma} + H.c.) - t' \sum_{<<i,j>>,\sigma} (a_{i,\sigma} a^{+}_{j,\sigma} + b_{i,\sigma} b^{+}_{j,\sigma} + H.c.). \tag{1.5}$$

Here, t and t' are the nearest and next-nearest hopping energies, $< i, j >$ and $<< i, j >>$ indicate the sum over nearest neighbor and next nearest neighbor. $a_{i,\sigma}$, $b_{i,\sigma}$ $(a^{+}_{i,\sigma}$, $b^{+}_{i,\sigma})$ are annihilation (creation) operates of one electron with spin $\sigma(\uparrow, \downarrow)$ on site R_i. For most of the case, we only consider the nearest neighbor hopping $(t' = 0)$. The Hamiltonian can be rewritten as [5]

$$H = t \begin{bmatrix} 0 & \sum_{i=1}^{3} e^{ik\cdot\delta_i} \\ \sum_{i=1}^{3} e^{-ik\cdot\delta_i} & 0 \end{bmatrix}. \tag{1.6}$$

The eigenvalues are

$$E(k) = \pm t\sqrt{3 + f(k)},$$

where

$$f(k) = 2\sin(\sqrt{3}k_y a) + 4\cos(\frac{\sqrt{3}}{2}k_y a)cos(\frac{3}{2}k_x a).$$

The '+' and '-' signs indicate the upper band (π^*) lower band (π) individually. This dispersion is plotted in Fig. 1.3. The upper band touches the lower band at the six corners of the first Brillion zone.

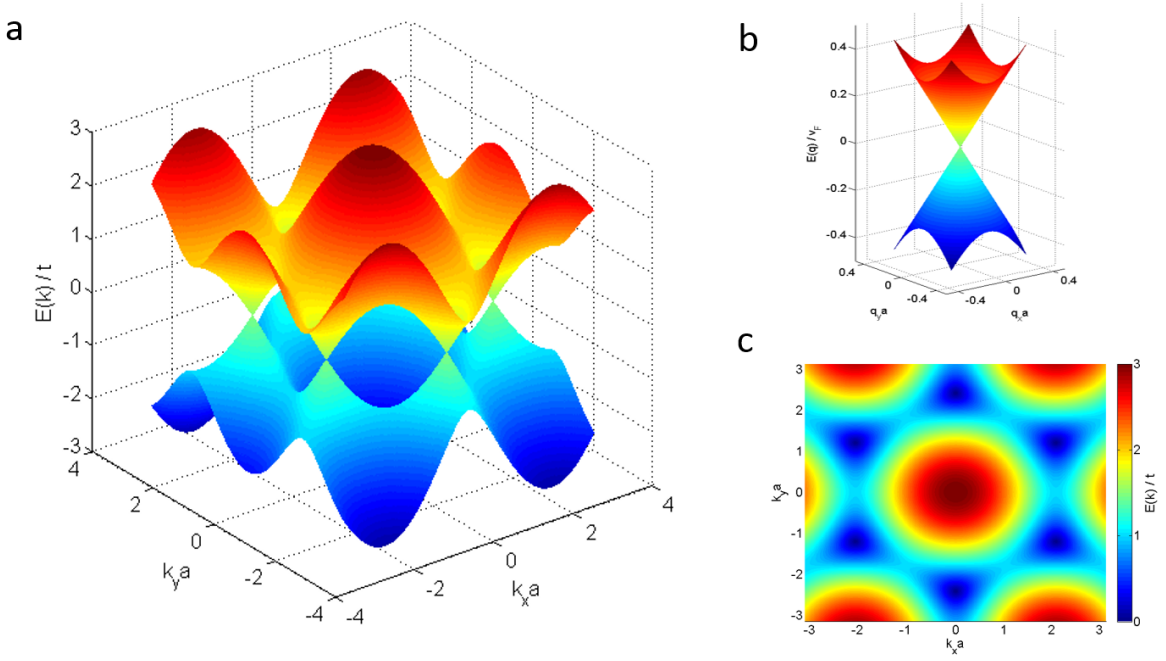

Figure 1.3: a, Electronic dispersion of single layer graphene, the upper band (π^*) touch the lower band (π) at the six corners of the first Brillion zone. b, Dispersion near one of the corners (Dirac cone), where $q = k - K$. c, Contour plot of the dispersion relation.

As shown in Fig. 1.3b, around Dirac points the dispersion is linear (so called Dirac cones). Suppose $q = k - K$ ($q = k - K'$ around K'), taking the first order Taylor expansion of formula (1.6), the Hamiltonian becomes

$$H_K = \frac{3at}{4}(1+\sqrt{3})\begin{bmatrix} 0 & iq_x - q_y \\ -iq_x - q_y & 0 \end{bmatrix} = \frac{3at}{4}(1+\sqrt{3}i)\hat{\sigma}\cdot q,$$

$$H_{K'} = \frac{3at}{4}(1+\sqrt{3})\begin{bmatrix} 0 & -iq_x+q_y \\ iq_x+q_y & 0 \end{bmatrix} = -\frac{3at}{4}(1+\sqrt{3}i)\hat{\sigma}\cdot q,$$

where $\hat{\sigma}$ is the properly chosen Pauli matrices

$$\sigma_x = \begin{bmatrix} 0 & i \\ -i & 0 \end{bmatrix}, \sigma_y = \begin{bmatrix} 0 & 1 \\ 1 & 0 \end{bmatrix}, \sigma_z = \begin{bmatrix} 1 & 0 \\ 0 & -1 \end{bmatrix}.$$

In total, the Hamiltonian around Dirac points can be summarized to be

$$H = v_F \begin{bmatrix} \hat{\sigma}\cdot q & 0 \\ 0 & -\hat{\sigma}\cdot q \end{bmatrix} = v_F(\tau_z\sigma_x q_x + \sigma_y q_y),$$

where $v_F = 3at/2 \approx 1\times 10^6 m/s$ is the Fermi velocity, τ_z is the valley index ($\tau_z = 1$ for K valley, $\tau_z = -1$ for -K valley). The eigenvalues are

$$E(q) \approx \pm v_F|q|. \tag{1.7}$$

Different from massive electrons in semiconductors, in graphene the linear dispersion indicates a zero effective mass of carriers around Dirac points. More importantly, the Dirac nature of electrons (holes) also means they can travel in graphene without scattering from phonons ideally, leading to extremely high carrier mobilities and ballistic transport for channels of micrometer size. For example, the mobility of graphene at room temperature has been determined [6] to be $15,000\ cm^2/V\cdot s$, much larger than that of silicon (typically $1,400\ cm^2/V\cdot s$ for electrons and $450\ cm^2/V\cdot s$ for holes).

1.2.2 Integer quantum Hall effect in Graphene

The quantum Hall effect is a quantum version of Hall effect observed when 2DEG systems are subjected to a strong magnetic field at low temperatures, in which the Hall conductance takes the quantized value

$$\sigma_H = I_{chanel}/V_H = \nu \frac{e^2}{h}.$$

Here, $I_{channel}$ is the channel current, and ν is the filling factor. $\nu = 1, 2, 3, \cdots$, indicates the integer quantum Hall effect (IQHE), while $\nu = 1/3, 2/5, 3/7, \cdots$, indicate the fractional quantum Hall effect (FQHE). The exact quantization of the QHE with 1ppb error was latter used in metrology for resistance calibration.

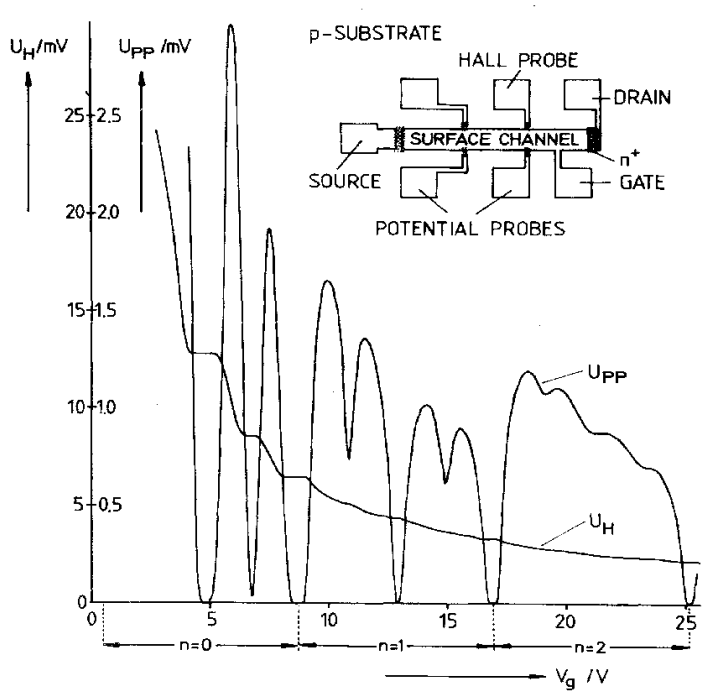

Figure 1.4: Longitudinal voltage U_{pp} and Hall voltage U_H as a function of gate voltage V_g at T=1.5 K, B = 18 T. Inset is a top view of the device, with length $L = 400\ \mu m$, width $W = 50\ \mu m$, and distance between the two probes $L_{pp} = 130\ \mu m$. (Figure taken from Ref. [7])

The IQHE was originally predicted by Ando, Matsumoto, and Uemura in 1975. In 1980, Klaus von Klitzing discovered the exact quantization in Si MOSFET under high magnetic field as in Fig. 1.4. When the 2DEG in Si-MOSFET is under inversion, and subjected to high magnetic field (18 T) at low temperature (1.5 K), the band structure is quantized into Landau Levels (LLs). As $\mu B \sim 1$, quantum oscillations are visible when sweeping the gate voltage.

Graphene, on the other hand, has its own advantage, it hosts massless Dirac fermions, which is generically more beneficial than other 2DEG. The integer quantum Hall Effect in graphene was first reported by two group independently in 2005 at close to liquid helium temperature [8, 9], and was later found that the effect could be observed at room temperature [10]. Under the magnetic field ($\vec{B} = B\hat{z}, \vec{A} = -yB\hat{x}$), the Hamiltonian (around K) is

$$H = v_F \hat{\sigma} \cdot (\vec{q} + \frac{e\vec{A}}{\hbar c}) = v_F[\sigma_x(q_x - \frac{eyB}{\hbar c}) + \sigma_y q_y].$$

A easy way to derive the eigenvalues is by calculating H^2,

$$\begin{aligned} H^2 &= v_F^2[(q_x - \frac{eyB}{\hbar c})^2 + q_y^2 - \sigma_x\sigma_y\frac{eB}{\hbar c}[y, q_y]] \\ &= v_F^2[q_y^2 + (\frac{eB}{\hbar c})^2(y - y_0)^2 + \frac{eB}{\hbar c}\sigma_z] \\ &= (\frac{v_F}{\hbar})^2[\hbar^2 q_y^2 + \omega_c^2(y - y_0)^2 + \hbar\omega_c\sigma_z]. \end{aligned}$$

Here, $\omega_c = eB/c, y_0 = \frac{\hbar c}{eB}q_x, [H^2, q_x] = 0$. H^2 is close to the Hamiltonian of a harmonic oscillator. The eigenvalues are

$$E_{q_x,n}^2 = (\frac{v_F}{\hbar})^2\hbar\omega_c[\sigma_z + (2n+1)] = (\frac{v_F}{\hbar})^2\hbar\omega_c \begin{bmatrix} 2n+2 & 0 \\ 0 & 2n \end{bmatrix}.$$

In all,

$$E_{q_x,n} = v_F\sqrt{\hbar\omega_c}\sqrt{n}.$$

Here, $n = 0, 1, 2, \cdots$. For all $n \leq 1$, different LLs have the same degeneracy (spin and valley degeneracy included)

$$N_n = 4\phi/\phi_0.$$

The zero Landau Level (zLL) is slightly different, with half the degeneracy. In terms of IQHE, the Hall conductivity is quantized to be

$$\sigma_{xy} = 4(\nu + \frac{1}{2})\frac{e^2}{h},$$

where ν is the filling factor of the LL.

Electrons fill from the lowest LL to the Fermi level. When the Fermi level is within the gap of two LLs, the bulk part won't conduct. But on the edge of the 2DEG, due to the band bending, there would be chiral edge current. For each LL, the edge contribution to the total conductance would be $4e^2/h$, considering the spin and valley degeneracies.

These edge conduction may also be understood in terms of the skipping motion electrons execute as their cyclotron orbits bounce off the edge. Importantly, the electronic states responsible for this motion are chiral in the sense that they only propagate in one direction along the edge. These states are insensitive to disorder because there are no states available for backscattering, a fact that underlies the perfectly quantized electronic transport in the quantum Hall Effect.

Although quantum mechanics predicts the LL splitting for arbitrary 2DEG, in real experiment, LLs are not discrete but largely broadened. One of the criteria for observing the Shubnikov de Hass (SdH) oscillation is $\mu B \sim 1$. Since the magnetic field is quite limited (usually 10s of Tesla), 2DEG with large mobility is the only choice. Figure 1.5 is one of the measurements from the Colombia group[9], for fixed gate voltage (Fig. 1.5a) as the magnetic field increases, the LL degeneracy increases for each LL below the Fermi level, the LL spacing increases, and thus the filling factor decreases discretely, indicating a quantized increasing Hall resistance. On the other hand, for fixed magnetic field B (Fig. 1.5b), as we increase the gate voltage from negative to positive, the Fermi level also goes from the lower Dirac band to the upper band and the filling factor also changes discretely, leading to quantized Hall resistance.

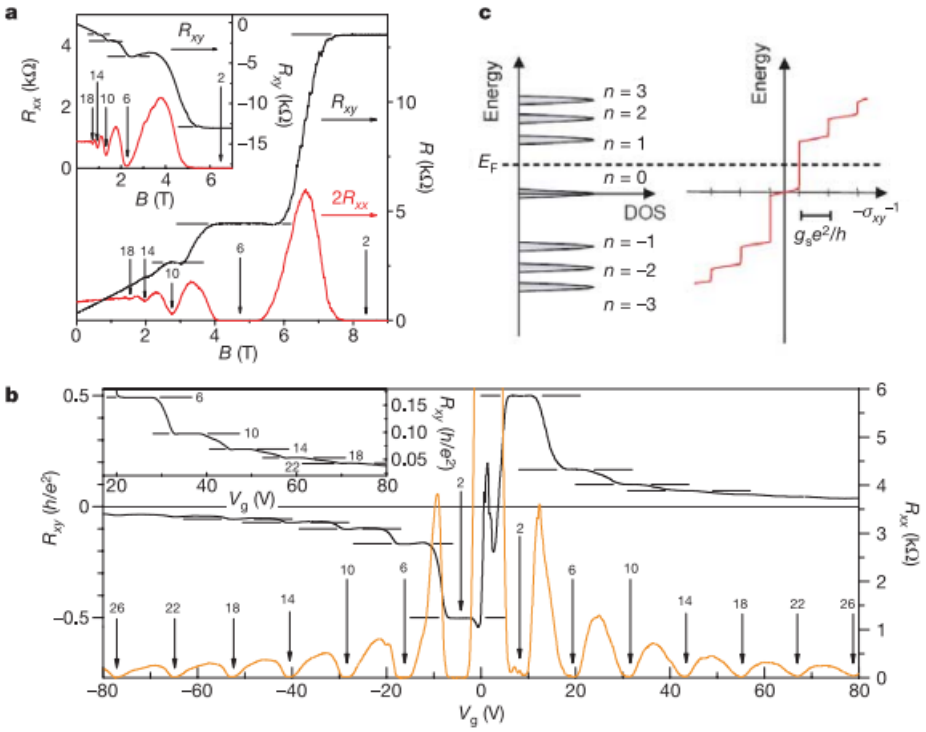

Figure 1.5: a-b, Quantized magneto resistance and Hall resistance of graphene device, $T = 30\ mK$, $V_g = 15\ V$ in (a), $T = 1.6\ K$, $B = 9\ T$ in (b). c, schematics of the quantized resistance and corresponding Landau Levels. (Figure taken from [9])

So far, the electron-electron interaction is neglected in our discussion about IQHE in 2DEG. This only applies when the carrier density and the magnetic field are relatively low. In fact, except for the integer resistance plateaus, when the magnetic field is high enough, fractional plateaus start to develop. This was also first seen in GaAs/GaAlAs heterostructures[11].

1.3 Transitional metal dichalcogenides

In previous sections we talked about different 2DEG systems, including conventional quantum wells and single layer graphene. Except for these systems, recently transitional metal dichalcogenides, in their atomically thin forms, have caught tremendous attentions because of their supreme physical properties and recent advances in technologies like sample growth, device fabrication, and optical detection etc. Some of the most investigated TMDCs with distinct electric properties are provided in the following table.

Table 1 | Summary of TMDC materials and properties.

	-S_2		-Se_2		-Te_2	
	Electronic characteristics	References	Electronic characteristics	References	Electronic characteristics	References
Nb	Metal; superconducting; CDW	138 (E)	Metal; superconducting; CDW	138,164 (E)	Metal	83 (T)
Ta	Metal; superconducting; CDW	138,164 (E)	Metal; superconducting; CDW	138,164 (E)	Metal	83 (T)
Mo	Semiconducting 1L: 1.8 eV Bulk: 1.2 eV	31 (E) 88 (E)	Semiconducting 1L: 1.5 eV Bulk: 1.1 eV	82 (T) 88 (E)	Semiconducting 1L: 1.1 eV Bulk: 1.0 eV	82 (T) 165 (E)
W	Semiconducting 1L: 2.1 eV 1L: 1.9 eV Bulk: 1.4 eV	25 (T) 82 (T) 88 (E)	Semiconducting 1L: 1.7 eV Bulk: 1.2 eV	83 (T) 88 (E)	Semiconducting 1L: 1.1 eV	83 (T)

The electronic characteristic of each material is listed as metallic, superconducting, semiconducting or charge density wave (CDW). For the semiconducting materials, the bandgap energies for monolayer (1L) and bulk forms are listed. The cited references are indicated as experimental (E) or theoretical (T) results.

Table 1.1: summary of common TMDC materials and their electronic properties. (Table taken from Ref. [12])

1.3.1 Lattice and band structure

Transition metal dichalcogenides are common layered materials, in which the adjacent layers are stacked by the Van de Waals interactions. It can be easily thinned down into a monolayer by mechanical exfoliation. The single layer MX_2 is composed of one layer of transition metal atoms, sandwiched between two layers of chalcogenide atoms. Usually for the single layer there are two types of stacking (see Fig. 1.6), the ABA stacking (1H phase) and the ABC

stacking (1T phase). ABA stacking is noncentrosymmetric [13, 14] with space group $P6m2$, and is the stable phase of most semiconducting monolayers (M = Mo, W; X = S, Se). ABC stacking, on the other hand, is centrosymmetric, but is usually not preferable energetically. There would be an additional distortion, and it ends up with a lower symmetric 1T' phase (space group $P2_1/m$). In the 1T' phase, the transition metal atoms dimerize and form quasi one dimensional zigzag chains, and is the stable phase of single layer WTe_2 and $MoTe_2$. More information on the 1T' MX_2 will be provided in Chapter 3, for the rest of this chapter, we will focus on semiconducting monolayers in the 1H phase.

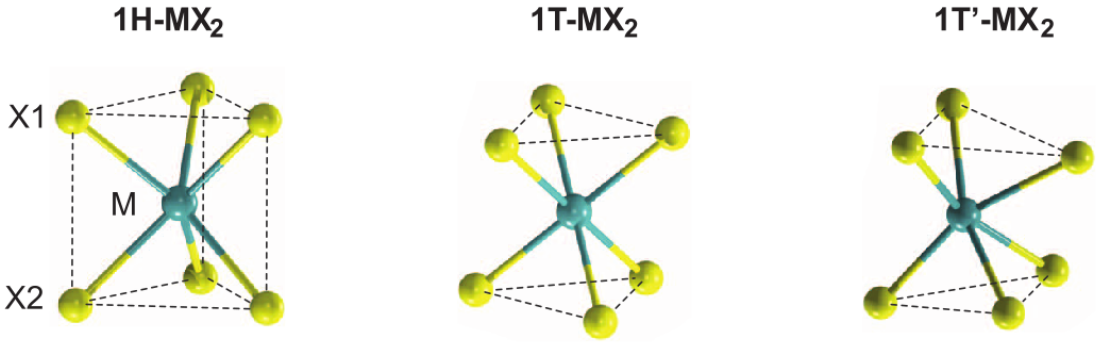

Figure 1.6: Atomistic structures of monolayer MX_2 with stacking order 1H, 1T, 1T' respectively. (Figure adapted from Ref. [15])

Figure 1.7 shows the schematics of the lattice and band structure of monolayer MX_2 in the 1H phase, where the inversion symmetry is intrinsically broken. A bandgap of 1-2 eV in the visible spectral range is open. The conduction band minimum (CBM) and valence band maximum (VBM) are both located around the K (-K) points (Dirac points, corners of the first Brillion zone), making the monolayer a direct bandgap semiconductor [12, 16]. Except for the opening of a bandgap around the Dirac points the spin degeneracy is lifted [12]. The magnitude of the spin splitting can be as large as hundreds of meV [17], while the spin polarizations are different for K and -K points, making it a promising candidate for

applications in valley- and spin-tronics.

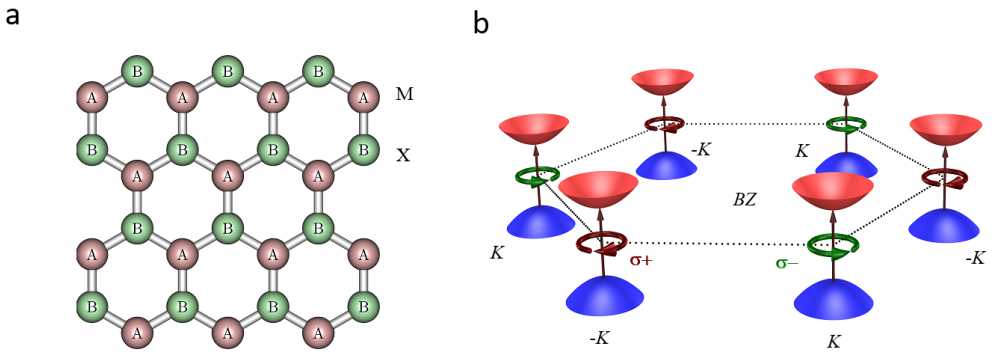

Figure 1.7: Schematics of the lattice and band structure of MX_2. a, Top view of the MX_2 monolayer, where A and B are different sites, representing M and X atoms respectively. b, Schematic drawing of the band structure at the band edges located at K (-K) points.

1.3.2 Valley degree of freedom and optical selection rules

The 1-2 eV direct band gap around the Dirac point makes monolayer MX_2s unique platforms for optical studies. A visible laser could be used for excitations, making detections much easier. As we mentioned in the last section, due to the lack of inversion symmetry in monolayer MX_2 in the 1H phase, the spin textures are the opposite for K and -K points, which are separated by a large momentum. Thus, the inter-valley scattering is largely suppressed [13], and valley as a degree of freedom (DOF) is a relatively good quantum number and can be used as an information carrier similar to the spin DOF.

The magnetic momentum for the n-th Bloch state is calculated [18] to be (around K)

$$m_n(k) = -i\frac{e\hbar}{2m^2}\sum_{i\neq n}\frac{P_{n,i}(k)\times P_{i,n}(k)}{E_{n,0}(k)-E_{i,0}(k)}.$$

Here, $P_{n,i}(k) =< u_{n,k}|\hat{p}|u_{i,k} >$ is the inter-band matrix element for the canonical momentum

operator. $E_{n,0}(k)$ is the Bloch Eigen energy. The Berry curvature is determined to be

$$\Omega_n(k) = -i\frac{\hbar^2}{m^2}\sum_{i\neq n}\frac{P_{n,i}(k)\times P_{i,n}(k)}{(E_{n,0}(k)-E_{i,0}(k))^2}.$$

From above, we know that the two Bloch states with opposite spins in a Kramer's pair (TRS is unbroken) have opposite values of m and Ω. And for each valley near the Dirac points, the magnetic momentum and Berry curvature do not vanish [14, 18]. The non-zero magnetic momentum means that the electrons are circularly polarized. For excitations with certain circular polarization, only one valley would be excited (see Fig. 1.7b). After recombination the luminescence would also be circularly polarized. The polarization of the photoluminescence could be quantified by (for σ_- excitation)

$$\eta = \frac{I(\sigma_-) - I(\sigma_+)}{I(\sigma_-) + I(\sigma_+)}.$$

Here, $I(\sigma_-)$ ($I(\sigma_+)$) is the intensity of the photoluminescence of left (right) polarization. The experimental determinations on the selection rules were performed in both monolayer and bilayer layer MX_2s [14, 17, 19, 20] with circularly polarized light.

1.4 Quantum spin Hall effect

In section 1.2.2, we discussed the quantized edge conduction that emerged at the edges of a 2D integer quantum Hall system despite the insulating bulk. In this section, we are going to talk about another type of Hall effect, the quantum spin Hall (QSH) effect, which is closely related to the QHE with gapped interior and gapless edge states. The difference is in the quantum Hall system to have the topological nontrivial state ($n \neq 0$) usually a strong magnetic field is applied, thus breaking the time reversal-symmetry. As illustrated in Fig. 1.8, the forward and backward movers in the quantum Hall bar are spatially separated and no backscattering is allowed on either edges.

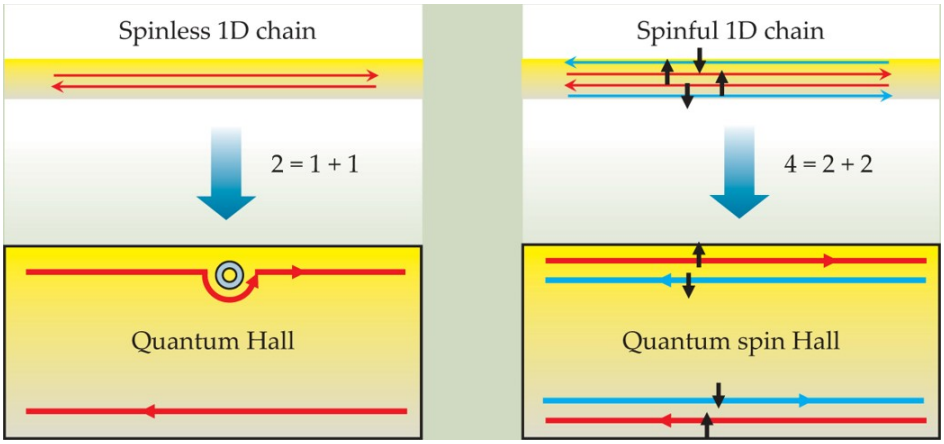

Figure 1.8: Comparison of QHE and QSHE. A spinless 1D system has both a forward and backward mover. Those two channels are spatially separated in a QH bar, where the upper edge contains only a forward mover and the lower edge has only a backward mover. A spinful 1D system has four basic channels, which are also spatially separated in a QSH bar. The upper edge contains a forward mover with up spin and a backward mover with down spin, and conversely for the lower edge. (Figure taken from Ref. [21])

In a QSH system, however, no magnetic field is needed and the time-reversal symmetry (TRS) is preserved. In this case, the spin and momentum of the electrons are locked due to

the strong spin orbital coupling. While the free carriers are still confined to the edges, there are both forward and backward movers on either edges with the opposite spin textures. For example, in Fig. 1.8, the upper edge contains a forward mover with up spin and backward mover with down spin, which are essentially different from the 1D conductor. For either edges, Kane and Mele [22] showed that the reflection amplitude is odd under time reversal, roughly because it involves flipping of the spin. Thus at zero temperature, without breaking TRS, the edge transport is dissipationless regardless of disorder.

At nonzero temperature, inelastic backscattering processes are allowed, resulting in a finite conductivity for edges longer than the phase coherence length, $l > l_\phi$. However, for $l < l_\phi$, even at nonzero temperature, the edge transport can still be considered as ballistic. The two-terminal conductance for a single edge can be described by the Landauer formula,

$$G = \frac{e^2}{h} MT \tag{1.8}$$

Here, M represents the number of modes, which equals 1 for the QSH edge state. T is the transmission coefficient for an electron injected at one end the conductor and collected by the other end. Assuming perfectly transparent contacts, the conductance would be $G = e^2/h$. For multi-terminal configurations, one could derive the conductance between any pair using the Büttiker formula.

1.4.1 Quantum spin hall effect in HgTe/CdTe quantum well

The first toy model of the QSH effect is made on graphene [22]. However, due to the weak spin-orbital interaction (10^{-3} meV), there is almost no observable effect in experiment. Latter, Bernevig, Hughes and Zhang (BHZ) proposed to consider the HgTe/CdTe quantum well structures, which have much stronger spin-orbital interactions. Inside these quantum wells, essentially, there is one layer of HgTe sandwiched by two layers of CdTe. When the thickness of the HgTe is above a critical value ($d_c = 6.3$ nm), the bands in WTe_2 would be inverted, resulting in a gaped bulk with nontrivial topological invariant, $Z_2 = 1$.

Shown in Fig. 1.9 is the first transport measurements on HgTe/CdTe quantum well

structures by König et al [23]. For HgTe thinner than the critical thickness ($d < d_c$, device I), at certain gate range, the four terminal resistance is much larger than h/e^2, indicating it's a normal insulator. However, when the thickness is above the critical thickness ($d > d_c$, device II, III, IV), when the Fermi level is tuned into the gap, the resistance is significantly smaller and develops a plateau, the value of which saturates to $h/2e^2$ when the size of the device is smaller enough (device III and IV). The perfect quantization is one of the key signature of the quantum spin Hall effect.

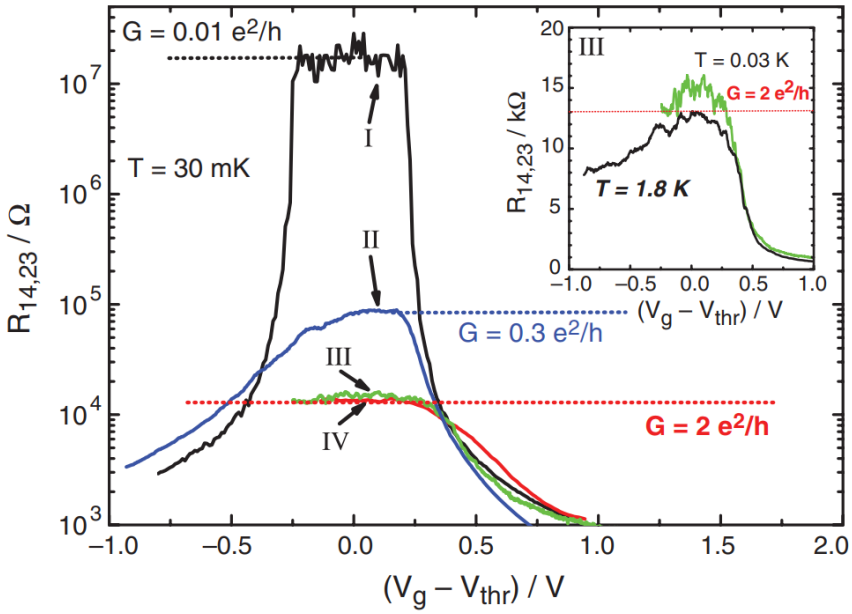

Figure 1.9: The longitudinal four terminal resistance ($R_{14,23}$) of various normal (d = 5.5 nm) (I) and inverted (d = 7.3 nm) (II, III, and IV) QW structures as a function of V_g at $B = 0\ T$, $T = 30\ mK$. The device sizes are $(20.0 \times 13.3)\mu m^2$ for devices I and II, $(1.0 \times 1.0)\mu m^2$ for device III, and $(1.0 \times 0.5)\mu m^2$ for device IV. The inset shows $R_{14,23}(V_g)$ of two samples from the same wafer, having the same device size (III) at 30 mK (green) and 1.8 K (black) on a linear scale. (Figure taken from Ref. [23])

1.5 Summary and outline

The fast explosion of 2D materials offers great opportunities for making new functional materials as well as provides platforms for realizing a lot of the fundamental physics, such as the quantum Hall effect, quantum spin Hall effect, high temperature superconductivity and valley-tronics. This thesis focuses on one type of these two dimensional materials, the 2D semimetal, including graphene and tungsten ditelluride (WTe_2).

In Chap. 2, we will talk about the discovery of a new type of photocurrent in monolayer graphene, generated by the photo Nernst effect. Different from other mechanisms, the photo Nernst current is a subtle effect that only dominates photocurrent in ultra clean and uniform graphene devices. In the photo Nernst effect, an out-of-plane magnetic field is applied, which breaks the mirror symmetry, resulting in a net current when the laser is parked near the free edges of the graphene flake. The photocurrent has opposite signs for the opposite edges and is linear with the magnetic field in the low field regime. Furthermore, the photo Nernst current is found to be more sensitive to the topology of the electronic structure than the four-terminal transport measurements for an high magnetic field. To explain these observations quantitatively, we developed a thermoelectric model from the microscopic theory.

In Chap. 3, we will start with a short introduction to the other 2D semimetal, WTe_2, we will talk about the large non saturating magnetoresistance in the bulk material as well as the nontrivial topology associated with bulk and monolayer WTe_2. At the same time, we will investigate the temperature dependence and the magnetoresistance when WTe_2 is thinned down into the monolayer limit. This chapter also serves partially as an introduction to the following two chapters.

Chap. 4 is mainly about the magneto-transport properties of monolayer WTe_2 near the charge neutrality. We found that the interior of monolayer WTe_2 is insulating below about 100 K while the edge remains conducting down to 1.6 K. The edge conduction is strongly suppressed by an in-plane magnetic field and is independent of gate voltage, save for mesoscopic fluctuations that grow on cooling due to a zero-bias anomaly, which reduces

the linear-response conductance. Many of the observations are consistent with monolayer WTe_2 being a 2DTI. However, the low-temperature edge conductance, for contacts spacings down to 150 nm, never reaches e^2/h, suggesting significant elastic scattering in the edge. We will also show a direct imaging of the conducting edge channels by scanning microwave impedance measurements.

The last chapter is on field induced superconductivity in monolayer WTe_2. With an electrostatic gate, one could easily tune the interior of monolayer WTe_2 from an insulator to a superconductor. The superconductivity is also highly tunable, the critical temperature can be tuned from 700 mK at high doping level to below 200 mK at low doping levels. At the lowest temperature (20 mK), a critical field of 35 mT is observed for out-of-plane magnetic field. When the magnetic field is aligned in the sample plane, the critical field is much higher. We also studied the gate tunable insulator to metal transition at various temperatures, which are scaled into an universal curve, indicating this transition could be a quantum phase transition.

Chapter 2

PHOTO NERNST EFFECT IN GRAPHENE

2.1 Introduction

2.1.1 Magneto scanning photocurrent microscopy

Scanning photocurrent microscopy (SPCM) belongs to the family of scanning probe microscopy, and is a very powerful tool for investigating spatial-dependent optoelectronic properties of classical semiconductors and their nano-structures[24–28]. In SPCM, a focused laser is raster-scanned across the sample, generates a laser-position dependent photocurrent map. A typical setup for the SPCM is shown in Fig. 2.1.

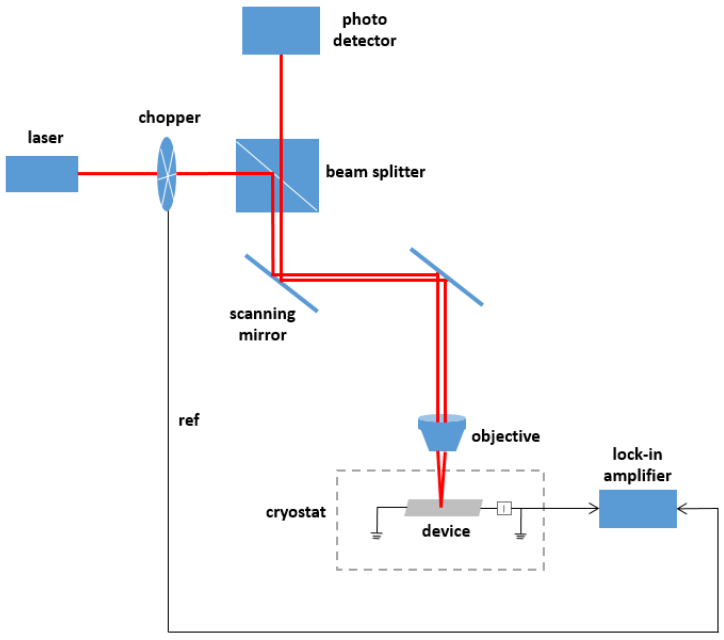

Figure 2.1: Schematic diagram of the scanning photocurrent microscopy

2.1.2 Model the long range photocurrent in graphene

Classical SPCM experiments are always conducted in semiconductor devices, in which electron-hole recombination process is greatly slowed down due to the existence of a solid band gap. The long live electrons and holes are usually separated by an electric field and diffuse into the contacts, resulting in a measurable photocurrent. This is basically the photo voltaic effect. Graphene, however, is a gapless material, the conduction band touches the valence band at the Dirac points, making electrons and holes less distinct. On the other hand, photocurrent has been observed when light is focused on inhomogeneous, junctions[29, 30] and boundaries[31] in graphene devices, and is suggested to be related to the thermal electric effect.

Due to the slow electron-lattice cooling process in graphene, the photo excited electron hole pairs always form the so called hot carriers near the Fermi surface, which are crucial for understanding charge and energy transfers in graphene. So far most researches have been focused on the local photocurrent generation, while much less attention has been put on the later stage, ie. how the charge transports on the long range scale. For ultra clean graphene devices, the electron/hole mobility has been shown[32–35] to be very close to GaAs/GaAlAs quantum wells, and a mean free path of tens of micrometers has been achieved. At low temperatures, when the symmetry for "left" and "right" moving carriers is broken, a long range photocurrent is expected in graphene. Recently, Song and Levitov[29] proposed another type of long range response similar to the Shockley-Ramo type photo response[36–38]. In the following of this chapter, a new member of the thermal electric effect, the photo Nernst effect, in graphene will be introduced. We will also apply the Song-Levitov result to the SPCM in a low magnetic field.

2.1.3 Long range photocurrent generation

The movement of charged particles in an electrostatic field is governed by the Poisson equation (see Appx. A). However, for gapless material like graphene, it becomes a steady current

problem, and the movement of charge particles instead follows the continuity equation.

$$\nabla \cdot (j_d + j_{ph}) = \nabla \cdot (-\sigma \nabla \phi + j_{ph}) = 0. \tag{2.1}$$

Here $j_d = -\sigma \nabla \phi$ is the diffusion current density, j_{ph} is the photocurrent density, ϕ is the electric potential. The boundary conditions at the free edges (no outgoing current) and near the contacts (equal potential) are described as following respectively,

$$n \cdot (j_d + j_{ph}) = 0, \tag{2.2}$$

$$n \times \nabla \phi = 0. \tag{2.3}$$

In experiment, what we measured is the total photocurrent collected by one of the contact (short circuit photocurrent) regardless of the details of current flow inside the material. Song and Levitov [27] figured out this long range photoresponse by using the concept of weighting (auxiliary) field as in the original Shockley-Ramo theorem. The weighting field(ψ) satisfies the following equations,

$$\nabla \cdot j^{(\psi)} = 0, \;\; j^{(\psi)} = -\sigma^T \nabla \psi. \tag{2.4}$$

Similarly, the boundary conditions at the free edges and near the contacts for the weighting field are

$$n \cdot j^{(\psi)} = 0, \tag{2.5}$$

$$n \times \nabla \psi = 0. \tag{2.6}$$

With this auxiliary field, the total photocurrent can be calculated with the following trick,

$$\begin{aligned}
\iint \nabla \cdot (j_d + j_{ph}) \psi dx dy &= \oint n \cdot (j_d + j_{ph}) \psi dl - \iint (j_d + j_{ph}) \cdot \nabla \psi dx dy \\
&= \oint n \cdot j \psi dl - \iint \nabla \phi \cdot (-\sigma^T \nabla \psi) dx dy - \iint j_{ph} \cdot \nabla \psi dx dy \\
&= \oint n \cdot j \psi dl - \iint \nabla \phi \cdot j^{(\psi)} dx dy - \iint j_{ph} \cdot \nabla \psi dx dy \\
&= \oint n \cdot j \psi dl - \oint n \cdot j^{(\psi)} \phi dl - \iint j_{ph} \cdot \nabla \psi dx dy = 0.
\end{aligned}$$

Thus,

$$\iint j_{ph} \cdot \nabla\psi dxdy = \sum_k (I_k\psi_k - I_k^{(\psi)}\phi_k). \tag{2.7}$$

For convenience, if we choose $I_k^{(\psi)}$ to be zero at all contacts, ψ_k to be zero except the one connected to the preamp to be 1, then the photocurrent we measured can be simplified as

$$I_{ph} = \iint j_{ph} \cdot \nabla\psi dxdy. \tag{2.8}$$

Knowing the local photocurrent density (j_{ph}) and the weighting field ($\nabla\psi$), the generated long range photocurrent can be easily calculated as equation 2.8. In the next section, I am going to discuss the calculation of local photocurrent density and weighting field first, then I will show that the long range photocurrent can be formulated as the Nernst effect.

2.1.4 Nernst coefficient

To derive the Nernst coefficient for a graphene device, we started from its original definition. Phenomenologically, the macroscopic electric current density j_e and heat current density j_Q can be described by the following equations,

$$j_e = \sigma E - \alpha\nabla T, \tag{2.9}$$

$$j_Q = \alpha T E - \kappa\nabla T. \tag{2.10}$$

The Nernst coefficient N is defined to be $N = E_y/(B_z(dT/dx))$, if $j_e = 0, \nabla T = dT/dx\hat{x}$. Under this definition, equation 2.9 becomes $E = \sigma^{-1}\alpha\nabla T$, thus

$$E_y = (\sigma^{-1}\alpha)_{yx} dT/dx = (\rho_{yx}\alpha_{xx} + \rho_{yy}\alpha_{yx})dT/dx,$$

$$N = E_y/(B_z(dT/dx)) = -\frac{1}{B_z}(\rho_{xx}\alpha_{xy} + \rho_{xy}\alpha_{xx}). \tag{2.11}$$

The last derivation used the Onsager relation, and also assumed conductivity is isotropic in the sample plane, which is the case for graphene. With the Mott relation, $\alpha_{ij} = -\frac{\pi^2}{3}\frac{k_B^2 T}{e}\frac{\partial\sigma_{ij}}{\partial\epsilon_F}$, equation 2.11 can also be written as

$$N = \frac{\pi^2 k_B^2 T}{3eB_z}(\rho_{xx}\frac{\partial\sigma_{xy}}{\partial\epsilon_F} + \rho_{xy}\frac{\partial\sigma_{xx}}{\partial\epsilon_F}) = -\frac{\pi^2 k_B^2 T}{3eB_z}\sigma_{xx}\rho_{xx}\frac{\partial}{\partial\epsilon_F}(\frac{\sigma_{xy}}{\sigma_{xx}}). \tag{2.12}$$

2.1.5 Weighting field in graphene strip and the photocurrent

The weighting field for a rectangular graphene strip under the magnetic field is not easy to solve analytically. However, for graphene strip with a large aspect ratio, far away from the contacts area, the auxiliary current density $j^{(\psi)}$ is approximately $j^{(\psi)} \approx -\frac{1}{\rho_{xx}L}\hat{x}$ (the prefactor is chose so that at $x = L$, $\psi = 1$). The weighting field is

$$\nabla\psi = -(\sigma^T)^{-1}j^{(\psi)} = -\rho^T j^{(\psi)} \approx \frac{1}{L}(\hat{x} + \frac{\rho_{xy}}{\rho_{xx}}\hat{y}). \tag{2.13}$$

Since the local photocurrent density from equation 2.9 is $j_{ph} = -\alpha\nabla T$ at zero bias, we can calculate the photocurrent collected by one of the contacts,

$$I_{ph} = \iint j_{ph}\nabla\psi dxdy \approx \frac{1}{L}(-\alpha\nabla T)(\hat{x} + \frac{\rho_{xy}}{\rho_{xx}}\hat{y}) = -\frac{1}{L}(\alpha_{xy} + \frac{\rho_{xy}}{\rho_{xx}}\alpha_{yy})\int_0^L\int_0^W \frac{\partial T}{\partial y}dxdy$$

$$= -(\alpha_{xy} + \frac{\rho_{xy}}{\rho_{xx}}\alpha_{yy})\frac{1}{L}\int_0^L \Delta T(x)dx = -(\alpha_{xy} + \frac{\rho_{xy}}{\rho_{xx}}\alpha_{yy})\Delta T_{av}.$$

Here $\Delta T_{av} = \frac{1}{L}\int_0^L\int_0^W \frac{\partial T}{\partial y}dxdy$ is the averaged temperature increasement due to the photo illumination. Compare this formula with equation 2.11, we can rewrite the photocurrent in terms of the Nernst coefficient (the prefactor β ($1 > \beta > 0$) is added due to the contact effect),

$$I_{ph} = \frac{\beta}{\rho_{xx}}NB_z\Delta T_{av}. \tag{2.14}$$

2.2 Experiment

2.2.1 Device fabrication and experiment setup

Two-terminal graphene devices were made on doped Si/SiO_2 substrate, in which the Si substrate is used as the bottom gate (see Fig. 2.2(a) for the optical image of a typical graphene device). Figure 2.2(b) shows the transfer characteristics of a two-terminal graphene device at both room and cryogenic (40 K) temperatures. The gate dependences can be fitted with the FET equation $R = R_c + \frac{l/w}{e\mu\sqrt{n_0^2+n_{2D}^2}}$. The 2D carrier density is estimated using the capacitance $n_{2D} = C\Delta V_g$, $C = 120\,\mu F/m^2$ for 285 nm of SiO_2, $l/w \approx 2$ for the device. The best fitting yields a field effect mobility of 20,000 $cm^2/V \cdot s$ at 40 K, and 17,000 $cm^2/V \cdot s$ at 300 K. The extracted residual local carrier fluctuation n_0 is $8 \times 10^{10}\,cm^{-2}$ at 40 K and $13 \times 10^{10}\,cm^{-2}$ at 300 K, indicating the graphene device is very clean and homogeneous. And this is very important for the observation of the photo Nernst effect, which would be the focus of the later part.

The scanning photocurrent microscopy in Fig. 2.2(c) is measured at 40 K and zero magnetic field with 632 nm laser. A small gate of $\Delta V_g = 5\ V$ is applied, so the graphene is slightly n doped. From the 2D colormap, we can see a significant photocurrent when the laser is parked near the two contacts, which can be understood by the formation of Schottky barrier near the metal contacts. When the laser is parked elsewhere, far away from the contacts but still on the graphene, the photocurrent is negligible. However, under an out-of-plane magnetic field, except for the photocurrent discussed above, there would be an additional photocurrent when the laser is focused near the free edges of the graphene flake. Figure 2.3 shows the experimental setup for the SPCM measurement setup under the out-of-plane magnetic field.

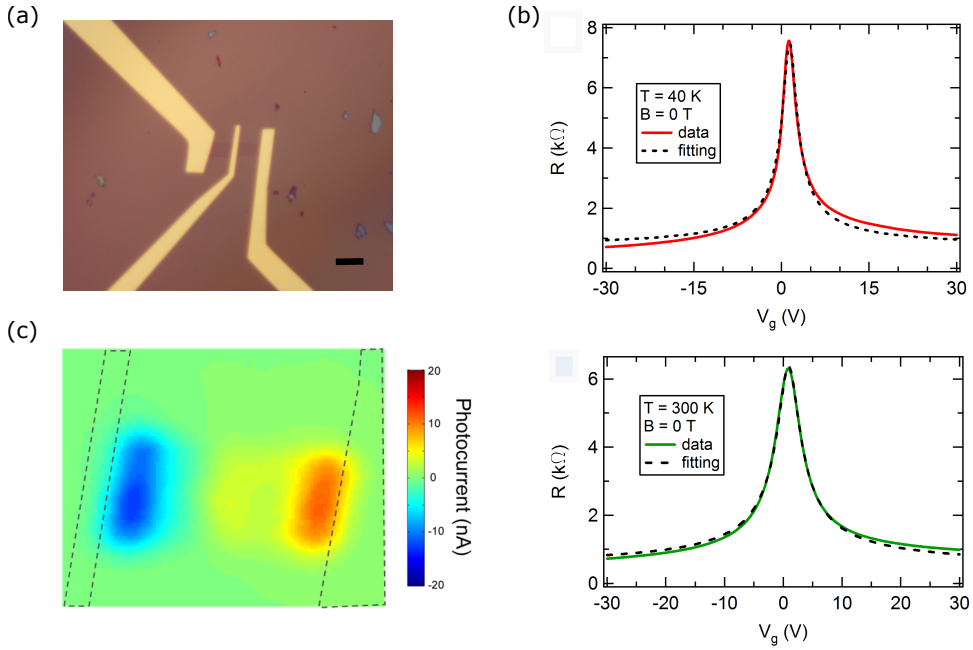

Figure 2.2: Graphene FET on SiO2 for scanning photocurrent microscopy. a, Optical image of a two-terminal graphene device, scale bar is 2 μm. b, Transfer characteristic of a two-terminal graphene device at T = 40 K, 300 K respectively. c, SPCM on the same two-terminal device at 40 K and zero magnetic field. $\lambda = 632\ nm$, $P = 40\ \mu W$.

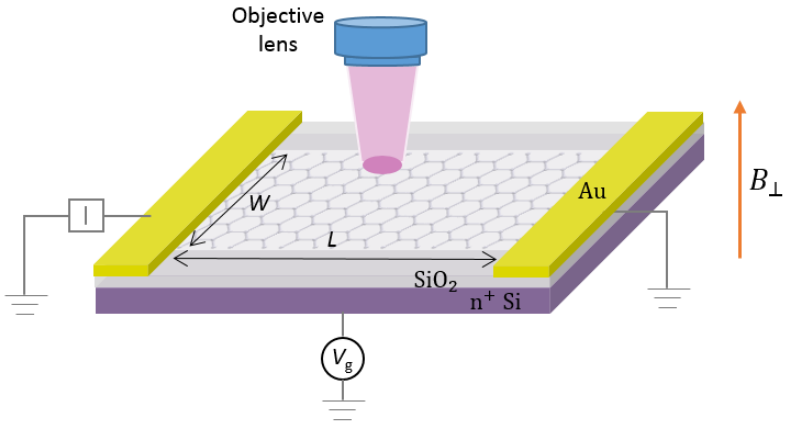

Figure 2.3: Experimental set-up and schematic structure of a graphene device

2.2.2 Chiral photocurrent generated on graphene edges

Far away from the metal contacts, when the laser is focused on one of the free edges, the photo excited electrons/holes will diffuse towards the other edge and the contacts. But due to the "left" and "right" symmetry, there would be no net photocurrent. However, if we apply a small out-of-plane magnetic field of 0.3 T, the electron/hole movement will be deflected and result in a SPCM map as Fig. 2.4b. From the 2D maps, one can see that except for the photocurrent near the metal contacts as in the zero field case, most of the additional photocurrent is generated when the laser is positioned on the two free edges. On the other hand, when we change the magnetic field from 0.3 T to -0.3 T, the photocurrent near the free edge would also reverse its sign. These observations are in complete agreement with the photo assisted thermal electric effect in graphene.

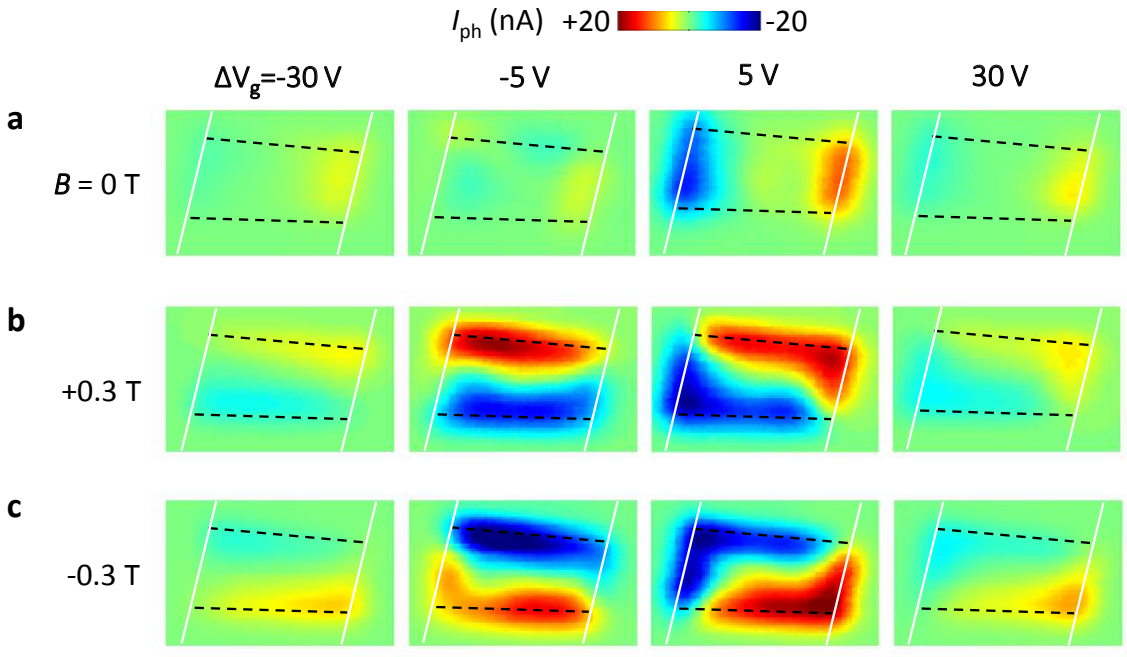

Figure 2.4: SPCM images for B = 0 (a), 0.3 T (b), -0.3 T (c) at varies gate voltages, T = 30 K.

At $\Delta V_g = 5\ V$, near the metal contacts, there is no sign change when we reverse the magnetic field, it's actually almost independent of the applied magnetic field. The same happens for other gate voltages, although the magnitude of the photocurrent is different for different gate voltages. In Fig 2.5a, b we show the symmetric and antisymmetric component of the SPCM with respect to the magnetic field at $\Delta V_g = 5\ V$. Clearly, we see the photocurrent generated near the metal contacts is due to the contacts effect (Schottky barrier), while the photocurrent near the free edges is all coming from the photo Nernst effect. Figure 2.5d is simulation of SPCM based on the Song-Levitov type long range photoresponse, as in equation 2.14. And Fig 2.5c is the photocurrent along the dashed line in b, we can see a good agreement between the simulation and experiment.

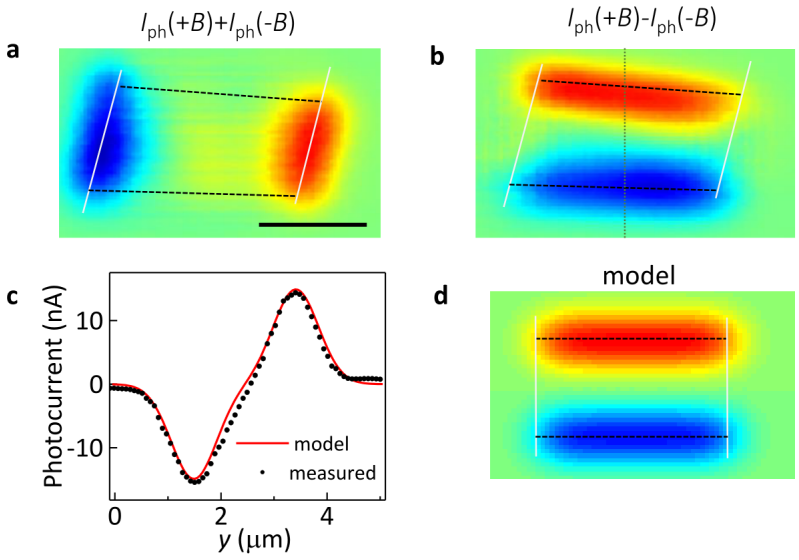

Figure 2.5: Analysis and modeling of the photo Nernst current at moderate magnetic field. a, b, B-symmetric and B-antisymmetric component of SPCM from Fig. 2.4b,c at $\Delta V_g = 5\ V$

2.2.3 Gate dependence of the Nernst photocurrent

Except for the spatial and magnetic field dependence, the photo Nernst current also shows a strong dependence on the gate voltage or carrier density as shown in Fig. 2.4. To better understand this gate dependence, we fixed the magnetic field at 0.3 T, and scanned the laser along the dashed vertical line in Fig. 2.5b while varying the gate voltage. The 2D map is shown in Fig. 2.6a. For fixed laser, the photocurrent switches its sign twice as we sweep the gate voltage from negative to positive values (see Fig. 2.6b). This gate dependence can be well explained by the analysis of the Nernst coefficient (equation 2.12) as in Fig. 2.6c.

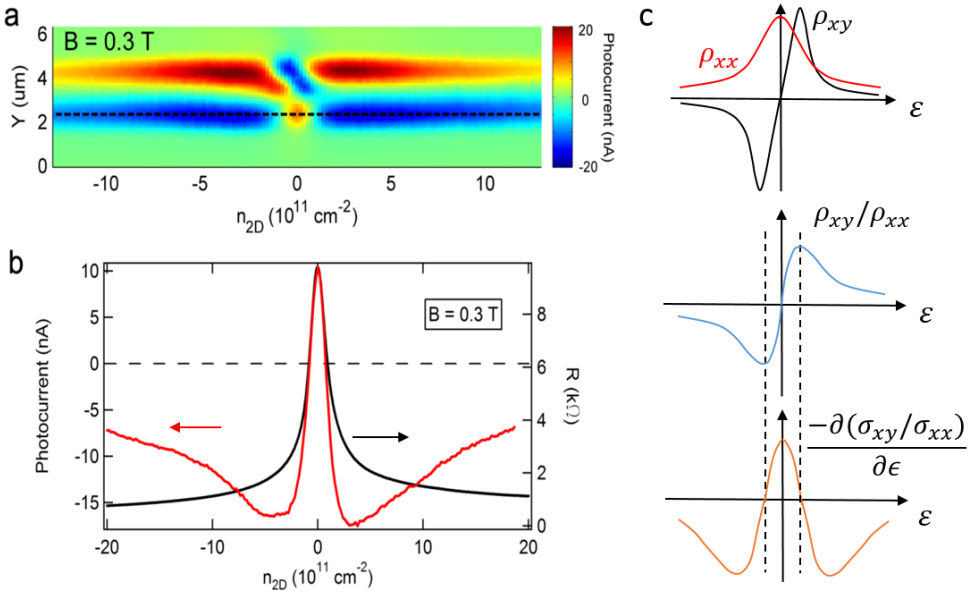

Figure 2.6: Carrier density dependence of the photocurrent at 0.3 T. a, Variation of the photocurrent along the dashed line in Fig. 2.4b as a function of the carrier density. b, Photocurrent along the line cut in a. c, Profile of the longitudinal and Hall resistivity as a function of the Fermi energy in the classical regime.

2.2.4 Photocurrent in the quantum regime

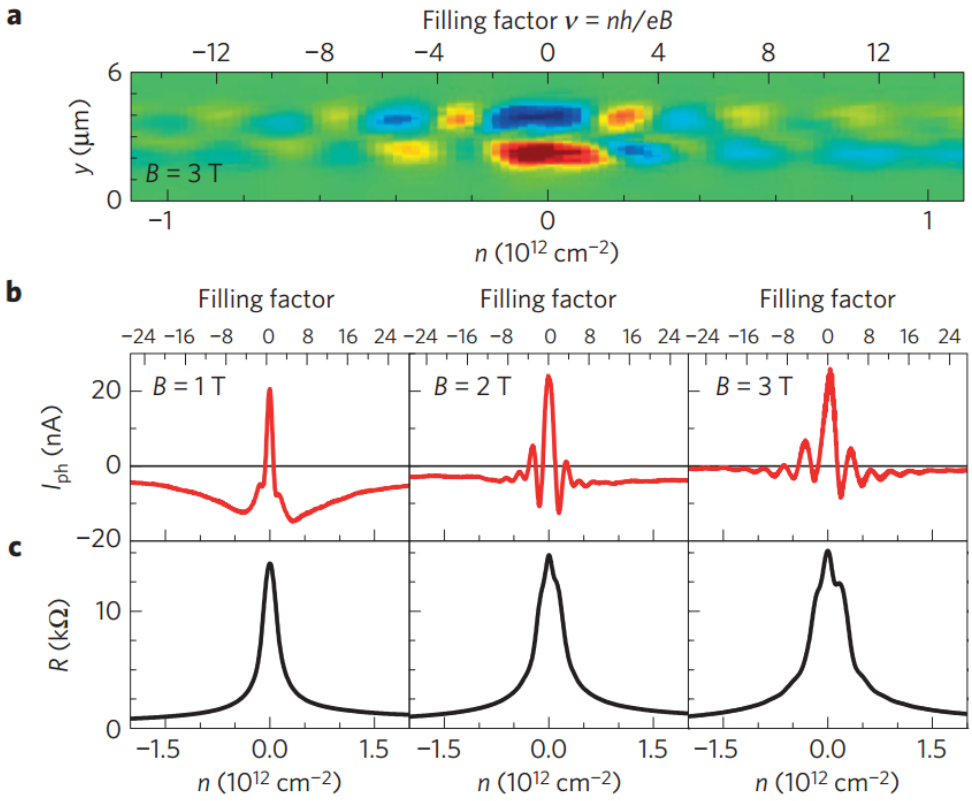

Figure 2.7: Carrier density dependence of the photocurrent in the quantum regime. a, Variation of the photocurrent along the dashed line in Fig 2.4b as a function of the carrier density at 3 T. b, c, Photocurrent and two-terminal resistance as a function of the carrier density at 1, 2 and 3 T respectively. For the photocurrent measurement, the laser is fixed at the center of one of the free edges.

One of the breakthroughs of the graphene studies is the observation of the quantum hall effect at relative high temperature and low magnetic field. Although the lowest accessible temperature in our experiment is ∼40 K, we were still able to see very weak quantum oscillations in two-terminal resistance above 2 T (Fig. 2.7c). The photocurrent in Fig. 2.7a

and b, however, shows a strong alternating of positive and negative values. Thus, the photo Nernst current act as a more sensitive probe of the formation of Landau levels and quasi particles. It is also clear from the Nernst coefficient in equation 2.12, which is expressed in terms of the derivative of the resistivity with respect to the Fermi energy.

2.3 Conclusion and Future Remark

As a summary, we demonstrated a new type of photocurrent generation by the photo Nernst effect in graphene in both classical and quantum regimes. By generalizing the Song-Levitov result on the long-range photocurrent response at zero magnetic field to a nonzero perpendicular field, we were able to capture almost all the features observed in experiment, including the spatial, magnetic field and carrier density dependences.

The magneto scanning photocurrent microscopy technique could also be used to probe spatial properties of a system, such as the homogeneity and domain structures. Different from conventional Nernst measurements, the device used in our experiment is much simpler, a two-terminal graphene device. On the other hand, in the quantum regime, the photo Nernst current is much more sensitive to the topology of the Fermi surface than regular transport measurements and can be utilized to study quasiparticle properties of materials with much short scattering time.

Chapter 3

TUNGSTEN DITELLURIDE - A COMPENSATED SEMIMETAL

3.1 Introduction to bulk WTe_2

Tungsten ditelluride (WTe_2) is a well-known non-magnetic layered semimetal [39, 40], and has been investigated for its thermoelectric applications [41]. Despite the recent broad interests in layered materials, other layered semimetals received much less attention compared to graphene, semiconducting and superconducting MX_2s. One of the main reasons is the complicated Fermi surfaces (up to 9 Fermi pockets have been reported [42]). Recently, Ali et al. [43] reported that orthorhombic WTe_2 crystal exhibits extremely large and non-saturating magnetoresistance at low temperature and high magnetic field, making it a candidate for low-temperature magnetic field sensors or high-field cryogenic temperature sensors. Beyond these potential applications, it also opens up a new field of searching for various kinds of semimetals [44–47] with large magnetoresistance.

The origin of this non-saturating magnetoresistance, however, is still not fully understood. It has been suggested [42, 48–53] to be related to the small overlap of the conduction and valence bands, and the near perfect charge compensation at low temperatures. Other papers suggested that spin-orbital coupling may also play an important role in determining the magnetoresistance of WTe_2 [42] and other semimetals [45].

On the other hand, Soluyanov et.al. [54] predicts that bulk WTe_2 in the orthorhombic structure, is a type-II Weyl semimetal (WSM). Weyl semimetals are a new type of quantum matter with nontrivial topological invariant as a analogy of 3D graphene or topological insulators. The electronic structure displays pairs of Weyl points connected by topological surface states (Fermi arcs). Several materials, including TaAs [48, 55, 56] and NbAs [57] have

been reported to be WSMs. To have nontrivial topology, either time reversal or inversion symmetry has to be broken. The Weyl points in this new type-II WSM appear at the contact of electron and hole pockets instead of the band edges. Soon afterwards, several groups claimed evidences of Weyl fermions in both ARPES [58–60] and transport measurements [61].

3.1.1 Lattice and electronic band structure

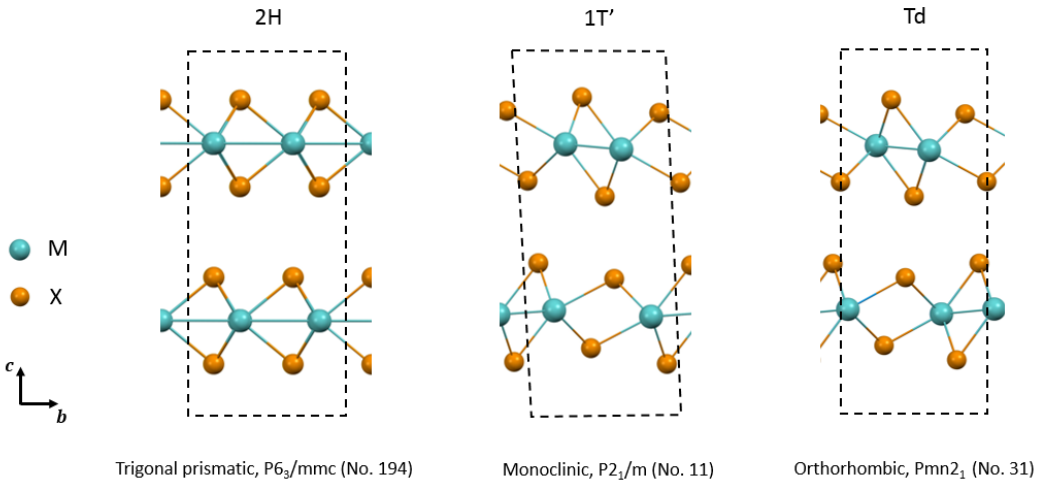

Figure 3.1: Schematic representations of 2H, 1T', Td crystal structures of bulk MX_2 along the bc plane respectively.

As mentioned in section 1.3.1, there are three different phases of monolayer MX_2. WTe_2 and $MoTe_2$ are usually stabilized at the 1T' phase, in which the transition metal atoms dimerize and form quasi one dimensional zigzag chains, as the red lines shown in Fig. 3.2c for WTe_2. Different from conventional bulk TMDCs, in which the 1H monolayers stack together forming the trigonal prismatic structure (2H), the 1T' monolayers can stack into bulk materials with two different crystal structures, monoclinic (1T') structure and orthorhombic (Td) structure (see Fig. 3.1). At room temperature in ambient conditions, bulk WTe_2 is usually stabilized

in the orthorhombic structure (space group $Pmn2_1$, No.31) as Fig. 3.2, the primitive unit contains four formula units. No structure transition is observed upon cooling to the cryogenic temperature for low pressures [43, 50, 62, 63]. $MoTe_2$, on the other hand, is more stable at the monoclinic phase [64–66] at room temperature.

For bulk WTe_2 in the orthorhombic structure, the inversion symmetry is broken although the 1T' single layer is centrosymmetric. This is the opposite to the case of most MX_2s in the 2H phase such MoS_2 and WSe_2, in which usually the bulk is centrosymmetric while the single layer is non-centrosymmetric. However, there are two reflection symmetries: a mirror in the bc plane m_{yz} and a glide plane in the ac plane g_{xz} formed by a reflection in the ac plane plus a translation by (0.5, 0, 0.5).

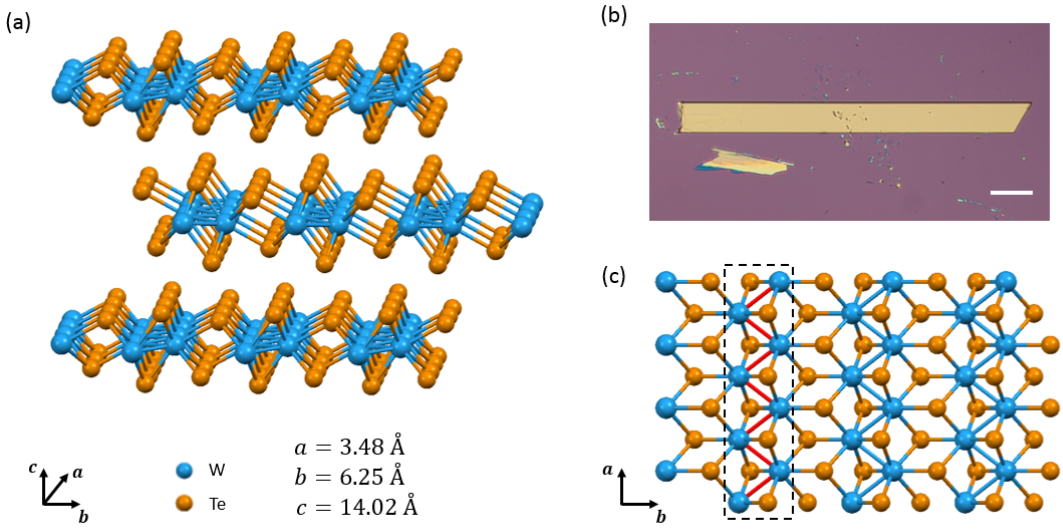

Figure 3.2: Atomistic structure of bulk and monolayer WTe_2. a, Side view of Bulk WTe_2 (only showing three layers) with orthorhombic stacking. The unit cell dimensions are: $a = 3.48$ Å, $b = 6.25$ Å, $c = 14.02$ Å. b, Optical image of a bulk WTe_2 crystal of about 100 nm thick, scale bar is 20 μm. c, Top view of monolayer WTe_2 in the 1T' phase, the red lines form a zigzag chain, which is the a axis.

In terms of the electronic structure, single particle DFT calculations [15, 43, 48] indicate that there is a small band overlap (negative gap) in both bulk and monolayer WTe_2 after taking spin orbital interactions into account. Figure 3.3 shows the dispersion relation and Fermi surfaces of bulk WTe_2 [43]. Near $E = E_F$, $k = 0$ (Γ point), the electron and hole bands cross each other. Therefore, intrinsically there would be electrons and holes coexisted in such system, i.e. it is a semimetal.

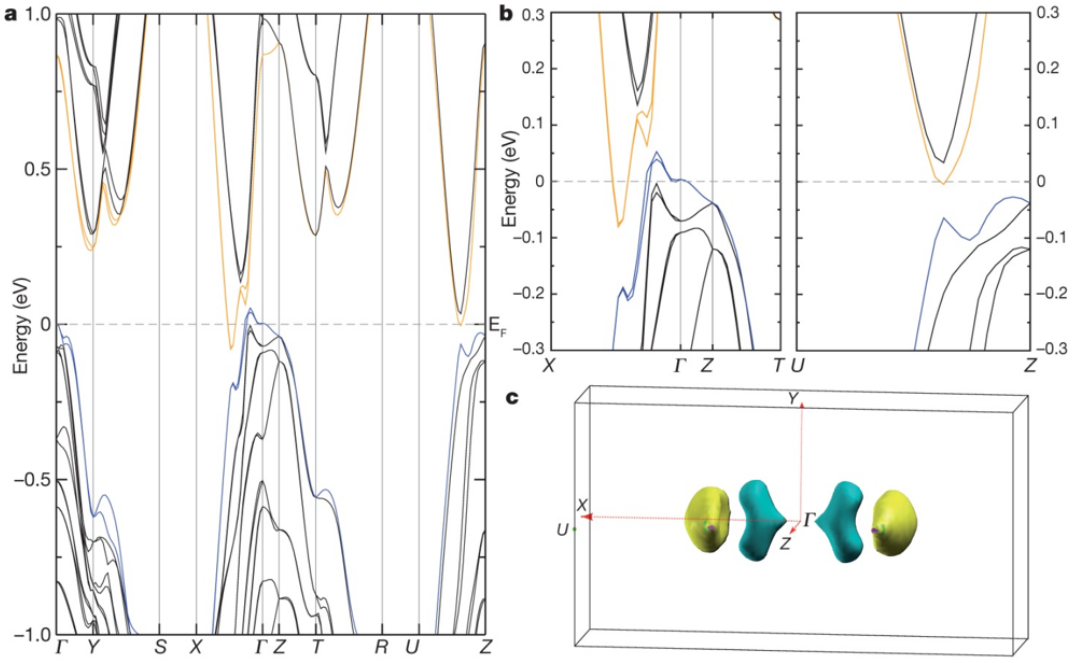

Figure 3.3: a, The dispersion relation of bulk WTe_2 for high-symmetry directions in the orthorhombic Brillouin zone. b, Details of the calculated electronic structures along ΓX and ΓZ directions. c, The Fermi surfaces of WTe_2, two electron (yellow) pockets and two hole (blue) pockets presented along the ΓX direction. (Figure taken from Ref. [43])

3.1.2 Extremely large magnetoresistance

We start the experiment by calibrating the flux-grown bulk crystals [67]. Figure 3.4 shows the magnetoresistance ($MR = \frac{R_{xx}(B)-R_{xx}(B=0)}{R_{xx}(B=0)}$) as a function of the out of plane magnetic field measured on a 100 nm thick single-crystal WTe_2 at 7 K. A constant current of 100 nA is flowed along the a-axis for the four-terminal measurements. At B = 7 T, the magnetoresistance is about $80,000\%$, very close to the reported data [43] at the same temperature.

As suggested by many groups, this large, non saturating magnetoresistance is due to the perfect charge compensation in the bulk WTe_2 crystal at extremely low temperatures. According to the classical two-fluid (electron and hole fluid in this case) model.

$$\rho_{xx} = \frac{1}{e}\frac{n\mu_n + p\mu_p + (n\mu_p + p\mu_n)\mu_n\mu_p B^2}{(n\mu_n + p\mu_p)^2 + (p-n)^2\mu_n^2\mu_p^2 B^2}, \tag{3.1}$$

$$\rho_{xy} = \frac{1}{e}\frac{(p\mu_p^2 - n\mu_n^2)B + (p-n)\mu_n^2\mu_p^2 B^3}{(n\mu_n + p\mu_p)^2 + (p-n)^2\mu_n^2\mu_p^2 B^2}. \tag{3.2}$$

The magnetoresistance is

$$MR = \frac{\rho_{xx}(B) - \rho_{xx}(B=0)}{\rho_{xx}(B=0)} = \frac{np(\mu_n + \mu_p)^2\mu_n\mu_p B^2}{(n\mu_n + p\mu_p)^2 + (p-n)^2\mu_n^2\mu_p^2 B^2} \times 100\%.$$

For perfect charge compensation, $n = p$, $MR = \mu_n\mu_p B^2 \times 100\% \propto B^2$. The magnetoresistance is a quadratic function of the external magnetic field, and will not saturate. The magnitude of the magnetoresistance is determined by the mobilities of electrons and holes.

In the log-log plot as in the inset of Fig. 3.4, the magnetoresistance indeed can be fitted into a power law of the applied magnetic field ($MR \propto B^\alpha$). However, the best fit gives $\alpha = 1.76$, which is inconsistent with two-fluid model with $n = p$. This sub quadratic magnetic field dependence is also observed by other groups in both bulk [43, 61, 68] and thin layer WTe_2 [69]. Moreover, anisotropic linear magnetoresistance [67] and exotic spin texture [42] indicate other factors, such as electron hole correlation and strong spin-orbital interaction may play important roles in the unusual magnetoresistance in bulk WTe_2.

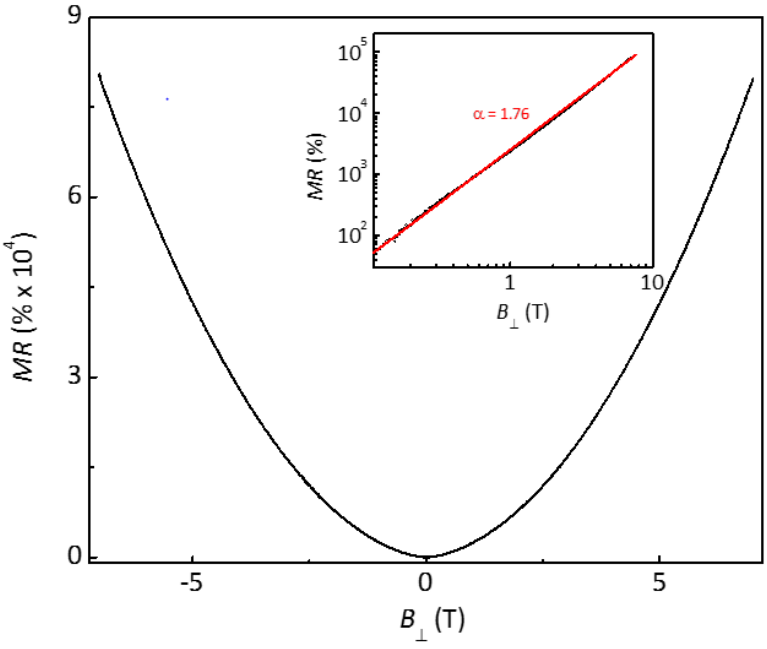

Figure 3.4: Magnetoresistance of Bulk WTe_2 at 7 K. The bulk WTe_2 is about 100 nm thick, current flows along the a axis. Inset shows the same plot in log-log scale, red curve is the power law fitting.

3.1.3 Electrical characterization of in-plane anisotropy

In the previous section as well as in literatures, for magnetoresistance measurements in bulk single-crystal WTe_2, current is always flowed along the a-axis. Due to the dimerization of the W atoms, one would expect a large in-plane anisotropy in such system. An example is the complicated polarization dependent Raman spectroscopy, as discussed in Appx. B. Another is the report of linear magnetoresistance when the magnetic field is along the b-axis [67]. In this section, we are going to compare the case of current flowing along a- with b-axis while always keeping the magnetic field pointed out of the sample plane.

Figure 3.5 shows the four-terminal resistance as a function of temperature and magnetic field for current flowing along a- versus b-axis. At high temperatures, the anisotropy is weak

and does not vary much with temperature. However, when it approaches the lowest temperature of the system (7 K here), the resistance ratio (R_b/R_a) starts to diverge, indicating different scattering rates for different axes at low temperatures. On the other hand, the anisotropy vanishes for $B > 1\ T$, as shown in Fig. 3.5d.

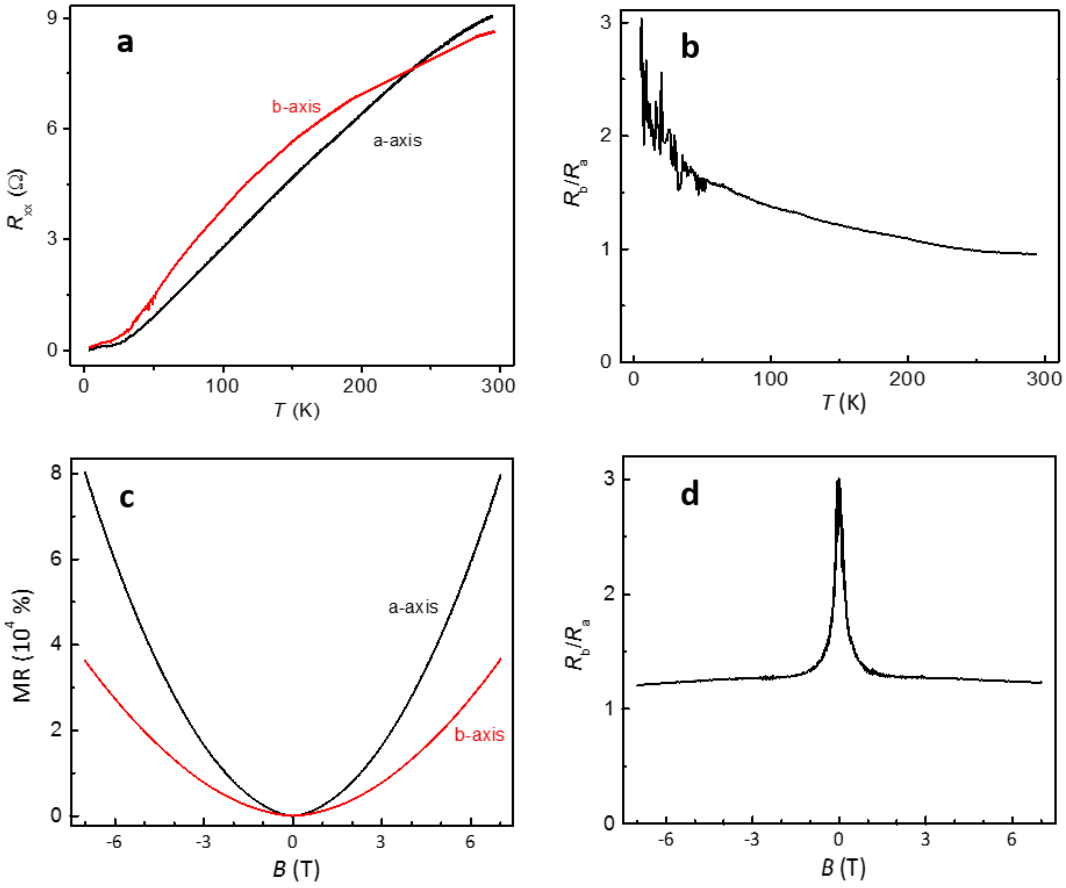

Figure 3.5: a, Four-terminal resistance as a function of temperature for current flow along a- and b- axis respectively. b, Temperature dependence of the four-terminal resistance ratio (R_b/R_a). c, Magnetoresistance as a function of the magnetic field. d, Magnetic field dependence of R_b/R_a.

3.1.4 Pressure driven superconductivity

In addition to the exotic large magnetoresistance and possible Weyl physics, bulk WTe_2 has also been demonstrated to superconduct under high pressure by several groups [62, 63, 70]. Upon increasing the pressure, in the phase diagram, a superconducting dome is observed. Figure 3.6 shows the resistance as a function of T at zero magnetic field for different pressures. Transitions from metallic to superconductivity and then back to metallic state are observed as the pressure increases. Structure analysis using X-ray diffraction and Raman spectroscopy indicates the change of the lattice constants or shrinkage of the volume when pressure increases. At low pressure ($< 4 - 5\ GPa$), the density of state at the Fermi surface increases tremendously. At high pressure, some groups [70, 71] claim a structure transition from Td to 1T' is observed accompanying the emergence of superconductivity. It is worth mentioning that the 1T' structure is centrosymmetric, prohibiting any WSM state.

If the structure transition from Td to 1T' is really responsible for the emerging of superconductivity in W(Mo)Te_2, it would be very interesting to see signs of superconductivity in non-pressurized monolayer WTe_2, which is in the 1T' phase generically.

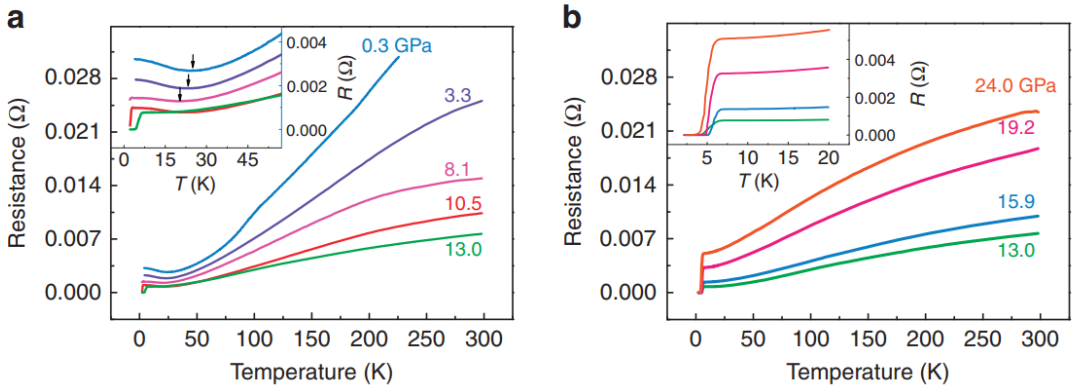

Figure 3.6: Electrical resistance of single-crystal WTe_2 as a function of temperature at different pressures, from 0.3 to 13.0 GPa (a) and from 13.0 to 24.0 GPa (b). The insets are enlarged views of the low temperature part. (Figure adapt from Ref. [62])

3.2 Thickness dependence and degradation of ultra thin layers

In the last section, we talked about the extremely large magnetoresistance in bulk WTe_2, which is related to but cannot be simply explained by the perfect electron and hole compensation in such system. A better and reversible control of the carrier imbalance is thus crucial for understanding the exotic magnetoresistance. This could be achieved by thinning it down to the atomically thin limit. In the monolayer, the electron and hole carrier density is predicted [48] to be $n = p = 1.6 \times 10^{13}\, cm^{-2}$, which can be accessed simply by applying an electrostatic gate.

In Table 3.1, we show the space group and the symmetry operations of WTe_2 from bulk to the monolayer. The change of the symmetry is key for understanding many transport and optical phenomena in such system, including the Weyl physics, second harmonic generation and ferroelectric behavior.

	1-layer WTe_2	N-layer WTe_2 ($N \geq 2$)	bulk WTe_2
Space group	$P2_1/m$	Pm	$Pnm2_1$
Point group	C_{2h}^2	C_s^1	C_{2v}^7
Symmetry operation	(x,y,z); (-x,-y,-z); (1/2-x,y,z)	(x,y,z); (-x,y,z)	(x,y,z);(-x,y,z); (1/2-x,-y,1/2+z); (1/2+x,-y,1/2+z)

Table 3.1: Symmetry analysis for monolayer, N-layer ($N \geq 2$) and bulk WTe_2. (Adapted from [72])

3.2.1 Metal-insulator transition in the atomic thin limit

In Fig. 3.7, we show the temperature dependence of sheet resistivity in WTe_2 devices of different thickness, ranging from 100 nm to three atomic layers ($3L$). All devices are built on SiO_2 substrate in ambient conditions. As is clear in the figure, there is a metal to insulator

transition as layer thickness is reduced, consistent with the literature [35]. For trilayer devices, as the temperature decreases the resistivity increases, indicating an insulating behavior below about 3 layers.

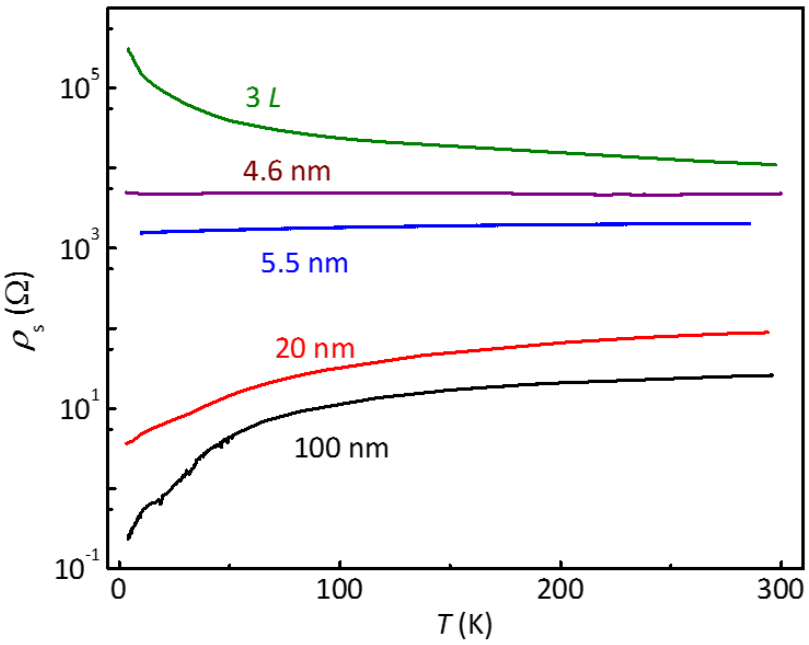

Figure 3.7: Temperature dependence of sheet resistivity (per square) in non-encapsulated WTe_2 devices of different thickness, from 100 nm thick down to a trilayer.

However, monolayer and bilayer WTe_2 devices built on SiO_2 are usually not stable over time. In fact, for WTe_2 flakes thinner than four layers, we found they could degrade within a day in ambient conditions, similar to a lot of other air sensitive 2D materials [73–75]. Figure 3.8 shows optical images of a monolayer piece took right after exfoliation and after keeping in air for one day. One can see a clear change of optical contrast before and after degradation. In Chap. 4, we will start by introducing a new technique of protecting the thin films from degradation, i.e. by encapsulating them in hexagonal boron nitride (hBN) in a nitrogen atmosphere. After encapsulation, we will show that trilayer is still semimetallic,

while monolayer and bilayer devices are insulating near the charge neutrality.

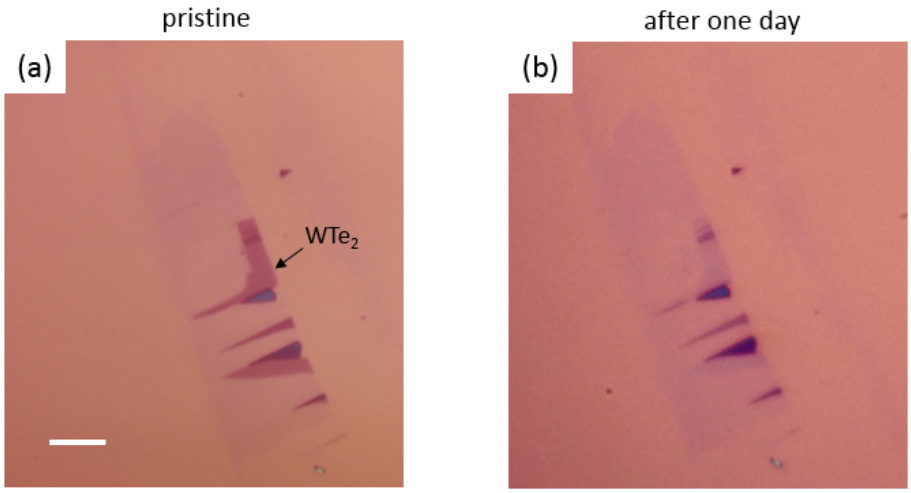

Figure 3.8: Optical images of monolayer WTe_2 as exfoliated (a) and in ambient condition for 4 hours (b). Scale bar is 5 μm

3.2.2 Magnetoresistance of few-layer WTe_2

While WTe_2 changes from metallic to insulating as thinned down to the monolayer, the magnetoresistance also decreases dramatically. Except for the the sudden fallen of the electron and hole mobilities, the underlying predominant mechanism for the magnetoresistance also changes. For example, quantum interference starts to play a more and more important role for WTe_2 below ~10 layers on SiO_2 [35, 76].

In Fig. 3.9, we show the magnetoresistance of a representative few-layer (4.5 nm thick) WTe_2 device. At $V_g = 0$, $T = 1.6\ K$, the magnetoresistance displays a dip or a V-shape feature around $B = 0$. This is very different from quasi-parabolic behavior (U-shape) in the bulk crystals, and cannot be explained by the two-fluid model. A lot of research have been focused on this regime, and it has been shown that this can be understood as a result of the weak antilocalization due to the strong spin-orbit interactions in the material [35, 76].

More intriguingly, as shown in Fig. 3.9c, in this regime the magnetoresistance can be tuned from positive to negative values by the applied electric field (gate voltage). Such weak antilocalization to weak localization transition has also been observed in other systems including the interface of $LaAlO_3/SrTiO_3$, and were explained by gate tunable Rashba spin-orbit interactions [76, 77].

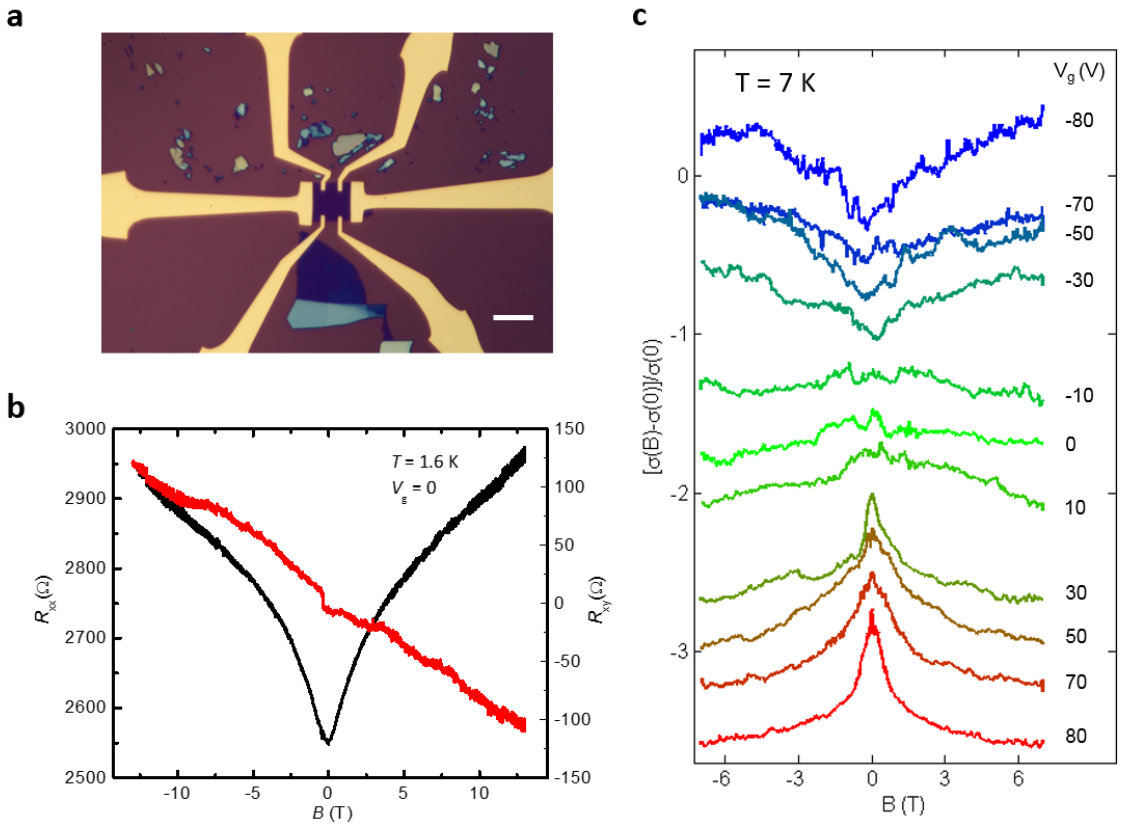

Figure 3.9: a, Optical image of a few-layer (4.5 nm) WTe_2 device made on SiO_2 substrate. Scale bar is 5 μm. b, The longitudinal (R_{xx}) and Hall resistance (R_{xy}) as a function of the magnetic field (out-of-plane) at $T = 1.6\ K$, $B = 0$. c, Magneto conductance ($MC = [\sigma(B) - \sigma(0)]/\sigma(0)$) as a function of the magnetic field at different gate voltages on another device of the same fashion. The magneto conductance for different gate voltages are plot with offset. $T = 7\ K$.

3.3 *Nontrivial topology in monolayer WTe_2*

In 2014, Qian et.al. predicted [15] that monolayer MX_2 (M = Mo, W; X = S, Se, Te) in the 1T' phase is a quantum spin hall insulator, characterized by Z_2 topological invariant ($Z_2 = 1$), if there is a band gap. However, from the material perspective, most of these MX_2s favor the 1H phase energetically. WTe_2 is an exception, but single particle calculation [15, 48] shows it's a semimetal rather than gapped even in the monolayer limit.

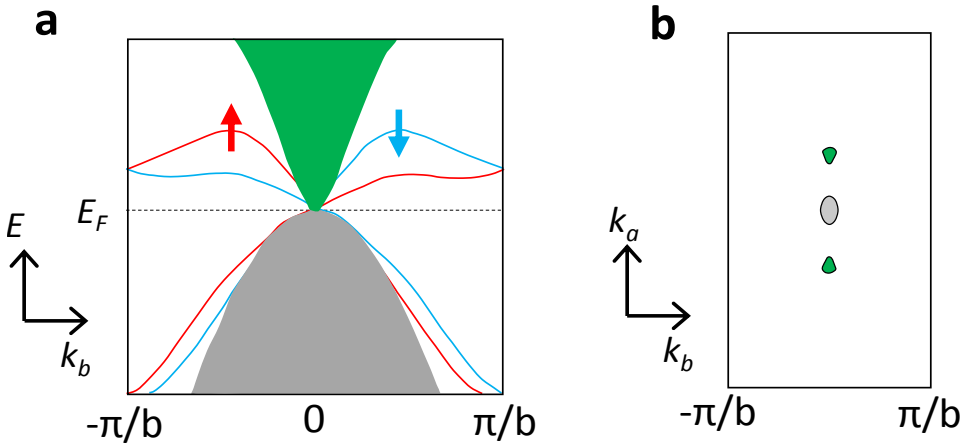

Figure 3.10: a, Band structure of monolayer WTe_2. Red and blue lines corresponds to the spin polarized edge states. b, Fermi surface of the monolayer WTe_2, which is made of a hole pocket centered at the Γ point and two electron pockets centered along the ΓX axis.

The band structure for monolayer WTe_2 is illustrated in Fig. 3.10. In the band diagram, the valence band mainly consists of the 5d-orbitals of the W atoms, while the conduction band mainly consists of the 5p_y-orbitals of the Te atoms. Due to the additional distortion of the W atoms, the 5d-orbitals will be lowered, leading to the band inversion. Due to the small overlap of the conduction and valence band, the inner part of the monolayer (monolayer bulk) will be semimetallic, and hybridize with the edge bands, making the separation and detection

of the edge states very challenging. Thus, to make a quantum spin hall insulator (QSHI) or topological field effect transistor, the application of a tensile strain is suggested [15] to open up a gap in the bulk bands. However, as we will show in Chap. 4, in experiment the interior of the monolayer WTe_2 is already insulating without applying any external strain. Consequently, WTe_2 is a possible generic QSHI.

Chapter 4

TOPOLOGICAL INSULATOR BEHAVIOR IN MONOLAYER WTe_2

4.1 Intrinsic transport of atomic thin WTe_2

In the last chapter, we discussed that WTe_2 flakes thinner than four layers can degrade very fast in ambient conditions, causing inconsistency between devices. To probe their intrinsic electrical properties, one needs to protect them from oxygen and water vapor, especially during the fabrication processes. The technique we adopted is encapsulating them between two hexagonal boron nitride (hBN) flakes in an oxygen-free glovebox, which has already been proven to be an effective way in several other systems [73, 74, 78].

4.1.1 Device fabrication: hBN encapsulation

We start the fabrication by pre-defining platinum (Pt) electrical contacts on a hBN flake (bottom hBN), which is identified on a SiO_2/Si substrate. Thin flakes of WTe_2 are cleaved from the bulk crystals inside a glovebox (O_2 and water vapor levels are both lower than 0.5 ppm). 1-3 layers of WTe_2 are identified and latter confirmed using atomic force microscopy (AFM). The flake is quickly encapsulated between the bottom Pt/hBN and another piece of hBN flake (top hBN). Then another step of e-beam lithography and metalization (Au) are used to pattern the electrical pads. The top graphite gate is transferred either at the last step or before picking up the top hBN. Figure 4.1 shows the schematics of the fabrication processes and images of a representative encapsulated monolayer WTe_2 device (MW2). Table 4.1 lists the thicknesses of the upper hBN, lower hBN, and the top graphite used for all five devices we are going to report in the following chapters, including three monolayer devices MW1, MW2, MW3, one bilayer device BW1 and one trilayer device TW1.

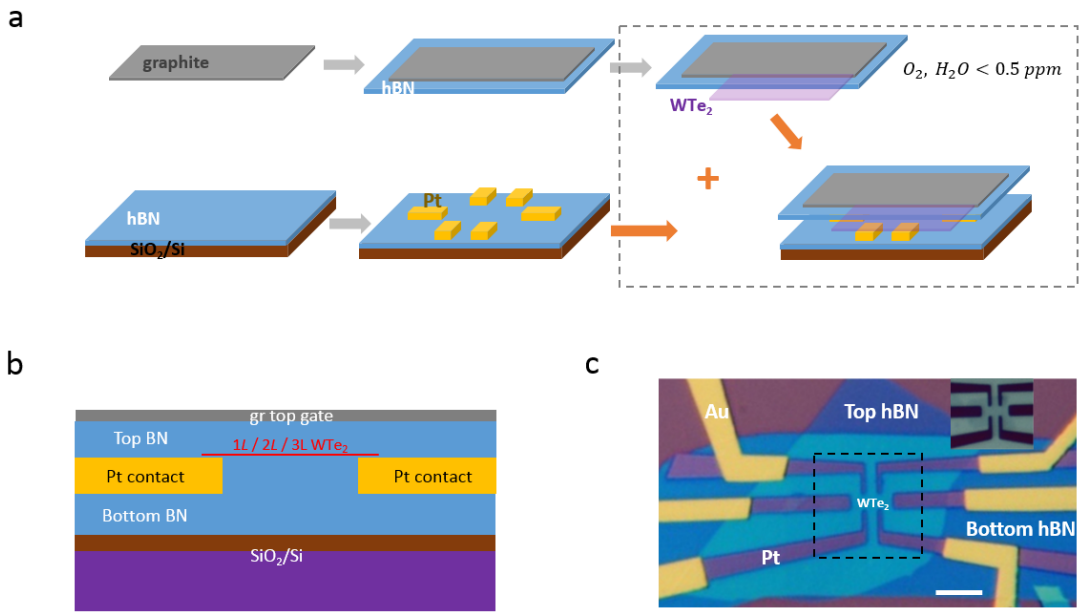

Figure 4.1: a, Schematics of the fabrication processes. b, Schematic of an encapsulated WTe_2 device. c, Optical image of a representative encapsulated monolayer WTe_2 device (MW2), the top right inset is a closer look at the dashed rectangular part in the main figure. Scale bar is 5 μm.

Device label	upper hBN (nm)	lower hBN (nm)	top graphite (nm)
MW1	5.8	18	3
MW2	9.2	17.5	4.1
MW3	11.4	14	3.4
BW1	5.4	30	3.3
TW1	5.5	22.6	4

Table 4.1: Thickness of the upper hBN, lower hBN, and the top graphite used for device MW1, MW2, MW3, BW1(bilayer) and TW1(trilayer). All thicknesses were obtained from the AFM image.

4.1.2 Temperature dependence of the two-terminal conductance

The transfer characteristics of WTe_2 devices from trilayer to the monolayer are shown in Fig. 4.2. For each curve, the temperature is fixed, from 300 K to 1.6 K. It is also worth mentioning that a small dc bias of 3 mV is applied on top of the 100 μV ac excitation in the two-terminal measurements to suppress the zero bias anomaly (ZBA), which only affects the bilayer and monolayer below ∼10 K and will be discussed later (see Appx. C for details of the linear responses).

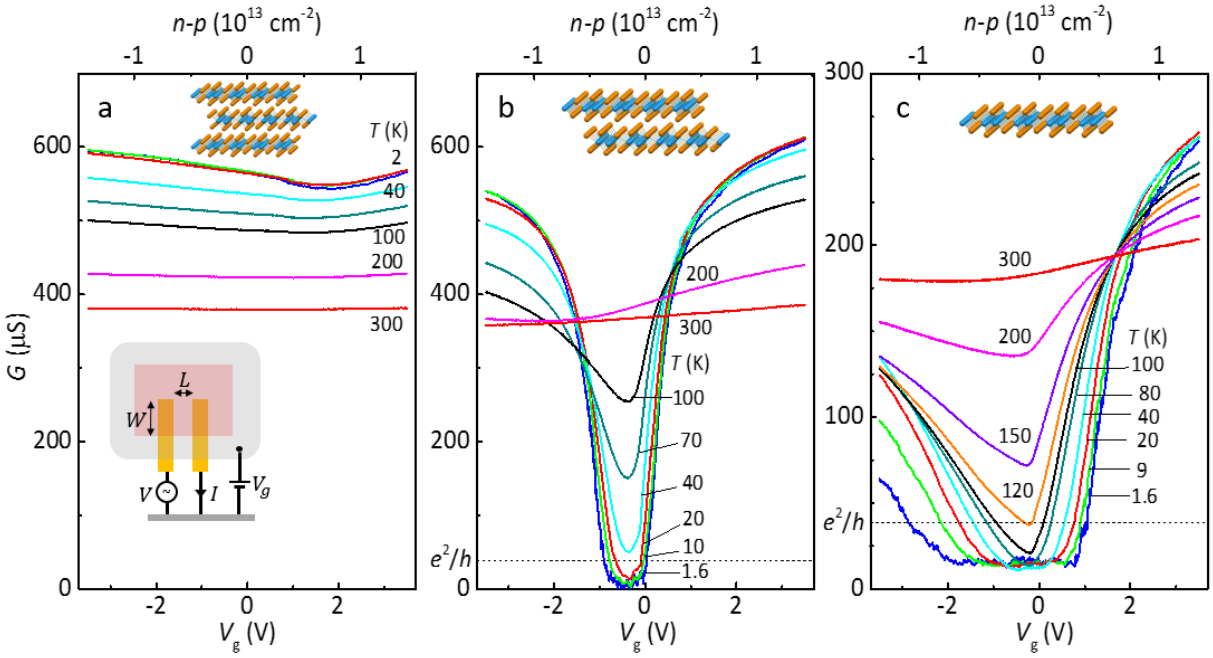

Figure 4.2: Two-terminal characteristics of encapsulated trilayer (a), bilayer (b) and monolayer (c) WTe_2 devices. All three devices have similar dimensions. Trilayer (TW1): $L = 0.2\ \mu m$, $W = 3.4\ \mu m$; bilayer (BW1): $L = 0.26\ \mu m$, $W = 3.1\ \mu m$; monolayer (MW1): $L = 0.2\ \mu m$, $W = 3.4\ \mu m$. The inset of (a) shows the schematic configuration of the two-terminal measurement, in which the pink region is the WTe_2, a gate voltage is applied between the top graphite gate and drain contact on WTe_2. In all three devices, the conductance $G = I/V$ is measured at a small dc bias of 3 mV.

For the trilayer device as shown in Fig. 4.2a, as the temperature decreases, the conductance increases in general, with a weak gate dependence, indicating a metallic temperature dependence at all gates. This agrees with the temperature dependence of bulk WTe_2 devices [43] and a recent report on trilayer devices [69], but is very different from the trilayer devices built on SiO_2 substrate as in Fig. 3.7, which shows a clear insulating temperature dependence even in the four-terminal configuration.

However, for the bilayer device the transfer characteristics are very different, especially at low temperatures. To begin with, for small gate voltages near charge neutrality, the bilayer behaves like an insulator, i.e. the conductance decreases as the temperature decreases. Secondly, below $\sim$ 100 K the gate dependence develops a cusp feature near the conductance minimum. The conductance minimum keeps decreasing as we lower the temperature and reaches zero at $\sim$ 10 K, below which the gate range for zero conductance starts to broaden. Thirdly, far away from charge neutrality at very large doping, the temperature dependence becomes metallic again, implying a gate tunable metal to insulator transition.

In the monolayer limit as shown in Fig. 4.2c, the temperature dependence looks very similar to the bilayer case in general. However, one of the key difference is that the conductance minimum stops at a finite positive value ($\sim 16\ \mu S$) at about 100 K, and develops a conductance plateau as we keep decreasing the temperature. At the same time, the width of the plateau is much wider than the bilayer case (for zero conductance) at the same temperatures.

For the rest of the chapter, we will focus on understanding the exotic transport properties of monolayer WTe_2. We will show that the non-vanishing conduction in the monolayer at low temperature near charge neutrality is due to the existence of edge conduction, while the bulk becomes insulating as in the bilayer but at a higher temperature of $\sim$ 100 K. We will also talk about the properties of this edge conduction, including temperature and magnetic field dependences as well as the non-linear behavior (zero bias anomaly). Most of these observations seem to indicate monolayer WTe_2 is a quantum spin Hall insulator.

4.2 Edge conduction in monolayer WTe_2

4.2.1 Nonlocal transport

Edge conduction is usually detected using a nonlocal measurement, such as in the HgTe/CdTe quantum wells [79]. Figure. 4.3 shows the nonlocal signal as a function of the gate voltage at different temperatures on the monolayer Hall bar shape device (MW2, see Fig. 4.1a for the optical image). As shown in the inset, a small excitation of 100 μV is applied between contact 2 and 6, and we measure the nonlocal voltage drop across contact 4 and 5. At room temperature, the nonlocal voltage to excitation ratio (V_{nl}/V_0) is almost independent of the gate voltage and is only about 5%, indicating a bulk dominated conduction between contact 2 and 6. Figure. 4.3b is the simulation of the potential distribution for the geometry approximating the real device. Here we assume the conductivity is isotropic, and the electric potential satisfies the Laplace equation. The dashed rectangles represents the metal contacts. All contacts except the source and drain are floated, implying constant potential and vanishing net current as the boundary conditions on these contacts. The simulated nonlocal to excitation ratio is $\sim 10\%$, in reasonable agreement with the ratio we measured at room temperature, considering the uncertainties of the exact monolayer shape and the in-plane anisotropy of the conductivity.

As the temperature decreases, the nonlocal signal increases for most gate voltages, and peaks near $V_g = 0$. When the temperature approaches the base ($T = 1.6\ K$), the nonlocal signal near the charge neutrality saturates to $\sim 100\%$. This is obviously in contradict to the isotropic bulk conduction, and can be explained by the existence of some kind of edge conduction. For $T < 100\ K$, the 2D bulk near the charge neutrality becomes insulating, while the edge remains conducting. If all edges are ideal helical edges, one would expect the nonlocal signal ratio to saturate to $V_{nl}/V_0 = 1/4$. However, experimentally we found a large variance between different devices or different edges of the same device although they have similar lengths. In this particular device, when we apply a small ac bias between contact 4 and 5 while shorting the longer edge by grounding contact 1, the current is almost negligible

for small doping when it approaches the base temperature. This particular "broken" edge and the fact that the other edges are non ideal makes the Landauer Büttiker type analysis not applicable. More discussions on the non-ideal edge will be made in later sections.

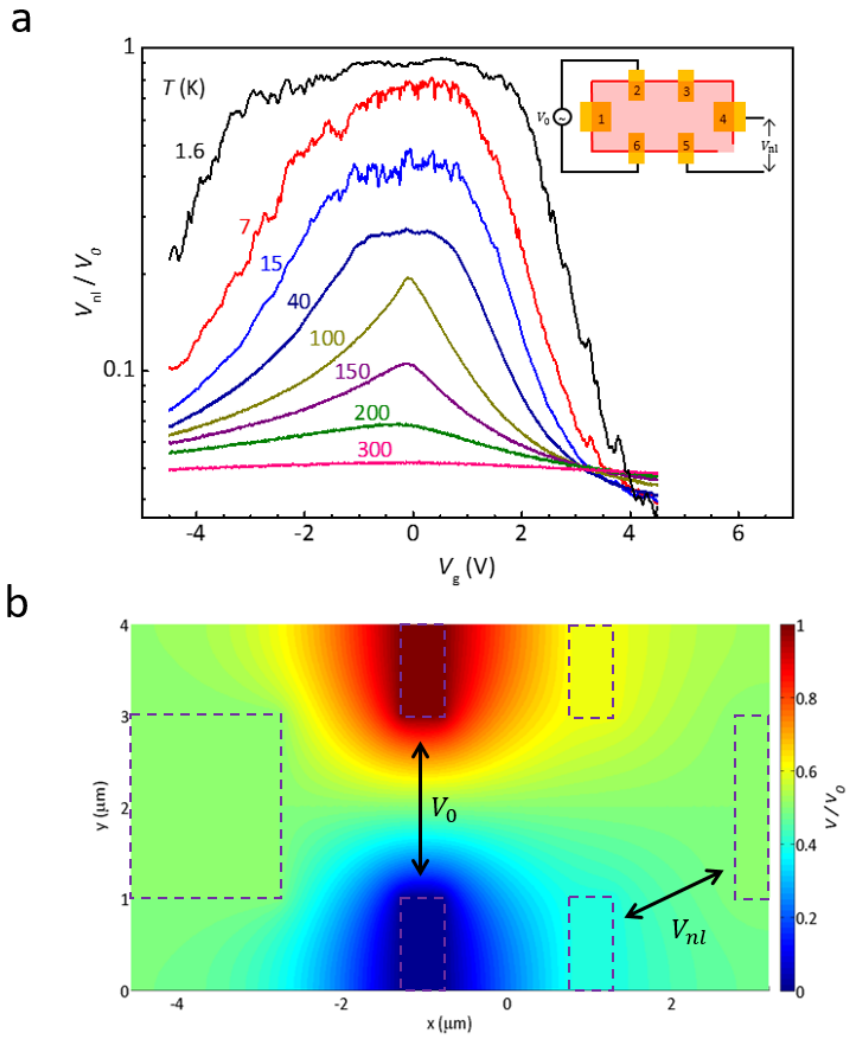

Figure 4.3: a, Nonlocal voltage to excitation ratio as a function of gate voltage at different temperatures. Inset is the configuration of the measurement. b, Simulation of the electrostatic potential distribution for the Hall bar shape device, the dashed rectangles represent the metal contacts.

4.2.2 Distinguishing edge and bulk conduction

Although the global nonlocal measurements strongly indicates that a substantial current flows along the edge for small doping at low temperatures, quantitative separation of the bulk and edge contribution is not possible especially when the edges are not ideal. A clearer and more direct experiment was performed on the same device as shown in Fig. 4.4.

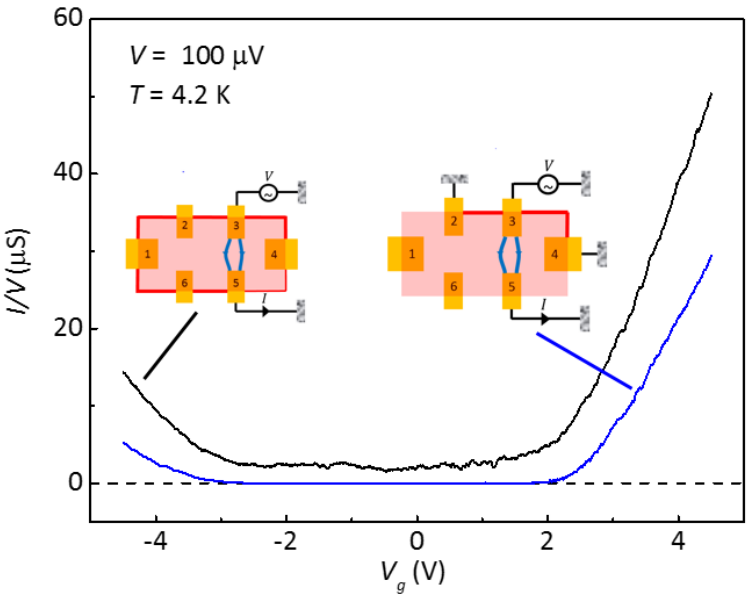

Figure 4.4: Two-terminal conductance measurements on the Hall bar shape device at T = 4.2 K. The black and blue curves are measured without and with the side contacts grounded respectively. The insets show the two measurement configurations, in which the pink rectangles represent the WTe_2 flake.

We compared the two-terminal conductance (I/V) between contact 3 and 5 for two different configurations at T = 4.2 K. In the first case (black trace), when we floated all the other contacts the two-terminal conductance as a function of V_g looks very similar to the transfer characteristic of Fig. 4.2c, except now there is no dc bias. In the second case (blue trace), when we grounded contacts 2 and 4 the overall conductance is suppressed. More

importantly, near charge neutrality ($2\ V > V_g > -3\ V$), the conductance is immeasurably small, indicating that the bulk is completely insulating and the non vanishing conductance in the black trace for the same gate range is all conducted through the edges. When $V_g > 2\ V$ or $V_g < -3\ V$, the bulk is turned on, and starts to dominate the two-terminal conduction. This experiment also suggests a way to measure the edge and 2D bulk conduction separately.

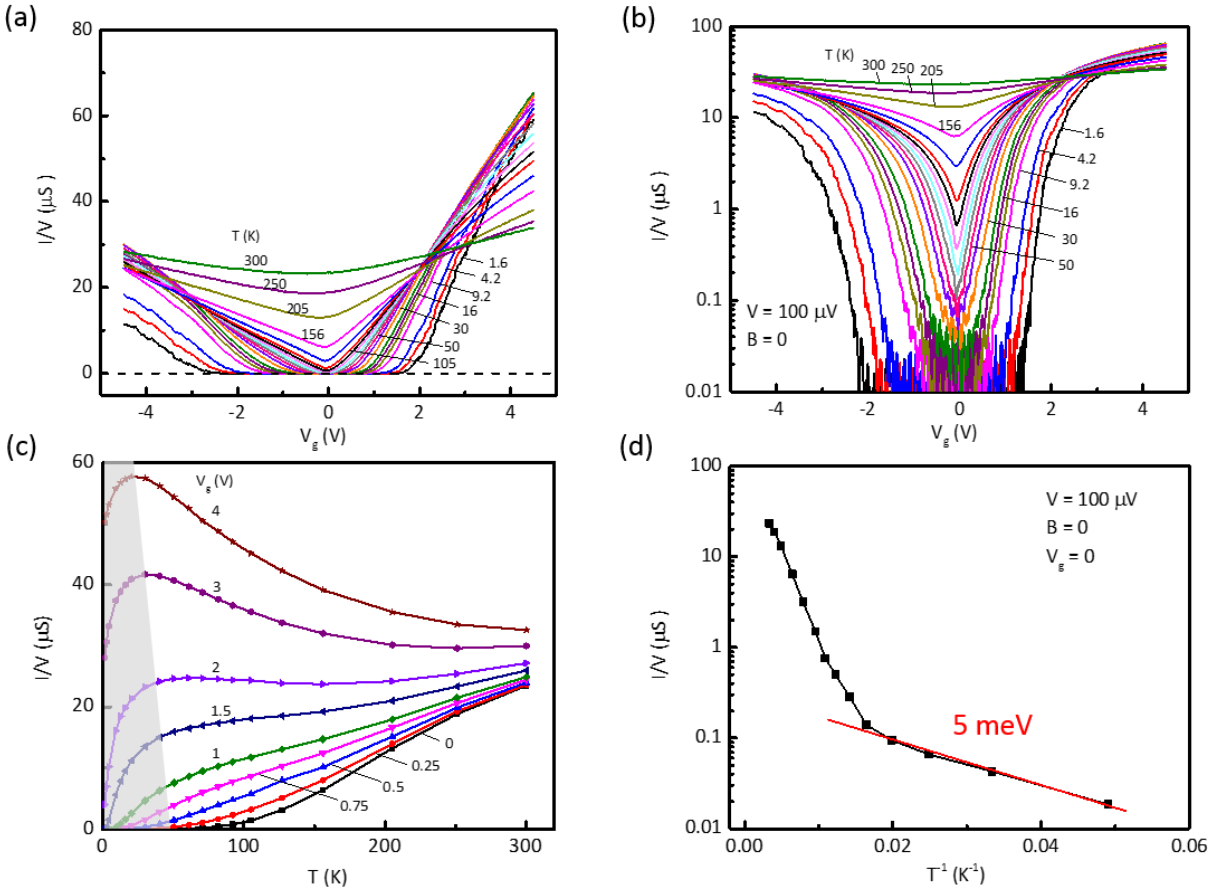

Figure 4.5: Temperature dependence of the 2D bulk in monolayer WTe_2. a-b, Two-terminal conductance for the 2D bulk as a function of V_g for fixed temperatures, in linear (a) and log scale (b) respectively. c, Two-terminal conductance as a function of T at fixed V_g. The shaded area corresponds to the freezing of the contacts to the bulk. d, Arrhenius plot of the 2D bulk conductance at $V_g = 0$.

Figure 4.5 shows the ambipolar transfer characteristics of the monolayer 2D bulk at different temperatures after shorting the edge current by grounding contacts 2 and 4, which has a weak effect on the bulk conduction. On cooling from 300 K, the monolayer bulk start to develop a "V" shape gate dependence with a sharp minimum around $V_g = 0$ at around 200 K. Below 200 K, the "V" grows sharper and the minimum keeps decreasing. At about 100 K, the minimum touches zero conductance and gets wider and wider afterwards. From 200 K to 30 K, there is a well-defined gate tunable metal to insulator transition, with critical gate voltage at $V_g \approx 2\ V$ on the n-side and $V_g \approx -3\ V$ on the p-side. Below 30 K, the gate dependence deviates from the well-defined behavior. For further investigation, we plot the temperature dependence at representative gate voltages in Fig. 4.5c. This figure shows a clear metal to insulator transition at $V_g \approx 2\ V$. For $V_g > 2\ V$, the conductance increases as temperature decreases until $T \approx 30\ K$, below which the conductance starts to fall quickly as a function of the temperature (shaded area). One possible reason for this sudden fallen is the freezing of the contacts to the 2D bulk, which in principle could be addressed by some kind of four-terminal measurements on the 2D bulk (see Chap. 5 for four terminal measurements).

For $T > 100\ K$ and $V_g < 2\ V$, the conductance increases almost linearly with increasing temperature, which contradicts to normal insulating behavior. However, below 100 K the conductance can be fit into thermally activated behavior ($G = G_0 exp(-\Delta/k_B T)$), as in Fig. 4.5d for $V_g = 0$. The best fitting yields a gap of $\Delta = 5\ meV$.

In all the two-terminal conductance measurements on the 2D bulk above, the geometry is not proper for measuring the conductivity. In fact, to obtain the aspect ratio (l/w), we performed a simulation of the current density distribution for geometry approaching the actual device and got an aspect ratio of 2.2. Of course, this represents a crude estimation that does not take into account a non-ideal geometry and any in-plane anisotropy of the conductivity. To avoid such uncertainty and complexity, we also fabricated a new type of device (MW3) with a series of alternating pincer-shape contacts overlapping a straight edge of a monolayer WTe_2. The inset of Fig. 4.6 shows the schematic of one set of the pincer shape contacts, in which the pink rectangle represents the monolayer WTe_2, and the two outer

contacts has a well-defined aspect ratio, thus can be used to probe the bulk conductivity if the center contact is grounded. The black and blue curves in Fig. 4.6 are the conductance between the two outer contacts with and without grounding the center contact respectively.

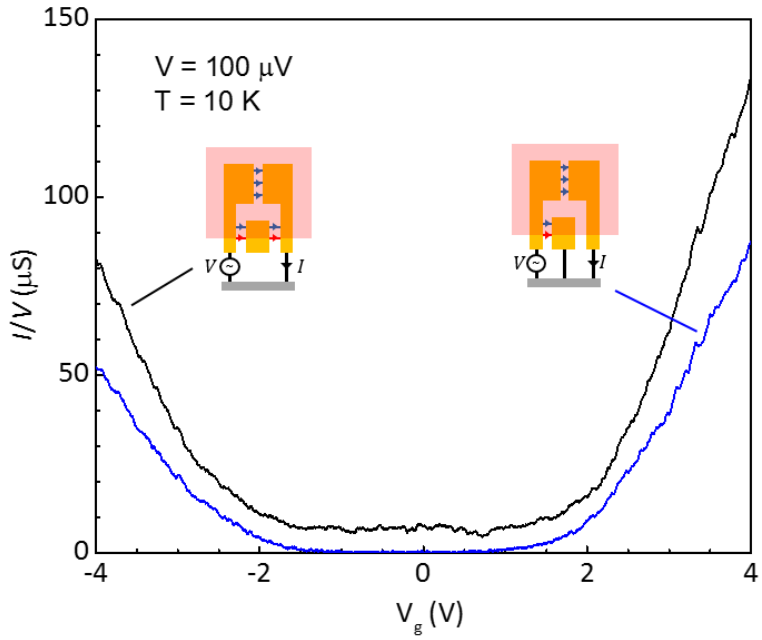

Figure 4.6: Two-terminal conductance as a function of V_g on the pincer shape device (MW3) at T = 10 K. The black and blue curves are measured with the center contact floated and grounded respectively. The insets show the two measurement configurations, in which the pink rectangles represent the WTe_2 flake.

4.2.3 Magnetic field dependence

So far we have shown that monolayer WTe_2 bulk becomes insulating below about 100 K, while the edge remains conducting down to 1.6 K. Then the next question is what kind of edge state is it? Is it consistent with the quantum spin Hall edge? To investigate it, we studied the in- and out-of-plane magnetic field dependence of the edge conductance, which is key for proving the helical nature of the edge.

Figure 4.7 shows the in-plane magnetic field dependence of the edge conductance at $V_g = 0$ and low temperatures, in which the conduction through the 2D bulk is negligible. For moderate $B_{||}$ and T the behavior approximates the activated function $G_{edge} = G_0 exp(-\alpha B_{||}/T)$ with $G_0 = 17\ \mu S$, and $\alpha = 5$, plotted as the red dashed lines. The $B_\perp$ sweeps are similar but weaker than $B_{||}$, as shown in the lower inset. Understanding the behavior under $B_\perp$ is more complicated due to the orbital effect.

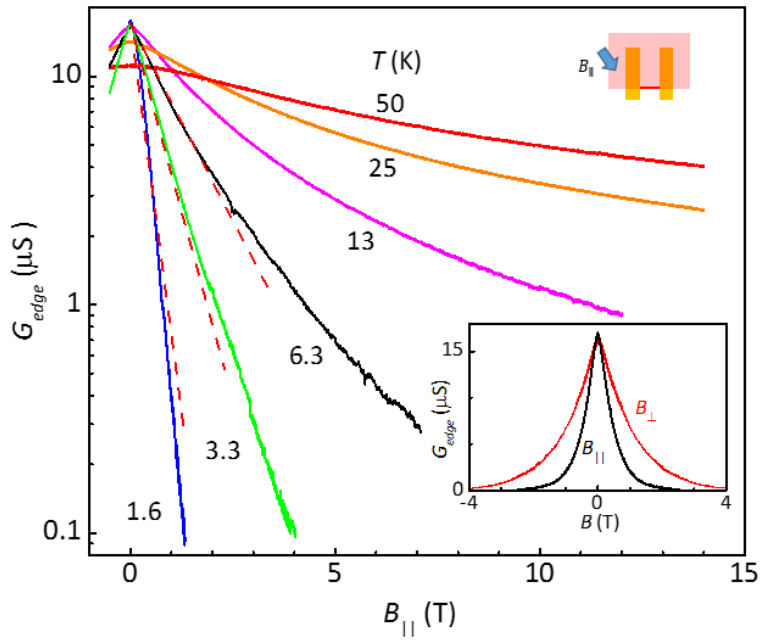

Figure 4.7: Edge conductance as a function of $B_{||}$ at $V_g = 0$ for various temperatures. Dashed lines plot $G_0 exp(-\alpha B_{||}/T)$ with $G_0 = 17\ \mu S$, $\alpha = 5$. Upper inset: orientation of $B_{||}$ relative to the edge. Lower inset: Comparing in- and out-of-plane magnetic fields at 1.6 K ($V_g = 0$).

Figure 4.7 also suggests a way of suppressing the edge state by applying a large magnetic field. In Fig. 4.8a we are showing the linear conductance between two adjacent contacts at an in-plane field of 0 T (black trace) and 14 T (blue trace) respectively ($T = 10$ K); the red

trace plots the difference between the two. Surprisingly, the difference is almost independent of the gate voltage in the accessible range, meaning the conductance suppression is due to the edge, while the bulk is immune to the magnetic field. Indeed, Fig. 4.8b shows conductance of the 2D bulk measurement under the perpendicular magnetic field of 0 T (blue) and 10 T (green), no appreciable magnetoresistance is found.

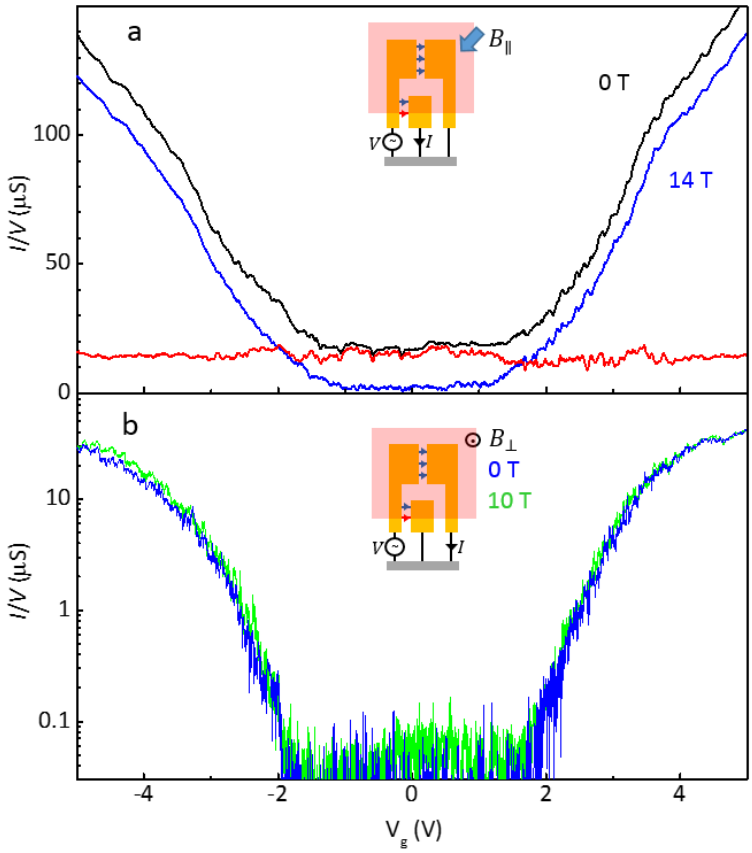

Figure 4.8: a, Gate dependence of the two terminal conductance between two adjacent contacts at an in plane magnetic field of 0 T (black) and 14 T (blue). b, Gate dependence of the conductance of the 2D bulk at an out of plane field of 0 T (blue) and 10 T (green) respectively. Insets are the measurement configurations, both figures are measured at 10 K on the pincer shaped device.

4.2.4 Mesoscopic fluctuations and length dependence

In previous sections, we have shown that upon decreasing temperature a conductance plateau would develop in gate sweeps for monolayer WTe_2 devices. However, a close look at these gate sweeps would reveal some mesoscopic fluctuations, the level of which varies for different devices and edges.

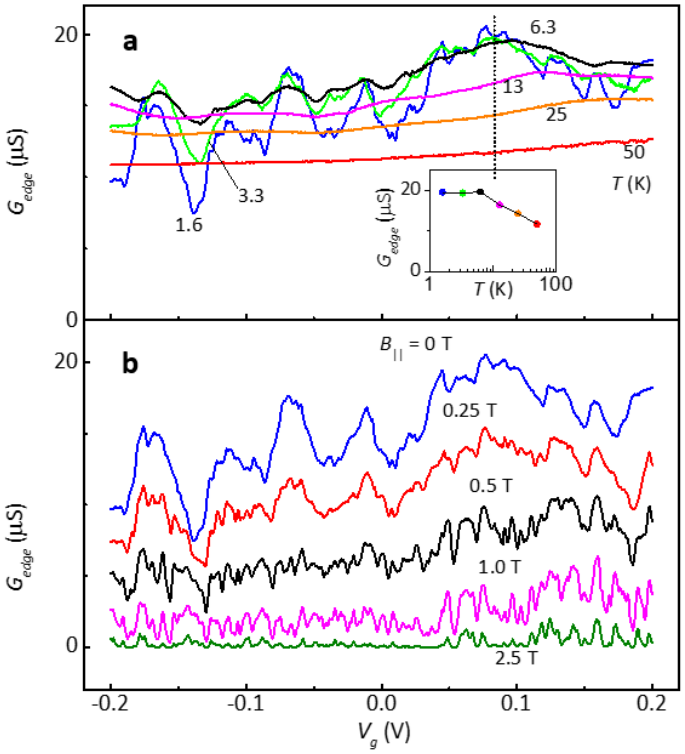

Figure 4.9: a, Temperature dependence of the edge conductance G_{edge} as a function of V_g at zero magnetic field. b, Effect of in-plane magnetic field $B_{||}$ at 1.6 K.

Figure 4.9 shows typical fine gate sweeps of G_{edge} between two adjacent contacts for different temperatures and magnetic fields. Cooling from 50 K to 10 K at 0 T, G_{edge} increases, but below about 10 K G_{edge} decreases again for general V_g, and mesoscopic fluctuations

start to prevail. For particular gate voltages, $V_g = 0.08\ V$ for example, the temperature dependence of G_{edge} is shown in the inset, the conductance increases first and then saturates to certain value (here $\sim 20\ \mu S$) below 10 K. Figure 4.9b shows the effect of $B_{||}$.

In Fig. 4.10 we compile measurements for 19 adjacent-contact pairs in four different monolayer devices, color coded by device, at zero magnetic field. The edge length L, which ranges from 0.16 to 5.5 μm, was estimated from atomic force microscope (AFM) images. For each edge we show the linear conductance, averaged over a window of V_g in which the bulk contribution is negligible, at 10 K (solid circles) and 1.6 K (open circles). At both temperatures the average conductance tends to decrease with L, but the trend is rather weak compared with the large, seemingly random variations. The edges with the weakest T dependence in this range also have the highest conductance, $\sim 20\ \mu S$.

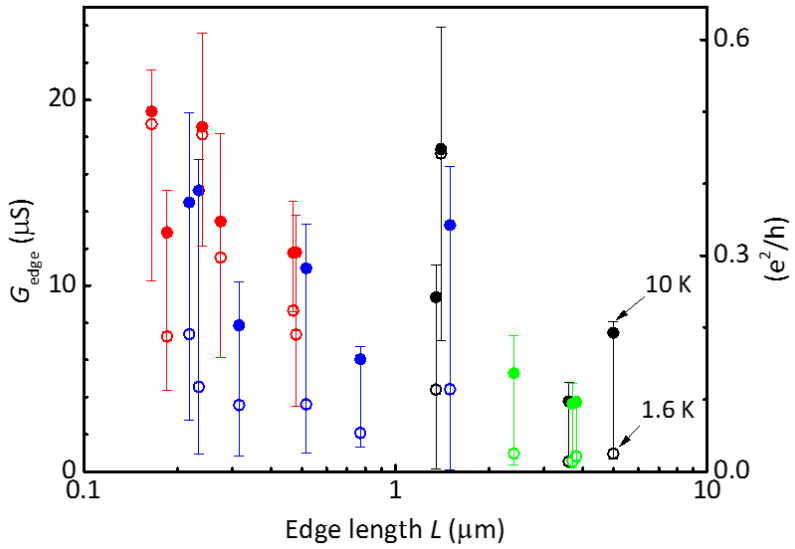

Figure 4.10: Gate-averaged linear response edge conductance for 19 adjacent-contact pairs at 10 K (solid circles) and 1.6 K (open circles), different colors correspond to different samples. The error bars represents the full range of fluctuations.

4.2.5 Zero bias anomaly and gap opening in the edge

In Fig. 4.2, a small dc bias of 3 mV was applied on top of the 100 μV ac excitation to suppress the mesoscopic fluctuations. To justify it, we are going to introduce the zero bias anomaly (ZBA) first. Figure 4.11a,b show the linear current and differential conductance as a function of the applied dc bias at $B_{||} = 0\ T$ (black) and $B_{||} = 10\ T$ (blue), both measurements are performed on a long edge of 1.5 μm at $T = 1.6\ K$, $V_g = 0$. At $B_{||} = 0\ T$, there is a sharp dip in dI/dV at $V = 0$, which we call ZBA. This dip always grows as T decreases, as illustrated in Fig. 4.11c. The mesoscopic fluctuations that grow on cooling are linked to the ZBA. A possible explanation of ZBA is that the edge state of monolayer WTe_2 behaves as a Luttinger Liquid (LL) due to some kind of interaction [80–83]. As a result, the temperature dependence can be scaled into a single curve as in Fig. 4.11d with fitting parameter $\alpha = 1.7$. Further investigations are necessary for better understanding of the zero bias anomaly and the underline mechanism.

The 1.5 μm edge is a typical example of the edges we studied, although the strength of the ZBA varies between different edges and different gate voltages. At the same time, it is worth mentioning that for some edges the ZBA is rather weak even at the base temperature (1.6 K). We call them "good" edges. In linear response these they always show much weaker fluctuations in the gate sweeps and the temperature dependence is also much weaker below 100 K. The linear response measurements in previous sections are performed on these "good" edges. Nevertheless, to capture the generic behavior of all devices factoring out the ZBA, we applied a small bias of 3 mV in Fig. 4.2, and we see a flatter edge conduction plateau similar to the "good" edges.

For $B_{||} = 10\ T$, as in Fig. 4.11b, a sharp threshold appears for the differential conductance. There are two possible origins for this threshold or solid gap, the bulk gap and the Zeeman gap of the edge. To figure out which one is dominant we performed the same experiment on the pincer shape device (MW3) at various magnetic fields.

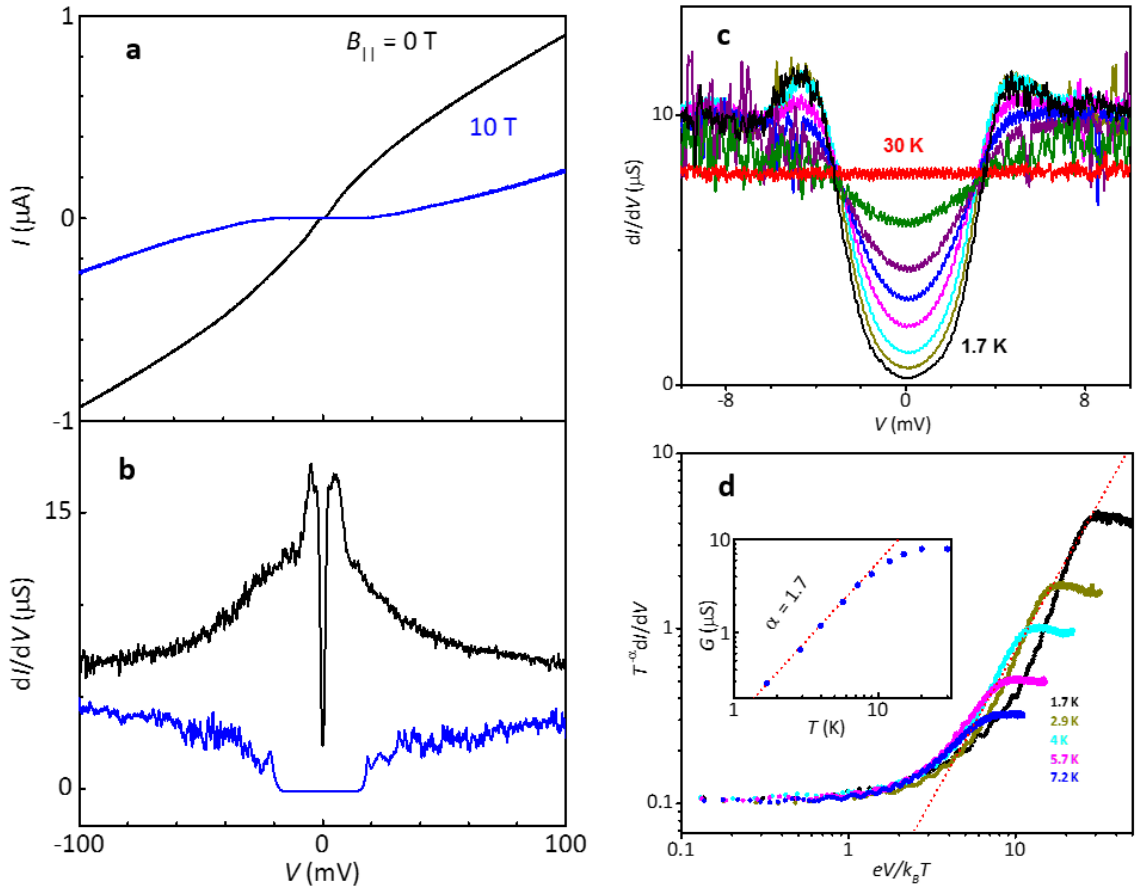

Figure 4.11: Nonlinear behavior of a 1.5 μm edge. a, I-V cures at $B_{||} = 0$ (black) and 10 T (blue) at $V_g = 0,\ T = 1.6\ K$. b, Corresponding differential conductance. A zero bias anomaly (ZBA) is seen at $B_{||} = 0$, while a sharp threshold appears for $B_{||} = 10\ T$. c, Differential conductance as a function of the dc bias for various temperatures from 30 K to 1.6 K. $B = 0, V_g = -0.68\ V$. d, Scaled differential conductance. Inset is the linear conductance as a function of the temperature in log-log scale, the best fitting yields $\alpha = 1.7$.

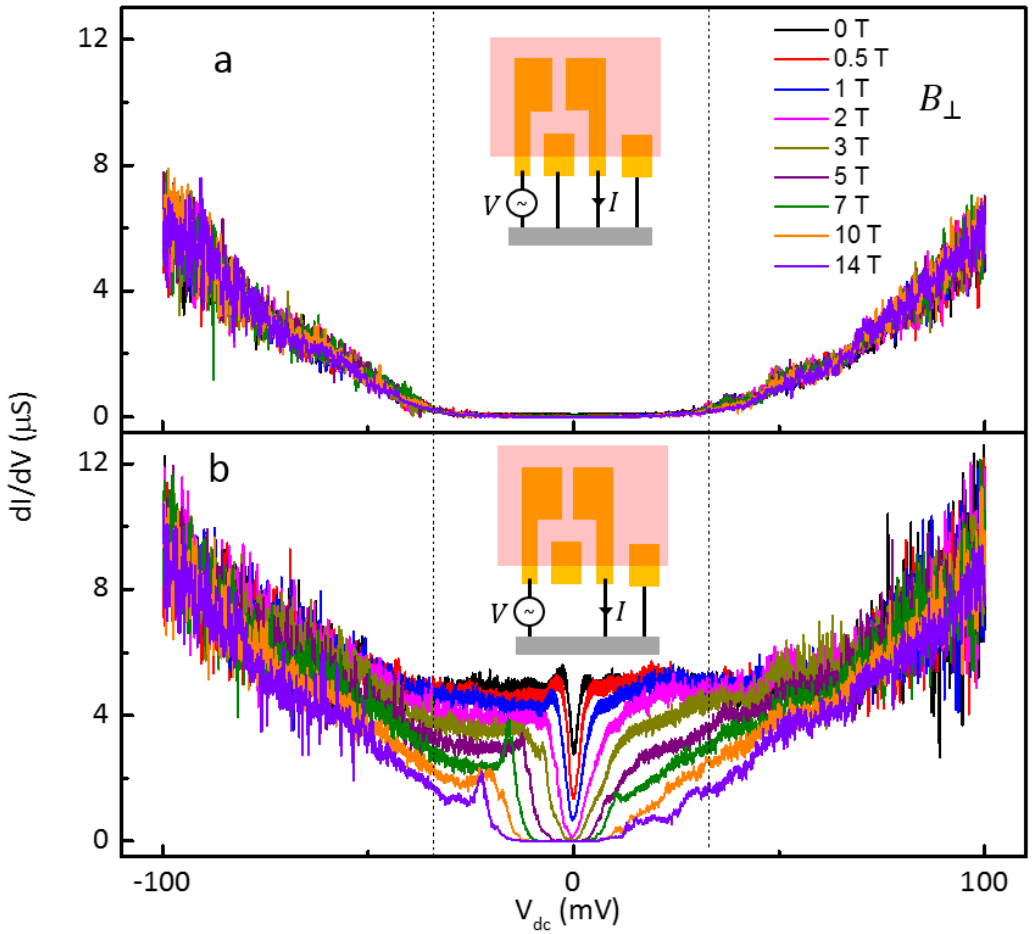

Figure 4.12: dI/dV as a function of V_{dc} of the pincer shape device (MW3) with (a) and without (b) the edge grounded for various $B_\perp$. The insets shows the corresponding configurations of the measurements.

Figure 4.12 shows the differential conductance as a function of the dc bias for the corresponding configuration in the inset. In the first case, we grounded the center contact and measured the differential conductance between the two outer contacts for perpendicular magnetic field from 0 to 14 T. As in the linear response, the dI/dV of the 2D bulk is also immune to $B_\perp$, and equals o for $V_{dc} < 30\ mV$. In the second case, the centered contact is floated. For $B_\perp = 0$, there is a strong ZBA as usual. As $B_\perp$ increases, the differential

conductance minimum decreases and finally becomes completely insulating, forming an insulating gap. The gap increases linearly with the magnetic field, consistent with the linear response ($G \sim G_0 exp(-\alpha B/T)$), but is always smaller than the bulk gap for $B_\perp \leq 14\ T$, as the indicated by the dashed lines.

To summarize, we found the zero bias anomaly seems to be generic to the edge state of monolayer WTe_2, while the strength varies for different edges and gate voltages. When a magnetic field is applied, both ZBA and dI/dV would be suppressed due to the opening of band gap in the edge state. The edge gap increases linearly with the external magnetic field, but is smaller than the bulk gap in the accessible range ($B \leq 14\ T$).

4.2.6 Discussions on the non-ideal helical edge

Now we will discuss the compatibility of the edge state we discovered with the scenario of a helical edge mode, in comparison with a trivial edge mode or carrier accumulation due to band bending. First, the monolayer edge conductance is roughly independent of V_g, and therefore chemical potential, over the entire accessible range (Fig. 4.8a). This is consistent with a single gapless mode, and not with carrier accumulation due to band bending or a trivial edge mode. Second, we see no edge conduction in bilayers. This can be explained by the fact that TR symmetry does not prohibit backscattering at the bilayer edge if the electron changes layer (the pair of coupled edges is not helical), whereas band-bending effects should be similar to those in a monolayer. Third, the conductance is dramatically suppressed by $B_\parallel$, consistent with the expectation that elastic backscattering is allowed once TR symmetry is broken.

On the other hand, we realized the edges we fabricated are far from being ideal in the following senses. (1) The conductance for a single ideal helical edge should saturate to the quantized value (e^2/h) as the separation of contacts and temperature decreases. In our experiment, even for the shortest edge (150 nm), the linear conductance never reaches the conductance quanta, and seems to keep decreasing as T decreases. (2) For $B = 0$, the helical edge is protected by TR symmetry, prohibiting any elastic backscattering. However, in our

devices, there are always mesoscopic fluctuations to some extent while sweeping the gate voltage. (3) For small B, the helical edge would open up a gap of $\Delta_B = g\mu_B B$, proportional to the external magnetic field. In previous sections, we do actually observe such gap in the magnetic field dependent linear and differential conductance measurements. However, in gate sweeps we never see a single sharp dip in certain gate range, instead there is always a lot of mesoscopic fluctuations. Possible explanations for these disagreements with ideal helical edges may include the non-transparent contact, short mean free path (shorter than 100 nm) and interaction effects. With all these ingredients, we propose the following simple picture, which captures most of the observed behavior while keeping the helical nature.

We suppose that there is indeed a single helical edge mode that follows the physical edge of the monolayer and effectively experiences a large but smooth disorder potential, for example due to static charges. As a result, the energy at which the left- and right-going branches are degenerate fluctuates up and down along the edge, passing through E_F at multiple points. This situation is sketched in Fig. 4.13. If some inter-branch scattering is possible in spite of the helical protection, it is likely to be strongest at these 'weak points' where no momentum transfer is required. At $B_{||} = 0$ in some edges the average linear conductance G_{edge} is not much less than e^2/h, and so the scattering must be weak, yet we see large, rapid mesoscopic fluctuations. If the origin of these fluctuations is quantum interference, then since no Feynman paths enclose magnetic flux in a one-dimensional wire we expect no corresponding fluctuations as a function of $B_\perp$, as is the case (see Fig. 4.7 inset). As T decreases, the scattering from the weak points strengthens at energies near E_F due to interaction effects, producing the ZBA. Edges longer than a few hundred nanometers are not phase-coherent and so have smaller conductance due to classical addition of resistance. Also, as T rises the coherence length will decrease, consistent with the fact that G_{edge} tends to decrease with T when the ZBA is small (see Fig. 4.9a, above ~6 K). A magnetic field opens a gap Δ_B in the helical modes, as sketched in the lower part of Fig. 4.13. Electrons at E_F now encounter this gap at the weak points, which they can pass by activation, thus introducing the factor $exp(-\Delta_B/k_BT)$ in the conductance.

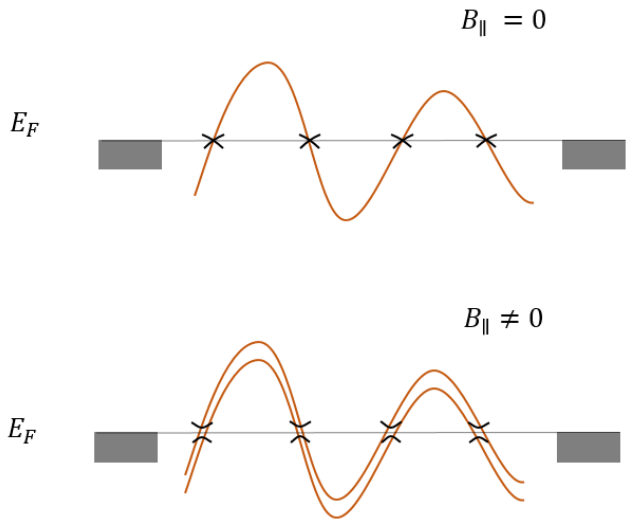

Figure 4.13: Schematic of combined effect of smooth static disorder and a magnetic field-induced gap along the edge.

4.3 Direct imaging of the edge state

Scanning microwave impedance microscopy (sMIM) is a new mode of imaging using AFM microscopy. It's a powerful tool for probing local electromagnetic response (electrical conductivity and permittivity) of nano-scale materials with spatial resolution of sub 100 nm. The sample is very easy to prepare, and unlike other conventional/non-conventional electrical probes, this new technique is nondestructive, and can be utilized to probe a wide variety of materials, from insulators, semiconductors to metals. It can also provide spatial information of trivial/topological edge states [84–86], magnetic/ferroelectric domains and domain walls [87–89].

In the sMIM system we use, the optimized electronics couple a 1 GHz microwave into a shielded tip of around 50 nm or less, which generates a strong electromagnetic (EM) field locally. After interacting with the sample underneath, the EM field is reflected and detected by the electronics. There are two output channels, the real part MIM-Re and the imaginary part MIM-Im, both of which can be viewed as images in the AFM software. Figure 4.14a shows the schematics of the sMIM. The impedance at the end of the tip can be simulated as a resistor (R) in parallel with a capacitor (C), or a load of Z, where $Z^{-1} = G_R + jG_C$. G_R is the conductance of the resistor ($G_R = 1/R$), while G_C is that of the capacitor ($G_C = \omega C$). From transmission line theory, the reflectance of a microwave in a lossless line is

$$\begin{aligned}\Gamma &= \frac{Z - Z_0}{Z + Z_0} = \frac{1 - Z_0/Z}{1 + Z_0/Z} = \frac{1 - Z_0(G_R + jG_C)}{1 + Z_0(G_R + jG_C)} \\ &= \frac{(1 - Z_0G_R - jZ_0G_C)(1 + Z_0G_R - jZ_0G_C)}{(1 + Z_0G_R)^2 + (Z_0G_C)^2} \\ &= \frac{1 - Z_0^2(G_R^2 + G_C^2)}{(1 + Z_0G_R)^2 + (Z_0G_C)^2} - j\frac{2Z_0G_C}{(1 + Z_0G_R)^2 + (Z_0G_C)^2}. \end{aligned} \tag{4.1}$$

Here Z_0 is the characteristic impedance. The real and imaginary parts of the reflectance as a function of the conductivity are simulated in Fig. 4.14b for a quantum well system. Both G (or σ_{xx}) and C are local values that varies spatially. Through scanning the entire sample, we could map the spatial distribution of the electromagnetic responses.

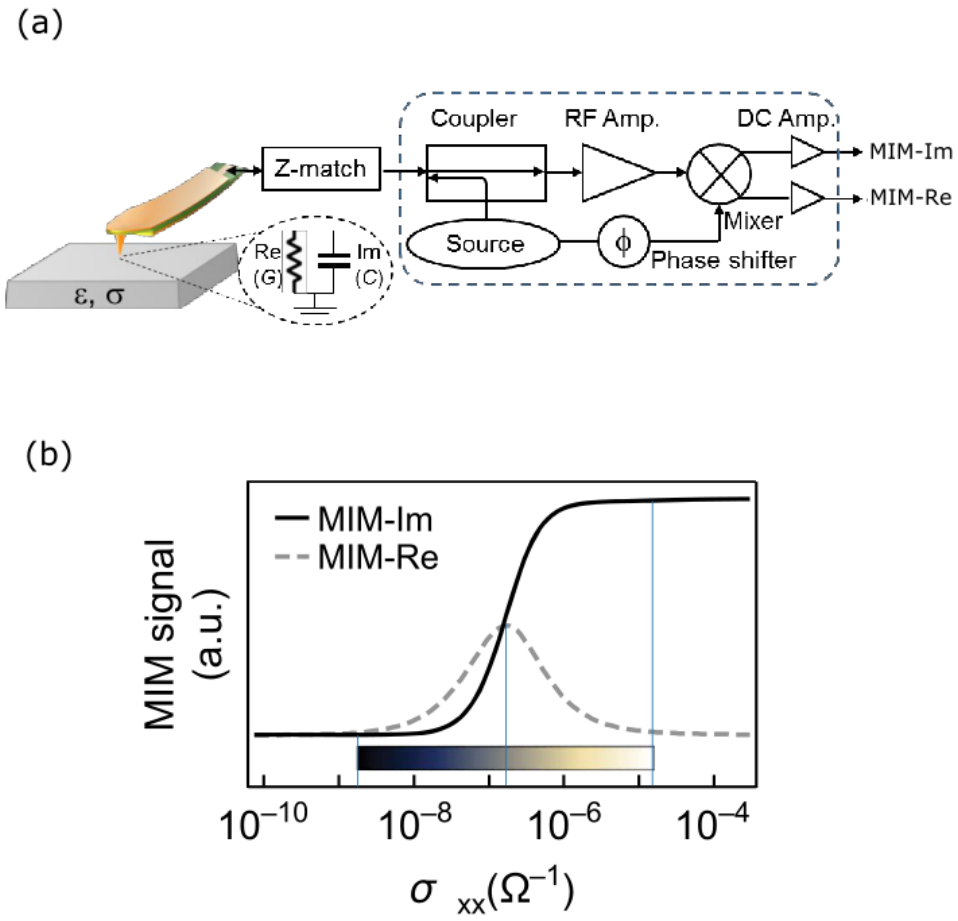

Figure 4.14: Schematics of scanning microwave impedance microscopy. b, MIM response as a function of the sheet conductance of a quantum well. (Figures adapted from Ref. [88] and Ref. [84]).

Figure 4.15 shows the optical and AFM image of a WTe_2 flake, which is partially covered by a thin layer of hBN to protected it from degradation. Based on the AFM image, most of the WTe_2 region is monolayer, the lower right corner, however, is a hybrid of bilayer and thicker layer ($\geq 3\ L$). The sample was cooled down to the base temperature (300 mK) before the scanning microwave impedance measurements. Figure 4.16 shows the imaginary part of the reflectance measured at $B = 0$ and $B = 12\ T$ (out-of-plane) on the same scale, performed

in the contact mode.

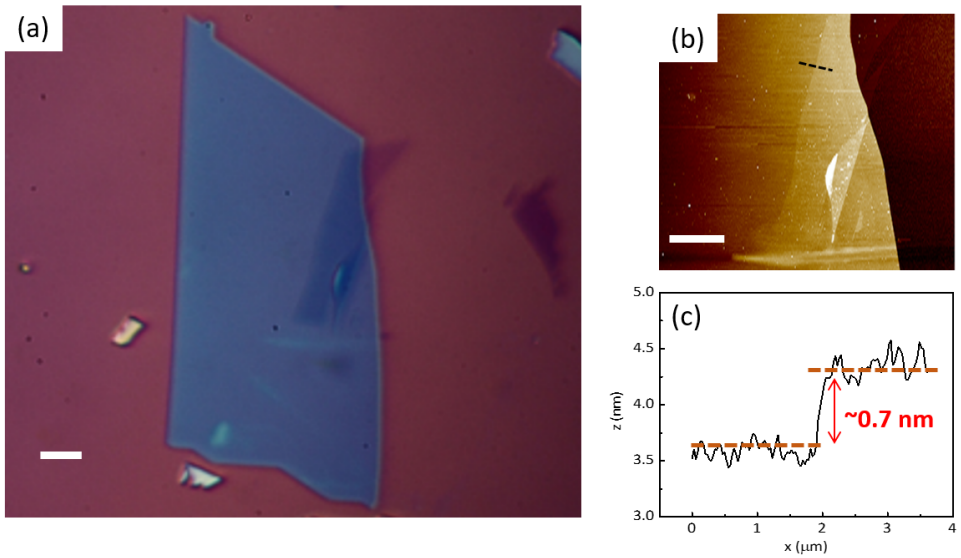

Figure 4.15: a, Optical image of WTe_2 covered by hBN. Scale bar is 5 μm. b, AFM image of the hBN/WTe_2 heterostructure in a. Monolayer, bilayer and thick layer can be identified on the same piece. Scale bar is 5 μm. c, Line trace along the dashed line in b, the monolayer thickness is identified to be ∼0.7 nm.

There are a lot of interesting features in the sMIM. (1) Only the monolayer underneath hBN has edge conduction, which can be suppressed by the magnetic field as expected. The uncovered part degraded and did not show any conduction, while the interface of the covered and uncovered region behaves as a new conductive edge. (2) Bilayer WTe_2 under hBN does not show any edge or bulk conduction. The bulk of the thicker layer conducts and cannot be turned off by the magnetic field. Both the bilayer and thicker layer signals are consistent with transport measurements. (3) In addition to the physical edges of the monolayer under the hBN, there are also internal lines of similar magnitude, not only in this particular sample but in all samples we've measured. These internal lines can also be suppressed by magnetic field, making them almost indistinguishable with the real physical edges. We also performed

polarized Raman spectroscopy (see Appx. B for details) on the same sample and found no difference in the polarization dependence for the entire sample. On the other hand, these internal lines do not show up in the topology. We thus conclude it's not due to domain walls or physical cracks, it's probably due to some built-in strain which is introduced while we try to cover the WTe_2 with hBN. Nevertheless, further investigations are required for better understanding of these internal lines and one needs to be very careful while looking for perfect quantization in transport measurement.

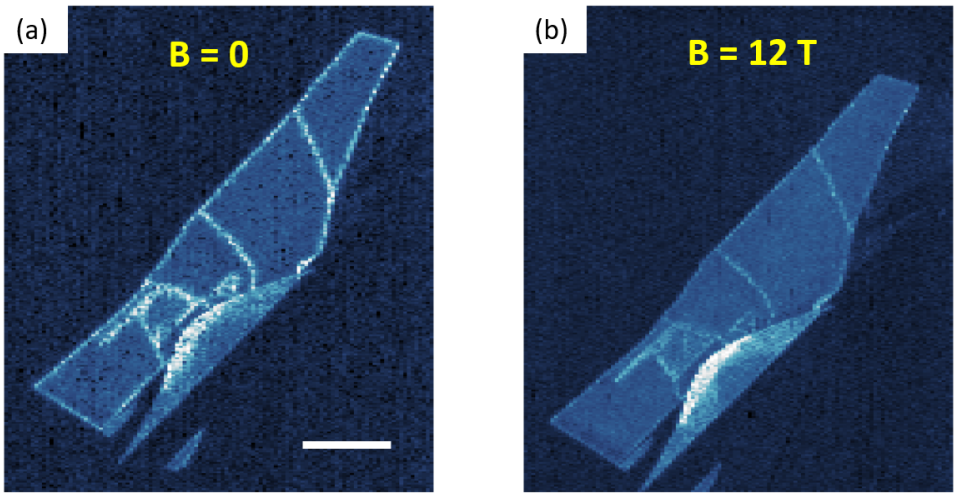

Figure 4.16: a, b, Imaginary part of the MIM signal on hBN/WTe_2 heterostructure at $B = 0$ (a) and $B = 12\ T$ (out-of-plane) (b) respectively. $T = 300\ mK$.

4.4 Conclusions and future outlook

In this chapter, we investigated the intrinsic transport properties of monolayer WTe_2 in details near charge neutrality from 300 K to 1.6 K. In contrast to the DFT calculations, our experiment, however, reveals that the interior of monolayer WTe_2 is insulating below about 100 K. From the temperature dependence of the 2D bulk measurement, a gap of 5 meV at $V_g = 0$ is obtained. This small energy gap could be a single particle band gap which is very sensitive to the strain or lattice constant used in the DFT calculations. It is also realized that certain arrangement of electron and hole puddles in a semimetal with a small overlap of conduction and valence bands could also lead to an insulating behavior [90]. More intriguingly, if the insulating behavior is a result of strong electron-electron correlation or electron-hole coupling, more exotic properties are expected in such system. Nevertheless, the nature of this insulating behavior is still not understood. Despite the insulating interior, there are conducting channels along the physical edges. These edge conduction shows expected temperature and magnetic field dependence as helical edges.

In contrast to the ideal helical edge, the conductance for a single edge never reaches the conductance quanta, and always shows mesoscopic fluctuations as a function of gate voltage at low temperatures, indicating appreciable backscattering. The perfect quantization is clearly a key signature of the quantum spin Hall effect and should be resolved before a conclusive claim of the nature of the edge conduction. In pursuing perfect quantization for an ideal helical edge, one needs to exclude the effect of the contact resistance while at the same time try even shorter channels.

If monolayer WTe_2 is indeed a quantum spin Hall insulator, it will offer a lot of new opportunities in the realms of both topological and low-dimensional physics. As a monolayer it can also be combined with other layered materials, such as layered magnets, semiconductors, and superconductors for the realization of spin manipulation or to create Majorana zero modes [21, 91].

Chapter 5

ELECTRIC FIELD INDUCED SUPERCONDUCTIVITY IN MONOLAYER WTE_2

5.1 Introduction: crystalline 2D superconductor

2D superconductors have been investigated for about 80 years since the observation of superconductivity in Pb and Sn thin films [92]. A lot of 2D systems including disordered metallic thin films, interfaces of complex oxide heterostructures [93, 94], and highly crystalline atomic layers grown by molecular beam epitaxy (MBE) have been reported to superconduct at cryogenic temperatures. Recently, mechanical exfoliation, together with the technique of ionic liquid gating and the ability of applying high pressure, have been utilized in the field of 2D superconductors, therefore spurred tremendous interests in the highly crystalline 2D superconductors. These highly crystalline 2D superconductors provide new opportunities for studying new quantum phenomena, such as the quantum metallic ground state, as well as providing clues in searching for high-temperature superconductors [95].

In Chap. 3, we talked about pressure driven superconductivity in bulk WTe_2. Without any pressure or Te deficiency, bulk and few layer WTe_2 show no signature of superconductivity above 30 mK [35, 69, 96]. Monolayer WTe_2, however, exhibits very different transport properties with its bulk and few layer counterparts at low doping levels, as demonstrated in the last chapter. Figure 5.1a shows the two-terminal transfer characteristic for monolayer device MW1 at various temperatures, from 300 K to 1.6 K. When increasing the gate voltage above $\sim$1.7 V, monolayer WTe_2 undergoes an insulator to metal transition, i.e. the conductance increases as T decreases. Actually, when the temperature is low enough, for gate voltage larger than 1.7 V, the conductance/resistance is weakly dependent on T. Shown in Fig. 5.1b is the four-wire resistance normalized by the normal resistance as a function of T on

the same device while the carrier imbalance (sometimes called carrier density for convenience) is set to $1.8 \times 10^{13}\ cm^{-2}$ with both top and bottom gates ($\Delta(n-p) = C_{tg}\Delta V_{tg} + C_{bg}\Delta V_{bg}$). The black and red curves are in the linear and log scale respectively. For $T > 1\ K$, the four-wire resistance is almost independent of T.

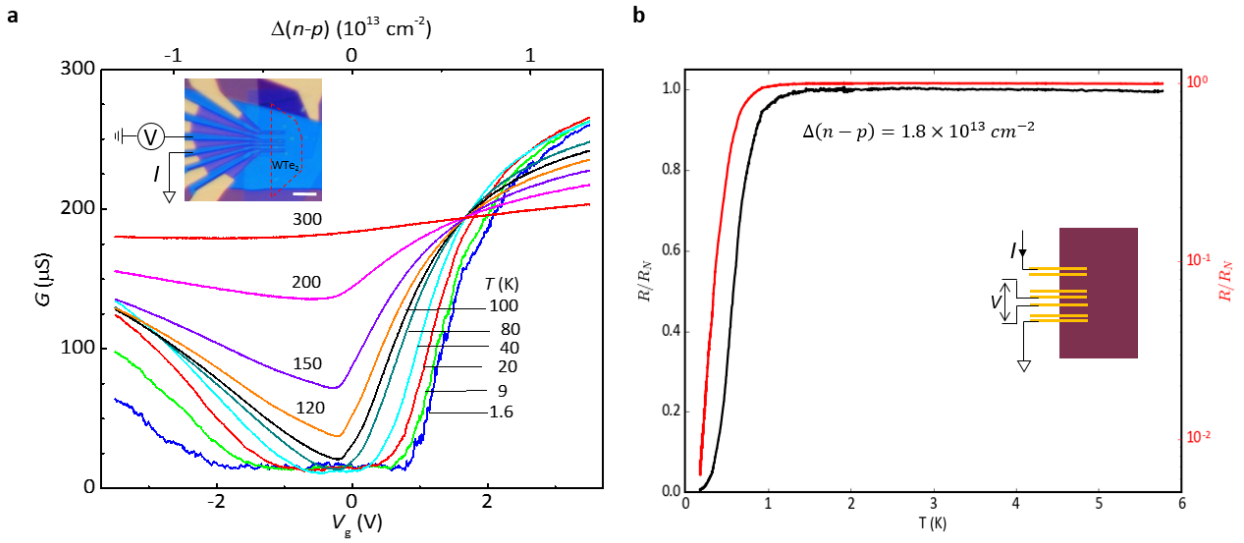

Figure 5.1: a, Two-terminal conductance as a function of gate voltage for various temperatures from 300 K to 1.6 K for MW1. The inset is the optical image of the device together with the electric setup for the measurement, scale bar is 5 μm. b, Temperature dependence of the normalized four-wire resistance on the same device. Here, T varies from 5.8 K to 20 mK, and the carrier imbalance is fixed at $1.8 \times 10^{13}\ cm^{-2}$, both the black and red curves are plots for the normalized resistance, but are in the linear and log scale respectively. The inset shows the electric setup for the four-wire measurement.

However, when the temperature is below about 700 mK, the resistance suddenly drops by more than two orders of magnitudes before reaches zero resistance. In the other way, monolayer WTe_2 becomes a superconductor at around 700 mK for a carrier imbalance of $1.8 \times 10^{13}\ cm^{-2}$.

5.2 Gate tunable superconductivity in monolayer WTe_2

One of the key benefits of 2D superconductors is that one could modify their carrier densities substantially by applying an electrical gate. One of such example is the observation of superconducting dome in an ionic liquid gated monolayer MoS_2 [97–99]. However, the disadvantages of using ionic liquid gate are also quite obvious, the long relaxation time and poor reproducibility over different cooling cycles. In monolayer WTe_2, the carrier imbalance ($\Delta(n-p) = 1.8 \times 10^{13}\ cm^{-2}$) as we discussed in the last section is smaller by one order of magnitude compared to that of MoS_2, implying that one could tune the superconductivity simply with an electrostatic gate.

5.2.1 Carrier density dependent critical temperature

Figure 5.2 shows the four-wire resistance as a function of T for various carrier densities, measured in the same configuration as Fig. 5.1b. The carrier densities are estimated using capacitor model ($\epsilon_{BN} = 4$), and are listed in the right bottom inset. When the carrier imbalance is above $6.1 \times 10^{12}\ cm^{-2}$, the four-wire resistance continuously decreases to near zero as T decreases despite the appearance of an intermediate step (the origin of this intermediate step is still unknown). When the carrier imbalance is below $4.6 \times 10^{12}\ cm^{-2}$, it shows an insulating behavior, consistent with what we observed in the previous section.

If we define the temperature at which the resistance drops to half the normal value as the critical temperature ($R(T = T_c) = \frac{1}{2}R_N$), then the critical temperature (T_c) as a function of the carrier density can be plotted as the inset of Fig. 5.2b. Here, T_c can be substantially tuned from 700 mK at $2 \times 10^{13}\ cm^{-2}$ to below 200 mK at $5 \times 10^{12}\ cm^{-2}$. The main panel is the normalized resistance as a function of T for various carrier densities same as in Fig. 5.2a.

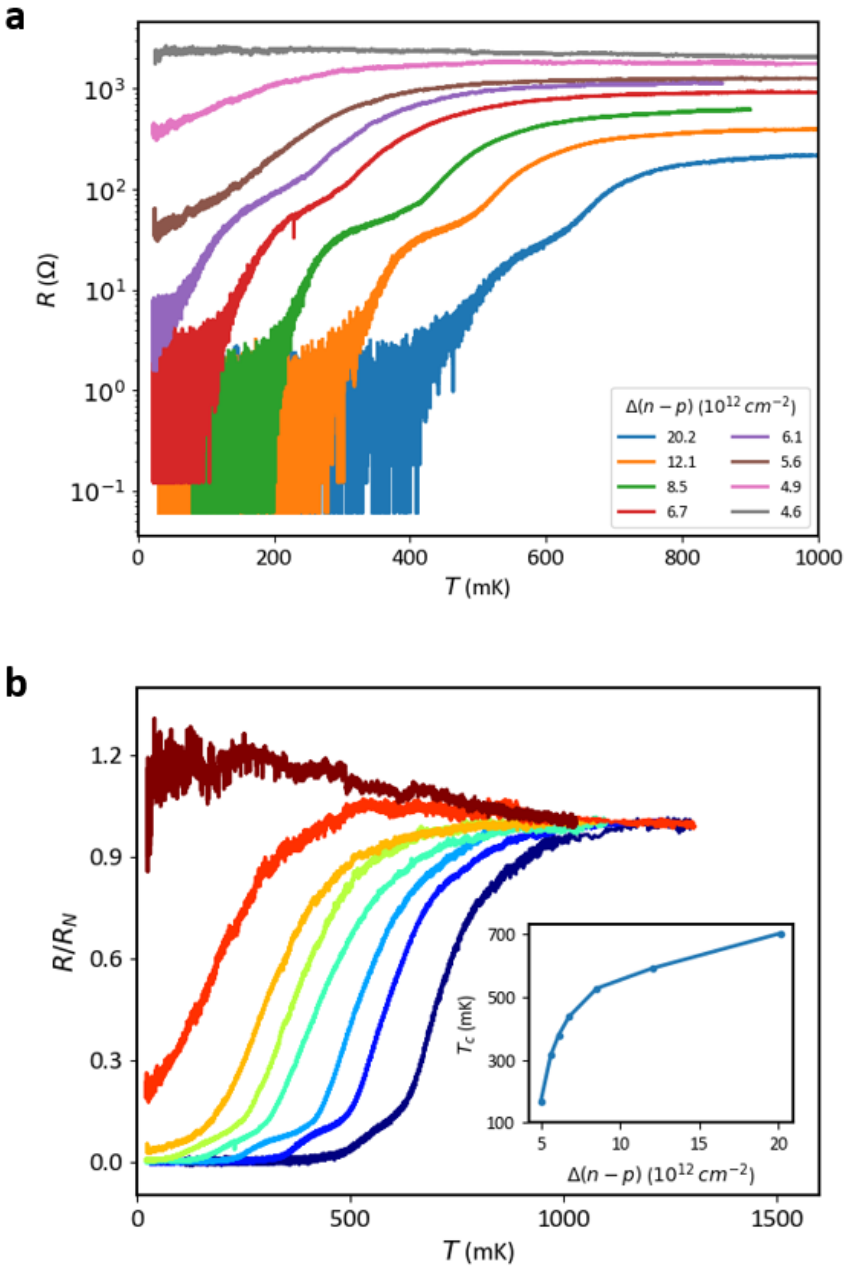

Figure 5.2: a, Temperature dependence of the four-wire resistance for various carrier densities. The bottom right inset shows the carrier densities estimated using the capacitor model. b, Normalized four-wire resistance as a function of temperature. The bottom right inset shows the change of critical temperature as a function of the carrier imbalance.

5.2.2 Gate tunable insulator to superconductor transition

Shown in Fig. 5.3 is a 2D map of the four-wire resistance as a function of the top and bottom gates measured at 20 mK. The resistance is plotted in the log scale. For small V_{tg} and V_{bg}, the resistance is larger than 1 $M\Omega$, implying WTe_2 is really insulating for $T = 25\ mK$ due to the zero bias anomaly as we discussed in the last chapter. However, when monolayer WTe_2 is electron doped with positive V_{tg} or V_{bg}, the four-wire resistance quickly drops to below 1 Ω, beyond the measurability of our system, suggesting it becomes a superconductor.

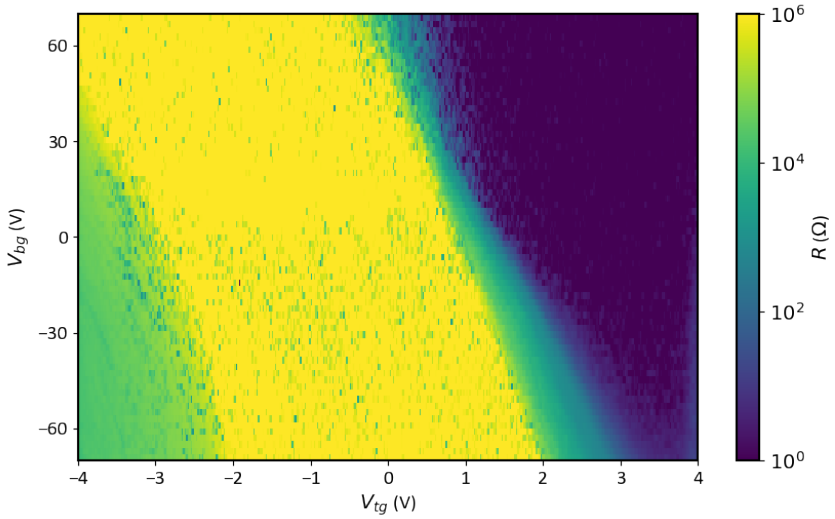

Figure 5.3: Color plot of the four-wire resistance as a function of the top and bottom gates. $T = 20\ mK$.

It's worth pointing out that due to the presence of metal contacts underneath the WTe_2 flake, V_{tg} and V_{bg} are expected to behave slightly differently from each other. One could actually make use of this slight difference to investigate the insulator to metal transition without contacts effect, i.e. always scanning V_{bg} while V_{tg} is set to a large positive value to ensure good electric contacts. Figure 5.4 shows the four-wire resistance as a function of V_{bg} at different temperatures, here $V_{tg} = 2.05\ V$. As one can see, $R - V_{bg}$ curves at different

temperatures cross each other at a critical gate voltage of $V_{bg,c} = -32.5\ V$, with a critical resistance of $R_c = 2\ k\Omega$. By tuning V_{bg} from below to above $V_{bg,c}$, monolayer WTe_2 transits from an insulator to a superconductor.

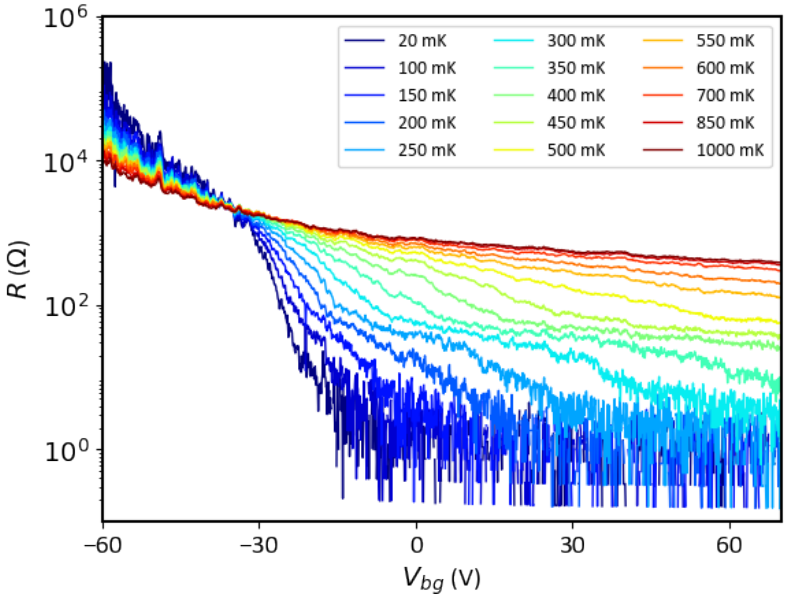

Figure 5.4: Four-wire resistance as a function of the bottom gate, different curves are measured at different temperatures as in the top right inset. The top gate is fixed at $V_{tg} = 2.05\ V$ for all temperatures.

To investigate this transition, we applied scaling analysis to the system as in previous works [100, 101]. In the analysis, the resistance can be described by following phenomenological function: $R(\delta, T) = R_c \cdot F(\delta\ T^{-1/\nu z})$, where $\delta = V_{bg} - V_{bg,c}$ is the deviation from the critical gate voltage in our case, F is an arbitrary function, ν is the correlation length exponent, and z is the dynamical critical exponent. Figure 5.5 shows the scaling of the resistance as a function of the scaling variable $|V_{bg} - V_{bg,c}|T^{-\alpha}$ for temperature from 100 mK to 300 mK near the critical point ($100\ \Omega < R < 8000\ \Omega$). The best fit yields an effective critical component of $\alpha = 1/\nu z = 0.6 \pm 0.2$ or $\nu z = 1.7 \pm 0.8$. Note here we discarded the data at

20 mK, which did not quite agree with the scaling behavior because of the bad calibration of the sample temperature near 20 mK.

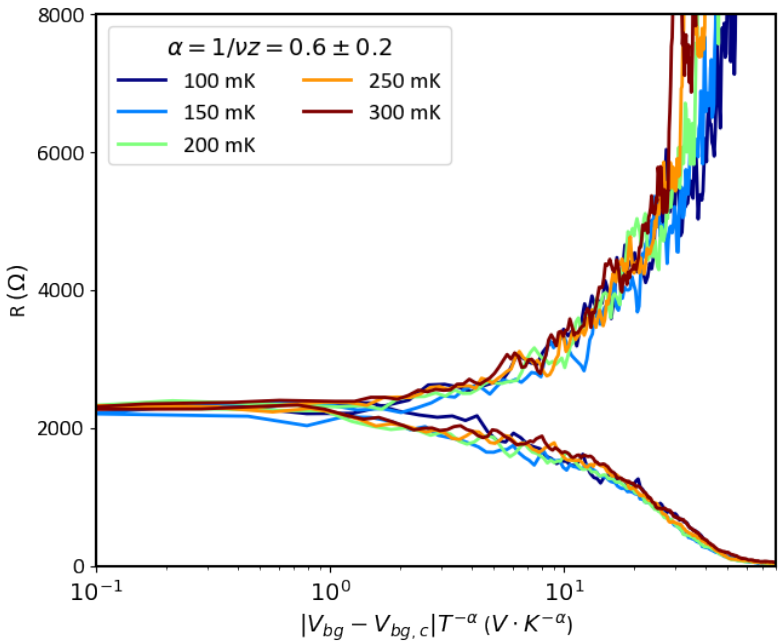

Figure 5.5: Resistance as a function of the scaling variable $|V_{bg} - V_{bg,c}|T^{-\alpha}$ for temperature from 100 mK to 300 mK. The best fitting yields an effective critical component of $\alpha = 1/\nu z = 0.6$.

5.3 Critical field and intermediate quantum metal

Except for increasing temperature, applying a magnetic field can also destroy the superconductivity in conventional superconductors by breaking Cooper pairs. Shown in Fig. 5.6a is the four-wire resistance of a monolayer WTe_2 as a function of the magnetic field, from below to above the critical temperature. The carrier imbalance is fixed at $1.5 \times 10^{13}\ cm^{-2}$, and the magnetic field is always pointed out of the sample plane as indicated in the lower left inset. At $T = 2\ K$, far above the critical temperature, the magnetoresistance is almost negligible, consistent with the 2D bulk measurement in the previous chapter. However, when the temperature is below the critical temperature, 20 mK for example, the resistance increases dramatically around $B_{c2} = 35\ mT$, and saturates to the normal resistance above 50 mT. In the other way, there is a superconductor to metal transition (SMT) driven by the magnetic field. It is also noticed that the crossing point varies with temperature, similar to the quantum Griffiths singularity of SMT observed in Ga thin films [102].

It is also very interesting to see the modulation of the upper critical field B_{c2} while varying carrier density. Figure 5.6b shows the 2D map of the four-wire resistance as a function of the magnetic field and the carrier imbalance. The dark region in the middle is where WTe_2 superconducts. When the carrier imbalance increases from $5 \times 10^{12}\ cm^{-2}$ to $9 \times 10^{12}\ cm^{-2}$, B_{c2} also increases monotonically. However, above $9 \times 10^{12}\ cm^{-2}$, B_{c2} is almost independent of the carrier imbalance.

More intriguingly, the upper critical field is found to be highly anisotropic for out-of- and in-plane magnetic field. Figure 5.7 shows the in-plane magnetic field dependence of the resistance measured at 20 mK with a fixed carrier density of $1.5 \times 10^{13}\ cm^{-2}$. The upper critical field in this case is around 3.5 T, 100 times larger than that for out-of-plane magnetic field. In fact, it is also larger than the Pauli limit [103, 104] for an homogeneous superconductor, $B_p = 1.86\ T_c(0) \approx 1.3\ T$.

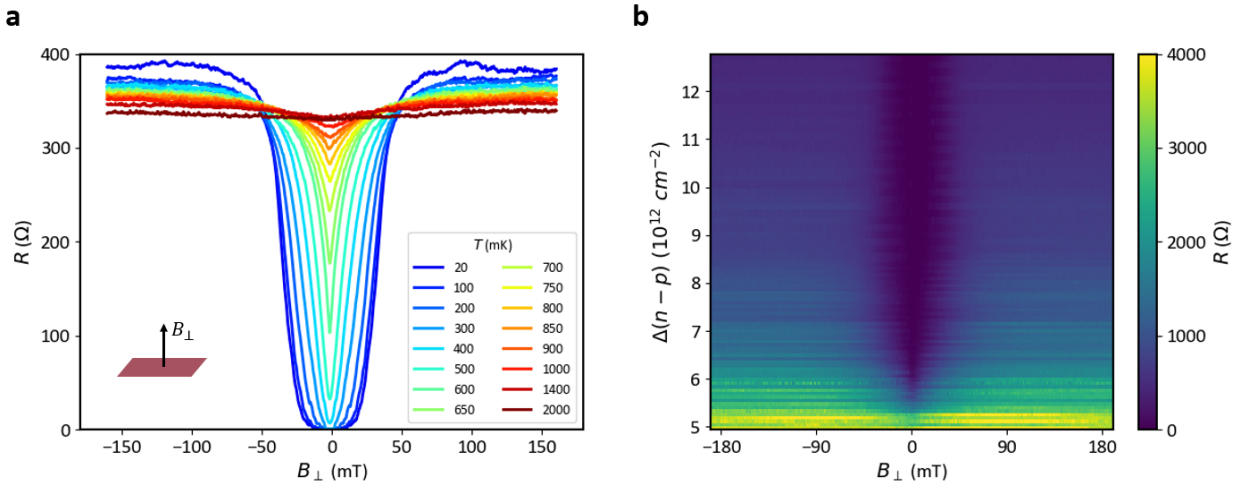

Figure 5.6: a, Four-wire resistance as a function of the $B_\perp$ for various temperatures. The lower left inset shows $B_\perp$ with respect to the sample plane. $\Delta(n-p) = 1.5 \times 10^{13}\ cm^{-2}$. b, 2D map of the resistance as a function of the magnetic field and carrier imbalance. $T = 50\ mK$.

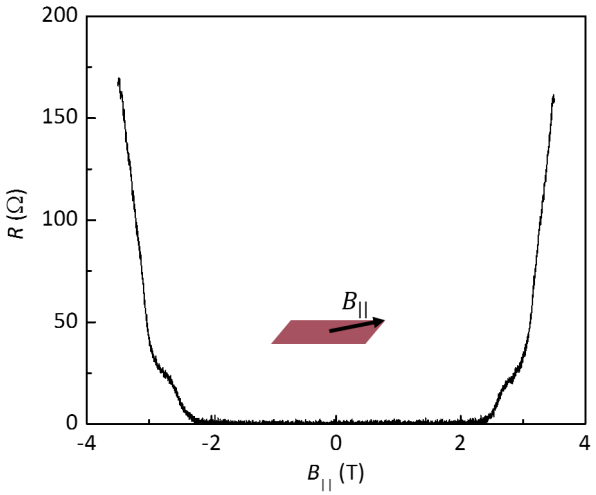

Figure 5.7: Four-wire resistance as a function of $B_\parallel$, measured at $T = 20\ mK$. Inset shows $B_\parallel$ with respect to the sample plane. $\Delta(n-p) = 1.5 \times 10^{13}\ cm^{-2}$.

In disordered superconducting thin films [105–107] and 2D crystalline $NbSe_2$ atomic layers [108], it is found that a substantial part of the phase diagram is occupied by an intermediate quantum metallic state, in which the resistance is non-vanishing but much lower than the normal resistance. In monolayer WTe_2, we were also able to observe such intermediate state for a small magnetic field. Figure 5.8 shows the temperature dependence of the four-wire resistance for various out-of-plane magnetic fields measured at a fixed carrier density of $\Delta(n-p) = 1.5 \times 10^{13}\ cm^{-2}$. For magnetic field larger than zero but smaller than B_{c2} (35 mT), as T decreases, instead of continuously decreasing to zero, the resistance decreases exponentially first, and below about 100 mK, the decreasing is much slower and the resistance almost saturated to a finite value dependent on the magnetic field. The nature of the quantum state is still under debate, and a lot of mechanisms have been proposed, including percolation of superconducting islands in disordered systems [109] and the Bose-metal model [108] where the Cooper pairing persists but the coherence is lost due to strong phase fluctuations caused by the magnetic field.

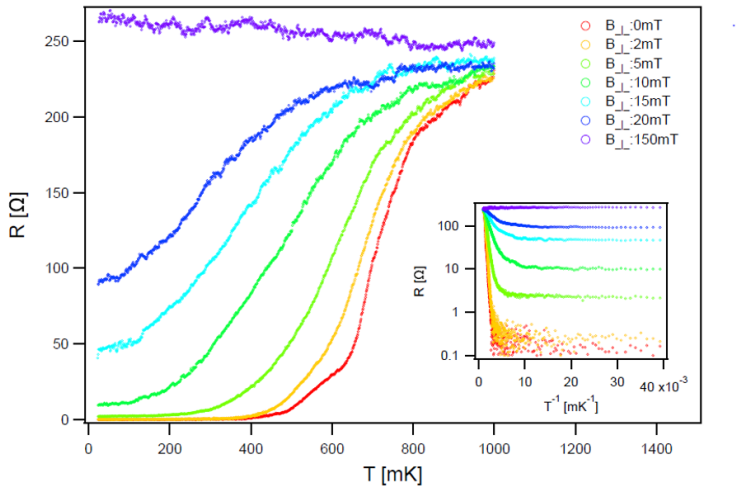

Figure 5.8: Temperature dependence of the four-wire resistance for various $B_\perp$. Inset is the corresponding Arrhenius plot. $\Delta(n-p) = 1.5 \times 10^{13}\ cm^{-2}$.

Further investigations are necessary for a full understanding the exact mechanism of the intermediate quantum metal state in monolayer WTe_2, and here I want to point out a few points. First, except for $B_\perp$ the intermediate quantum state is also observed under a small $B_\parallel$ or V_{bg}. In the case of $B_\parallel$, the phase coherence is unchanged, thus other factors have to be taken into account in the Bose-metal model. Secondly, the superconductivity presented in our monolayer WTe_2 devices seems to be very non-uniform, especially taking into account that the critical carrier density is relatively low and the unavoidable strain seems to have a large effect on the transport as we have already seen in the sMIM. In some devices with the same doping level, superconductivity is much weaker and there is a residual resistance even at the lowest temperature (20 mK). On the other hand, even in the same device, different regions seem to behave differently. It is thus reasonable to believe that instead of being an uniform crystalline 2D superconductor, upon cooling monolayer WTe_2, superconducting islands appears first and merges later. To have a better understanding the superconductivity in such system, spatial resolved mappings of the local resistivity at a series of temperatures are required.

5.4 Conclusions and Future outlook

In this chapter, we have shown that monolayer WTe_2 does become a superconductor in the interior with a large positive gate voltage when temperature drops to below 1 K. The critical temperature is highly tunable with an electrostatic gate, from about 700 mK at $2 \times 10^{13}\ cm^{-2}$ to below 200 mK at a low doping of $5 \times 10^{12}\ cm^{-2}$. For even lower doping levels, the 2D bulk becomes an insulator. We also studied the magnetic field dependence and found the upper critical field is very anisotropic. At a large carrier density of $1.5 \times 10^{13}\ cm^{-2}$ around 20 mK, B_{c2} is about 35 mT for out-of-plane magnetic field. However, for in-plane magnetic field, B_{c2} reaches 3.5 T, about 100 times larger. More intriguingly, for small magnetic fields, it is revealed that there is an intermediate quantum metal state, which has dissipation but the resistance is orders of magnitudes smaller than the normal metallic state.

The discovery of field induced superconductivity and topological insulator behavior in the exact same real two dimensional system is quite unique and encouraging. In principle, one could tune monolayer WTe_2 from one of the exotic states to the other reversely and reliably, and all one needs is just an electrostatic gate! One could also think of making a generic QSHI to 2D-SC junction from the same material by designing the gate geometry and study the interplay between these two quantum states. Moreover, it is proposed that there are Majorana zero modes attached to the superconductor-magnetic interface at the edge of QSHI [110]. Based on this proposal, one could create Majorana zero modes by combining monolayer WTe_2 with another magnetic insulator.

BIBLIOGRAPHY

[1] N. M. R. Peres and E. V. Castro. Algebraic solution of a graphene layer in transverse electric and perpendicular magnetic fields. *Journal of Physics-Condensed Matter*, 19(40), 2007.

[2] K. S. Novoselov, A. K. Geim, S. V. Morozov, D. Jiang, Y. Zhang, S. V. Dubonos, I. V. Grigorieva, and A. A. Firsov. Electric field effect in atomically thin carbon films. *Science*, 306(5696):666–669, 2004.

[3] P. Blake, E. W. Hill, A. H. Castro Neto, K. S. Novoselov, D. Jiang, R. Yang, T. J. Booth, and A. K. Geim. Making graphene visible. *Applied Physics Letters*, 91(6), 2007.

[4] A. H. Castro Neto, F. Guinea, N. M. R. Peres, K. S. Novoselov, and A. K. Geim. The electronic properties of graphene. *Reviews of Modern Physics*, 81(1):109–162, 2009.

[5] P. R. Wallace. The band theory of graphite. *Physical Review*, 71(7):476–476, 1947.

[6] A. K. Geim and K. S. Novoselov. The rise of graphene. *Nature Materials*, 6(3):183–191, 2007.

[7] K. Vonklitzing, G. Dorda, and M. Pepper. New method for high-accuracy determination of the fine-structure constant based on quantized hall resistance. *Physical Review Letters*, 45(6):494–497, 1980.

[8] K. S. Novoselov, A. K. Geim, S. V. Morozov, D. Jiang, M. I. Katsnelson, I. V. Grigorieva, S. V. Dubonos, and A. A. Firsov. Two-dimensional gas of massless dirac fermions in graphene. *Nature*, 438(7065):197–200, 2005.

[9] Y. B. Zhang, Y. W. Tan, H. L. Stormer, and P. Kim. Experimental observation of the quantum hall effect and berry's phase in graphene. *Nature*, 438(7065):201–204, 2005.

[10] K. S. Novoselov, Z. Jiang, Y. Zhang, S. V. Morozov, H. L. Stormer, U. Zeitler, J. C. Maan, G. S. Boebinger, P. Kim, and A. K. Geim. Room-temperature quantum hall effect in graphene. *Science*, 315(5817):1379–1379, 2007.

[11] H. L. Stormer, D. C. Tsui, and A. C. Gossard. The fractional quantum hall effect. *Reviews of Modern Physics*, 71(2):S298–S305, 1999.

[12] Q. H. Wang, K. Kalantar-Zadeh, A. Kis, J. N. Coleman, and M. S. Strano. Electronics and optoelectronics of two-dimensional transition metal dichalcogenides. *Nature Nanotechnology*, 7(11):699–712, 2012.

[13] D. Xiao, G. B. Liu, W. X. Feng, X. D. Xu, and W. Yao. Coupled spin and valley physics in monolayers of mos2 and other group-vi dichalcogenides. *Physical Review Letters*, 108(19), 2012.

[14] S. F. Wu, J. S. Ross, G. B. Liu, G. Aivazian, A. Jones, Z. Y. Fei, W. G. Zhu, D. Xiao, W. Yao, D. Cobden, and X. D. Xu. Electrical tuning of valley magnetic moment through symmetry control in bilayer mos2. *Nature Physics*, 9(3):149–153, 2013.

[15] X. F. Qian, J. W. Liu, L. Fu, and J. Li. Quantum spin hall effect in two-dimensional transition metal dichalcogenides. *Science*, 346(6215):1344–1347, 2014.

[16] A. H. Castro Neto. Charge density wave, superconductivity, and anomalous metallic behavior in 2d transition metal dichalcogenides. *Physical Review Letters*, 86(19):4382–4385, 2001.

[17] J. S. Ross, S. F. Wu, H. Y. Yu, N. J. Ghimire, A. M. Jones, G. Aivazian, J. Q. Yan, D. G. Mandrus, D. Xiao, W. Yao, and X. D. Xu. Electrical control of neutral and charged excitons in a monolayer semiconductor. *Nature Communications*, 4, 2013.

[18] X. D. Xu, W. Yao, D. Xiao, and T. F. Heinz. Spin and pseudospins in layered transition metal dichalcogenides. *Nature Physics*, 10(5):343–350, 2014.

[19] K. F. Mak, K. L. He, J. Shan, and T. F. Heinz. Control of valley polarization in monolayer mos2 by optical helicity. *Nature Nanotechnology*, 7(8):494–498, 2012.

[20] T. Cao, G. Wang, W. P. Han, H. Q. Ye, C. R. Zhu, J. R. Shi, Q. Niu, P. H. Tan, E. Wang, B. L. Liu, and J. Feng. Valley-selective circular dichroism of monolayer molybdenum disulphide. *Nature Communications*, 3, 2012.

[21] X. L. Qi and S. C. Zhang. The quantum spin hall effect and topological insulators. *Physics Today*, 63(1):33–38, 2010.

[22] Charles L Kane and Eugene J Mele. Z 2 topological order and the quantum spin hall effect. *Physical review letters*, 95(14):146802, 2005.

[23] M. Konig, S. Wiedmann, C. Brune, A. Roth, H. Buhmann, L. W. Molenkamp, X. L. Qi, and S. C. Zhang. Quantum spin hall insulator state in hgte quantum wells. *Science*, 318(5851):766–770, 2007.

[24] Z. H. Zhong, N. M. Gabor, J. E. Sharping, A. L. Gaeta, and P. L. McEuen. Terahertz time-domain measurement of ballistic electron resonance in a single-walled carbon nanotube. *Nature Nanotechnology*, 3(4):201–205, 2008.

[25] C. Drexler, S. A. Tarasenko, P. Olbrich, J. Karch, M. Hirmer, F. Muller, M. Gmitra, J. Fabian, R. Yakimova, S. Lara-Avila, S. Kubatkin, M. Wang, R. Vajtai, P. M. Ajayan, J. Kono, and S. D. Ganichev. Magnetic quantum ratchet effect in graphene. *Nature Nanotechnology*, 8(2):104–107, 2013.

[26] K. F. Mak, K. L. McGill, J. Park, and P. L. McEuen. The valley hall effect in mos2 transistors. *Science*, 344(6191):1489–1492, 2014.

[27] J. C. W. Song and L. S. Levitov. Shockley-ramo theorem and long-range photocurrent response in gapless materials. *Physical Review B*, 90(7), 2014.

[28] J. W. McIver, D. Hsieh, H. Steinberg, P. Jarillo-Herrero, and N. Gedik. Control over topological insulator photocurrents with light polarization. *Nature Nanotechnology*, 7(2):96–100, 2012.

[29] D. Sun, G. Aivazian, A. M. Jones, J. S. Ross, W. Yao, D. Cobden, and X. D. Xu. Ultrafast hot-carrier-dominated photocurrent in graphene. *Nature Nanotechnology*, 7(2):114–118, 2012.

[30] X. D. Xu, N. M. Gabor, J. S. Alden, A. M. van der Zande, and P. L. McEuen. Photothermoelectric effect at a graphene interface junction. *Nano Letters*, 10(2):562–566, 2010.

[31] Q. Ma, N. M. Gabor, T. I. Andersen, N. L. Nair, K. Watanabe, T. Taniguchi, and P. Jarillo-Herrero. Competing channels for hot-electron cooling in graphene. *Physical Review Letters*, 112(24), 2014.

[32] K. I. Bolotin, K. J. Sikes, Z. Jiang, M. Klima, G. Fudenberg, J. Hone, P. Kim, and H. L. Stormer. Ultrahigh electron mobility in suspended graphene. *Solid State Communications*, 146(9-10):351–355, 2008.

[33] C. R. Dean, A. F. Young, I. Meric, C. Lee, L. Wang, S. Sorgenfrei, K. Watanabe, T. Taniguchi, P. Kim, K. L. Shepard, and J. Hone. Boron nitride substrates for high-quality graphene electronics. *Nature Nanotechnology*, 5(10):722–726, 2010.

[34] L. Wang, I. Meric, P. Y. Huang, Q. Gao, Y. Gao, H. Tran, T. Taniguchi, K. Watanabe, L. M. Campos, D. A. Muller, J. Guo, P. Kim, J. Hone, K. L. Shepard, and C. R. Dean. One-dimensional electrical contact to a two-dimensional material. *Science*, 342(6158):614–617, 2013.

[35] L. Wang, I. Gutierrez-Lezama, C. Barreteau, N. Ubrig, E. Giannini, and A. F. Morpurgo. Tuning magnetotransport in a compensated semimetal at the atomic scale. *Nature Communications*, 6, 2015.

[36] W. Shockley. Currents to conductors induced by a moving point charge. *Journal of Applied Physics*, 9(10):635–636, 1938.

[37] Simon Ramo. Currents induced by electron motion. *Proceedings of the IRE*, 27(9):584–585, 1939.

[38] Z. He. Review of the shockley-ramo theorem and its application in semiconductor gamma-ray detectors. *Nuclear Instruments & Methods in Physics Research Section a-Accelerators Spectrometers Detectors and Associated Equipment*, 463(1-2):250–267, 2001.

[39] S. Kabashima. Electrical properties of tungsten-ditelluride wte2. *Journal of the Physical Society of Japan*, 21(5):945–+, 1966.

[40] B.E. Brown. The crystal structures of wte2 and high-temperature mote2. *Acta Crystallographica*, 20(2):268–274, 1966.

[41] E. Revolinsky and D. Beerntsen. Electrical properties of mote2-wte2 + mose2-wse2 systems. *Journal of Applied Physics*, 35(7):2086–&, 1964.

[42] J. Jiang, F. Tang, X. C. Pan, H. M. Liu, X. H. Niu, Y. X. Wang, D. F. Xu, H. F. Yang, B. P. Xie, F. Q. Song, P. Dudin, T. K. Kim, M. Hoesch, P. K. Das, I. Vobornik, X. G. Wan, and D. L. Feng. Signature of strong spin-orbital coupling in the large nonsaturating magnetoresistance material wte2. *Physical Review Letters*, 115(16), 2015.

[43] M. N. Ali, J. Xiong, S. Flynn, J. Tao, Q. D. Gibson, L. M. Schoop, T. Liang, N. Haldolaarachchige, M. Hirschberger, N. P. Ong, and R. J. Cava. Large, non-saturating magnetoresistance in wte2. *Nature*, 514(7521):205–+, 2014.

[44] F. C. Chen, H. Y. Lv, X. Luo, W. J. Lu, Q. L. Pei, G. T. Lin, Y. Y. Han, X. B. Zhu, W. H. Song, and Y. P. Sun. Extremely large magnetoresistance in the type-ii weyl semimetal mote2. *Physical Review B*, 94(23), 2016.

[45] T. Liang, Q. Gibson, M. N. Ali, M. H. Liu, R. J. Cava, and N. P. Ong. Ultrahigh mobility and giant magnetoresistance in the dirac semimetal cd3as2. *Nature Materials*, 14(3):280–284, 2015.

[46] C. Shekhar, A. K. Nayak, Y. Sun, M. Schmidt, M. Nicklas, I. Leermakers, U. Zeitler, Y. Skourski, J. Wosnitza, Z. K. Liu, Y. L. Chen, W. Schnelle, H. Borrmann, Y. Grin, C. Felser, and B. H. Yan. Extremely large magnetoresistance and ultrahigh mobility in the topological weyl semimetal candidate nbp. *Nature Physics*, 11(8):645–+, 2015.

[47] Z. J. Yuan, H. Lu, Y. J. Liu, J. F. Wang, and S. Jia. Large magnetoresistance in compensated semimetals taas2 and nbas2. *Physical Review B*, 93(18), 2016.

[48] H. Y. Lv, W. J. Lu, D. F. Shao, Y. Liu, S. G. Tan, and Y. P. Sun. Perfect charge compensation in wte2 for the extraordinary magnetoresistance: From bulk to monolayer. *Epl*, 110(3), 2015.

[49] I. Pletikosic, M. N. Ali, A. V. Fedorov, R. J. Cava, and T. Valla. Electronic structure basis for the extraordinary magnetoresistance in wte2. *Physical Review Letters*, 113(21), 2014.

[50] P. L. Cai, J. Hu, L. P. He, J. Pan, X. C. Hong, Z. Zhang, J. Zhang, J. Wei, Z. Q. Mao, and S. Y. Li. Drastic pressure effect on the extremely large magnetoresistance in wte2: Quantum oscillation study. *Physical Review Letters*, 115(5), 2015.

[51] F. X. Xiang, M. Veldhorst, S. X. Dou, and X. L. Wang. Multiple fermi pockets revealed by shubnikov-de haas oscillations in wte2. *Epl*, 112(3), 2015.

[52] Z. W. Zhu, X. Lin, J. Liu, B. Fauque, Q. Tao, C. L. Yang, Y. G. Shi, and K. Behnia. Quantum oscillations, thermoelectric coefficients, and the fermi surface of semimetallic wte2. *Physical Review Letters*, 114(17), 2015.

[53] Y. Y. Lv, B. B. Zhang, X. Li, P. Pang, F. Zhang, D. J. Lin, J. Zhou, S. H. Yao, Y. B. Chen, S. T. Zhang, M. H. Lu, Z. K. Liu, Y. L. Chen, and Y. F. Chen. Dramatically decreased magnetoresistance in non-stoichiometric wte2 crystals. *Scientific Reports*, 6, 2016.

[54] A. A. Soluyanov, D. Gresch, Z. J. Wang, Q. S. Wu, M. Troyer, X. Dai, and B. A. Bernevig. Type-ii weyl semimetals. *Nature*, 527(7579):495–498, 2015.

[55] S. Y. Xu, I. Belopolski, N. Alidoust, M. Neupane, G. Bian, C. L. Zhang, R. Sankar, G. Q. Chang, Z. J. Yuan, C. C. Lee, S. M. Huang, H. Zheng, J. Ma, D. S. Sanchez, B. K. Wang, A. Bansil, F. C. Chou, P. P. Shibayev, H. Lin, S. Jia, and M. Z. Hasan. Discovery of a weyl fermion semimetal and topological fermi arcs. *Science*, 349(6248):613–617, 2015.

[56] L. X. Yang, Z. K. Liu, Y. Sun, H. Peng, H. F. Yang, T. Zhang, B. Zhou, Y. Zhang, Y. F. Guo, M. Rahn, D. Prabhakaran, Z. Hussain, S. K. Mo, C. Felser, B. Yan, and Y. L. Chen. Weyl semimetal phase in the non-centrosymmetric compound taas. *Nature Physics*, 11(9):728–+, 2015.

[57] S. Y. Xu, N. Alidoust, I. Belopolski, Z. J. Yuan, G. Bian, T. R. Chang, H. Zheng, V. N. Strocov, D. S. Sanchez, G. Q. Chang, C. L. Zhang, D. X. Mou, Y. Wu, L. N. Huang, C. C. Lee, S. M. Huang, B. K. Wang, A. Bansil, H. T. Jeng, T. Neupert, A. Kaminski, H. Lin, S. Jia, and M. Z. Hasan. Discovery of a weyl fermion state with fermi arcs in niobium arsenide. *Nature Physics*, 11(9):748–+, 2015.

[58] Y. Wu, D. X. Mou, N. H. Jo, K. W. Sun, L. N. Huang, S. L. Bud'ko, P. C. Canfield,

and A. Kaminski. Observation of fermi arcs in the type-ii weyl semimetal candidate wte2. *Physical Review B*, 94(12):5, 2016.

[59] C. L. Wang, Y. Zhang, J. W. Huang, S. M. Nie, G. D. Liu, A. J. Liang, Y. X. Zhang, B. Shen, J. Liu, C. Hu, Y. Ding, D. F. Liu, Y. Hu, S. L. He, L. Zhao, L. Yu, J. Hu, J. Wei, Z. Q. Mao, Y. G. Shi, X. W. Jia, F. F. Zhang, S. J. Zhang, F. Yang, Z. M. Wang, Q. J. Peng, H. M. Weng, X. Dai, Z. Fang, Z. Y. Xu, C. T. Chen, and X. J. Zhou. Observation of fermi arc and its connection with bulk states in the candidate type-ii weyl semimetal wte2. *Physical Review B*, 94(24), 2016.

[60] F. Y. Bruno, A. Tamai, Q. S. Wu, I. Cucchi, C. Barreteau, A. de la Torre, S. M. Walker, S. Ricco, Z. Wang, T. K. Kim, M. Hoesch, M. Shi, N. C. Plumb, E. Giannini, A. A. Soluyanov, and F. Baumberger. Observation of large topologically trivial fermi arcs in the candidate type-ii weyl semimetal wte2. *Physical Review B*, 94(12), 2016.

[61] Y. J. Wang, E. F. Liu, H. M. Liu, Y. M. Pan, L. Q. Zhang, J. W. Zeng, Y. J. Fu, M. Wang, K. Xu, Z. Huang, Z. L. Wang, H. Z. Lu, D. Y. Xing, B. G. Wang, X. G. Wan, and F. Miao. Gate-tunable negative longitudinal magnetoresistance in the predicted type-ii weyl semimetal wte2. *Nature Communications*, 7, 2016.

[62] X. C. Pan, X. L. Chen, H. M. Liu, Y. Q. Feng, Z. X. Wei, Y. H. Zhou, Z. H. Chi, L. Pi, F. Yen, F. Q. Song, X. G. Wan, Z. R. Yang, B. G. Wang, G. H. Wang, and Y. H. Zhang. Pressure-driven dome-shaped superconductivity and electronic structural evolution in tungsten ditelluride. *Nature Communications*, 6, 2015.

[63] D. F. Kang, Y. Z. Zhou, W. Yi, C. L. Yang, J. Guo, Y. G. Shi, S. Zhang, Z. Wang, C. Zhang, S. Jiang, A. G. Li, K. Yang, Q. Wu, G. M. Zhang, L. L. Sun, and Z. X. Zhao. Superconductivity emerging from a suppressed large magnetoresistant state in tungsten ditelluride. *Nature Communications*, 6, 2015.

[64] Y. P. Qi, P. G. Naumov, M. N. Ali, C. R. Rajamathi, W. Schnelle, O. Barkalov,

M. Hanfland, S. C. Wu, C. Shekhar, Y. Sun, V. Suss, M. Schmidt, U. Schwarz, E. Pippel, P. Werner, R. Hillebrand, T. Forster, E. Kampert, S. Parkin, R. J. Cava, C. Felser, B. H. Yan, and S. A. Medvedev. Superconductivity in weyl semimetal candidate mote2. *Nature Communications*, 7, 2016.

[65] H. Sakai, K. Ikeura, M. S. Bahramy, N. Ogawa, D. Hashizume, J. Fujioka, Y. Tokura, and S. Ishiwata. Critical enhancement of thermopower in a chemically tuned polar semimetal mote2. *Science Advances*, 2(11), 2016.

[66] S. Cho, S. H. Kang, H. S. Yu, H. W. Kim, W. Ko, S. W. Hwang, W. H. Han, D. H. Choe, Y. H. Jung, K. J. Chang, Y. H. Lee, H. Yang, and S. W. Kim. Te vacancy-driven superconductivity in orthorhombic molybdenum ditelluride. *2d Materials*, 4(2), 2017.

[67] Y. F. Zhao, H. W. Liu, J. Q. Yan, W. An, J. Liu, X. Zhang, H. C. Wang, Y. Liu, H. Jiang, Q. Li, Y. Wang, X. Z. Li, D. Mandrus, X. C. Xie, M. H. Pan, and J. Wang. Anisotropic magnetotransport and exotic longitudinal linear magnetoresistance in wte2 crystals. *Physical Review B*, 92(4), 2015.

[68] L. R. Thoutam, Y. L. Wang, Z. L. Xiao, S. Das, A. Luican-Mayer, R. Divan, G. W. Crabtree, and W. K. Kwok. Temperature-dependent three-dimensional anisotropy of the magnetoresistance in wte2. *Physical Review Letters*, 115(4), 2015.

[69] V. Fatemi, Q. D. Gibson, K. Watanabe, T. Taniguchi, R. J. Cava, and P. Jarillo-Herrero. Magnetoresistance and quantum oscillations of an electrostatically tuned semimetal-to-metal transition in ultrathin wte2. *Physical Review B*, 95(4):5, 2017.

[70] P. C. Lu, J. S. Kim, J. Yang, H. Gao, J. F. Wu, D. X. Shao, B. Li, D. W. Zhou, J. Sun, D. Akinwande, D. Y. Xing, and J. F. Lin. Origin of superconductivity in the weyl semimetal wte2 under pressure. *Physical Review B*, 94(22):8, 2016.

[71] Y. H. Zhou, X. L. Chen, N. N. Li, R. R. Zhang, X. F. Wang, C. An, Y. Zhou, X. C. Pan,

F. Q. Song, B. G. Wang, W. G. Yang, Z. R. Yang, and Y. H. Zhang. Pressure-induced td to 1t ' structural phase transition in wte2. *Aip Advances*, 6(7), 2016.

[72] Q. J. Song, H. F. Wang, X. L. Xu, X. C. Pan, Y. L. Wang, F. Q. Song, X. G. Wan, and L. Dai. The polarization-dependent anisotropic raman response of few-layer and bulk wte2 under different excitation wavelengths. *Rsc Advances*, 6(105):103830–103837, 2016.

[73] Y. Cao, A. Mishchenko, G. L. Yu, E. Khestanova, A. P. Rooney, E. Prestat, A. V. Kretinin, P. Blake, M. B. Shalom, C. Woods, J. Chapman, G. Balakrishnan, I. V. Grigorieva, K. S. Novoselov, B. A. Piot, M. Potemski, K. Watanabe, T. Taniguchi, S. J. Haigh, A. K. Geim, and R. V. Gorbachev. Quality heterostructures from two-dimensional crystals unstable in air by their assembly in inert atmosphere. *Nano Letters*, 15(8):4914–4921, 2015.

[74] L. K. Li, G. J. Ye, V. Tran, R. X. Fei, G. R. Chen, H. C. Wang, J. Wang, K. Watanabe, T. Taniguchi, L. Yang, X. H. Chen, and Y. B. Zhang. Quantum oscillations in a two-dimensional electron gas in black phosphorus thin films. *Nature Nanotechnology*, 10(7):608–+, 2015.

[75] Y. J. Yu, F. Y. Yang, X. F. Lu, Y. J. Yan, Y. H. Cho, L. G. Ma, X. H. Niu, S. Kim, Y. W. Son, D. L. Feng, S. Y. Li, S. W. Cheong, X. H. Chen, and Y. B. Zhang. Gate-tunable phase transitions in thin flakes of 1t-tas2. *Nature Nanotechnology*, 10(3):270–276, 2015.

[76] E. Z. Zhang, R. Chen, C. Huang, J. H. Yu, K. T. Zhang, W. Y. Wang, S. S. Liu, J. W. Ling, X. G. Wan, H. Z. Lu, and F. X. Xiu. Tunable positive to negative magnetoresistance in atomically thin wte2. *Nano Letters*, 17(2):878–885, 2017.

[77] A. D. Caviglia, M. Gabay, S. Gariglio, N. Reyren, C. Cancellieri, and J. M. Triscone.

Tunable rashba spin-orbit interaction at oxide interfaces. *Physical Review Letters*, 104(12), 2010.

[78] N. Gillgren, D. Wickramaratne, Y. M. Shi, T. Espiritu, J. W. Yang, J. Hu, J. Wei, X. Liu, Z. Q. Mao, K. Watanabe, T. Taniguchi, M. Bockrath, Y. Barlas, R. K. Lake, and C. N. Lau. Gate tunable quantum oscillations in air-stable and high mobility few-layer phosphorene heterostructures. *2d Materials*, 2(1), 2015.

[79] A. Roth. Nonlocal transport in the quantum spin hall state (july, pg 294, 2009). *Science*, 330(6012):1746–1746, 2010.

[80] M. Bockrath, D. H. Cobden, J. Lu, A. G. Rinzler, R. E. Smalley, L. Balents, and P. L. McEuen. Luttinger-liquid behaviour in carbon nanotubes. *Nature*, 397(6720):598–601, 1999.

[81] C. J. Wu, B. A. Bernevig, and S. C. Zhang. Helical liquid and the edge of quantum spin hall systems. *Physical Review Letters*, 96(10), 2006.

[82] T. L. Schmidt, S. Rachel, F. von Oppen, and L. I. Glazman. Inelastic electron backscattering in a generic helical edge channel. *Physical Review Letters*, 108(15), 2012.

[83] J. I. Vayrynen, F. Geissler, and L. I. Glazman. Magnetic moments in a helical edge can make weak correlations seem strong. *Physical Review B*, 93(24), 2016.

[84] E. Y. Ma, M. R. Calvo, J. Wang, B. Lian, M. Muhlbauer, C. Brune, Y. T. Cui, K. J. Lai, W. Kundhikanjana, Y. L. Yang, M. Baenninger, M. Konig, C. Ames, H. Buhmann, P. Leubner, L. W. Molenkamp, S. C. Zhang, D. Goldhaber-Gordon, M. A. Kelly, and Z. X. Shen. Unexpected edge conduction in mercury telluride quantum wells under broken time-reversal symmetry. *Nature Communications*, 6, 2015.

[85] Y. T. Cui, B. Wen, E. Y. Ma, G. Diankov, Z. Han, F. Amet, T. Taniguchi, K. Watanabe, D. Goldhaber-Gordon, C. R. Dean, and Z. X. Shen. Unconventional correlation

between quantum hall transport quantization and bulk state filling in gated graphene devices. *Physical Review Letters*, 117(18), 2016.

[86] M. T. Allen, O. Shtanko, I. C. Fulga, A. R. Akhmerov, K. Watanabe, T. Taniguchi, P. Jarillo-Herrero, L. S. Levitov, and A. Yacoby. Spatially resolved edge currents and guided-wave electronic states in graphene. *Nature Physics*, 12(2):128–133, 2016.

[87] E. Y. Ma, Y. T. Cui, K. Ueda, S. J. Tang, K. Chen, N. Tamura, P. M. Wu, J. Fujioka, Y. Tokura, and Z. X. Shen. Mobile metallic domain walls in an all-in-all-out magnetic insulator. *Science*, 350(6260):538–541, 2015.

[88] Xiaoyu Wu, Urko Petralanda, Lu Zheng, Yuan Ren, Rongwei Hu, Sang-Wook Cheong, Sergey Artyukhin, and Keji Lai. Low-energy structural dynamics of ferroelectric domain walls in hexagonal rare-earth manganites. 2017.

[89] P. Ponath, K. Fredrickson, A. B. Posadas, Y. Ren, X. Y. Wu, R. K. Vasudevan, M. B. Okatan, S. Jesse, T. Aoki, M. R. McCartney, D. J. Smith, S. V. Kalinin, K. Lai, and A. A. Demkov. Carrier density modulation in a germanium heterostructure by ferroelectric switching. *Nature Communications*, 6, 2015.

[90] M. Knap, J. D. Sau, B. I. Halperin, and E. Demler. Transport in two-dimensional disordered semimetals. *Physical Review Letters*, 113(18), 2014.

[91] L. Fu and C. L. Kane. Superconducting proximity effect and majorana fermions at the surface of a topological insulator. *Physical Review Letters*, 100(9), 2008.

[92] A. Shalnikov. Superconducting thin films. *Nature*, 142:74–74, 1938.

[93] N. Reyren, S. Thiel, A. D. Caviglia, L. F. Kourkoutis, G. Hammerl, C. Richter, C. W. Schneider, T. Kopp, A. S. Ruetschi, D. Jaccard, M. Gabay, D. A. Muller, J. M. Triscone, and J. Mannhart. Superconducting interfaces between insulating oxides. *Science*, 317(5842):1196–1199, 2007.

[94] A. D. Caviglia, S. Gariglio, N. Reyren, D. Jaccard, T. Schneider, M. Gabay, S. Thiel, G. Hammerl, J. Mannhart, and J. M. Triscone. Electric field control of the laalo(3)/srtio(3) interface ground state. *Nature*, 456(7222):624–627, 2008.

[95] Y. Saito, T. Nojima, and Y. Iwasa. Highly crystalline 2d superconductors. *Nature Reviews Materials*, 2(1), 2017.

[96] L. Wang, I. Gutierrez-Lezama, C. Barreteau, D. K. Ki, E. Giannini, and A. F. Morpurgo. Direct observation of a long-range field effect from gate tuning of nonlocal conductivity. *Physical Review Letters*, 117(17), 2016.

[97] J. T. Ye, Y. J. Zhang, R. Akashi, M. S. Bahramy, R. Arita, and Y. Iwasa. Superconducting dome in a gate-tuned band insulator. *Science*, 338(6111):1193–1196, 2012.

[98] Y. Saito, Y. Nakamura, M. S. Bahramy, Y. Kohama, J. T. Ye, Y. Kasahara, Y. Nakagawa, M. Onga, M. Tokunaga, T. Nojima, Y. Yanase, and Y. Iwasa. Superconductivity protected by spin-valley locking in ion-gated mos2. *Nature Physics*, 12(2):144–+, 2016.

[99] Y. Saito, Y. Nakamura, M. S. Bahramy, Y. Kohama, J. T. Ye, Y. Kasahara, Y. Nakagawa, M. Onga, M. Tokunaga, T. Nojima, Y. Yanase, and Y. Iwasa. Superconductivity protected by spin-valley locking in ion-gated mos2. *Nature Physics*, 12(2):144–+, 2016.

[100] S. L. Sondhi, S. M. Girvin, J. P. Carini, and D. Shahar. Continuous quantum phase transitions. *Reviews of Modern Physics*, 69(1):315–333, 1997.

[101] A. M. Goldman. Superconductor-insulator transitions. *International Journal of Modern Physics B*, 24(20-21):4081–4101, 2010.

[102] Y. Xing, H. M. Zhang, H. L. Fu, H. W. Liu, Y. Sun, J. P. Peng, F. Wang, X. Lin, X. C. Ma, Q. K. Xue, J. Wang, and X. C. Xie. Quantum griffiths singularity of superconductor-metal transition in ga thin films. *Science*, 350(6260):542–545, 2015.

[103] A. M. Clogston and New Jersey Bell Telephone Laboratories, Murray Hill. Upper limit for the critical field in hard superconductors. *Physical Review Letters*, 9(6):266, 1962.

[104] B. S. Chandrasekhar. A note on the maximum critical field of high-field superconductors. *Applied Physics Letters*, 1(1):7–8, 1962.

[105] D. Ephron, A. Yazdani, A. Kapitulnik, and M. R. Beasley. Observation of quantum dissipation in the vortex state of a highly disordered superconducting thin film. *Physical Review Letters*, 76(9):1529–1532, 1996.

[106] C. Christiansen, L. M. Hernandez, and A. M. Goldman. Evidence of collective charge behavior in the insulating state of ultrathin films of superconducting metals. *Physical Review Letters*, 88(3), 2002.

[107] M. A. Steiner, N. P. Breznay, and A. Kapitulnik. Approach to a superconductor-to-bose-insulator transition in disordered films. *Physical Review B*, 77(21), 2008.

[108] A. W. Tsen, B. Hunt, Y. D. Kim, Z. J. Yuan, S. Jia, R. J. Cava, J. Hone, P. Kim, C. R. Dean, and A. N. Pasupathy. Nature of the quantum metal in a two-dimensional crystalline superconductor. *Nature Physics*, 12(3):208–+, 2016.

[109] E. Shimshoni, A. Auerbach, and A. Kapitulnik. Transport through quantum melts. *Physical Review Letters*, 80(15):3352–3355, 1998.

[110] M. Z. Hasan and C. L. Kane. Colloquium: Topological insulators. *Reviews of Modern Physics*, 82(4):3045–3067, 2010.

[111] Y. C. Jiang, J. Gao, and L. Wang. Raman fingerprint for semi-metal wte2 evolving from bulk to monolayer. *Scientific Reports*, 6:7, 2016.

[112] Y. Kim, Y. I. Jhon, J. Park, J. H. Kim, S. Lee, and Y. M. Jhon. Anomalous raman scattering and lattice dynamics in mono- and few-layer wte2. *Nanoscale*, 8(4):2309–2316, 2016.

[113] M. Kim, S. Han, J. H. Kim, J. U. Lee, Z. Lee, and H. Cheong. Determination of the thickness and orientation of few-layer tungsten ditelluride using polarized raman spectroscopy. *2d Materials*, 3(3), 2016.

[114] W. D. Kong, S. F. Wu, P. Richard, C. S. Lian, J. T. Wang, C. L. Yang, Y. G. Shi, and H. Ding. Raman scattering investigation of large positive magnetoresistance material wte2. *Applied Physics Letters*, 106(8), 2015.

[115] J. Lee, F. Ye, Z. H. Wang, R. Yang, J. Hu, Z. Q. Mao, J. Wei, and P. X. L. Feng. Single- and few-layer wte2 and their suspended nanostructures: Raman signatures and nanomechanical resonances. *Nanoscale*, 8(15):7854–7860, 2016.

Appendix A

A.1 Shockley-Ramo theorem

The Shockley-Ramon theorem was originally established for dealing with charge detection problem in a vacuum tube. In the original problem (take a γ-ray spectrometer as an example) the γ radiation on a typical semiconductor would generate free electron-hole pairs within the device, labeled as q, these free moving charges generate an instantaneous electric field $\mathbf{E}$, which induces charge Q on the electrodes. Before the discovery of Shockley-Ramo theorem, the calculation of this long-range charge response is rather complicated due to the processes discussed above. Shockley and Ramo reviewed this from the perspective of conservation of energy, and found that the induced charge can be calculated in a much easier way, with the help of an auxiliary potential (field), so called weighting potential (field). The derivation could also be extended to the case with stationary charges instead of vacuum as discussed below.

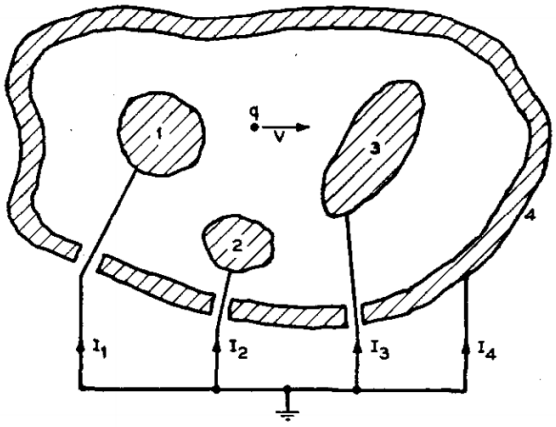

Figure A.1: Schematic of a vacuum tube. (Figure taken from Ref. [36])

To begin with, we consider the following configuration (see Fig. A.1): all electrodes are set to be at constant voltages $V_i(i = 1, 2, ...N)$, with boundaries S_i; inside the device, there are a free moving charge q and background stationary charges of carrier density $\rho(r)$. The electrical potential of the system $\Phi(r)$ satisfies the following Poisson's equation with Dirichlet boundary conditions.

$$\nabla^2\Phi(r) = -(\rho(r) + q\delta(r))/\epsilon,$$

$$\Phi|_{S_i} = V_i(i = 1, 2, ...N).$$

With $\Phi(r)$, the electric field is determined to be $\mathbf{E} = -\nabla\mathbf{\Phi}(\mathbf{r})$. Then we can calculate the charge collected by each electrode $Q_i = \oint_{S_i} \epsilon\mathbf{E} \cdot \mathbf{dS}$. This is basically the traditional way of calculating the charge accumulated at each electrode. However, due to the linear superposition, the electrical potential can be separated into two parts, $\Phi = \psi + \phi$, ψ is the auxiliary or weighting field. ψ and ϕ satisfy the following equation and boundary conditions.

$$\nabla^2\psi(r) = 0, \tag{A.1}$$

$$\psi|_{S_i} = V_i(i = 1, 2, ...N), \tag{A.2}$$

$$\nabla^2\phi(r) = -(\rho(r) + q\delta(r))/\epsilon, \tag{A.3}$$

$$\phi|_{S_i} = 0(i = 1, 2, ...N). \tag{A.4}$$

$\mathbf{E_1} = -\nabla\psi$, $\mathbf{E_2} = -\nabla\phi$ are electric fields correspond to the electric potentials introduced above. Due to the conservation of energy, for $\rho(r)$ and q in the electric potential $\phi(r)$, the work done by $\mathbf{E_2}$ on charge q is

$$\int_{\mathbf{r_i}}^{\mathbf{r_f}} q\mathbf{E_2'} \cdot \mathbf{dr} = \frac{\mathbf{1}}{\mathbf{2}} \int_{\mathbf{V}} \epsilon(\mathbf{E_{2i}^2} - \mathbf{E_{2f}^2})\mathbf{d}\tau. \tag{A.5}$$

$\mathbf{E_2'}$ is part of $\mathbf{E_2}$ except for the self field of charge q. On the other hand, the total work done by $\mathbf{E_1}$ and $\mathbf{E_2}$ on q is

$$\int_{\mathbf{r_i}}^{\mathbf{r_f}} q(\mathbf{E_1} + \mathbf{E_2'}) \cdot \mathbf{dr} = \sum_{\mathbf{i=1}}^{\mathbf{N}} \mathbf{V_i}\mathbf{\Delta Q_i} + \frac{\mathbf{1}}{\mathbf{2}} \int_{\mathbf{V}} \epsilon[(\mathbf{E_1} + \mathbf{E_{2i}})^\mathbf{2} - (\mathbf{E_1} + \mathbf{E_{2f}})^\mathbf{2}]\mathbf{d}\tau. \tag{A.6}$$

Here, $\sum_{i=1}^{N} V_i \Delta Q_i$ is the work done by the external power supply. With Green's identity and equation A.1, A.4,

$$\int_V \mathbf{E_1} \cdot \mathbf{E_2} \mathbf{d}\tau = \int_{\mathbf{V}} \nabla\psi \cdot \nabla\phi \mathbf{d}\tau = \oint_{\mathbf{S}} \phi \nabla\psi \cdot \mathbf{dS} - \int_{\mathbf{V}} \phi \nabla^{\mathbf{2}} \psi \mathbf{d}\tau = \mathbf{0}.$$

So equation A.6 can be further simplified to

$$\int_{\mathbf{r_i}}^{\mathbf{r_f}} q(\mathbf{E_1} + \mathbf{E_2'}) \cdot \mathbf{dr} = \sum_{\mathbf{i=1}}^{\mathbf{N}} \mathbf{V_i \Delta Q_i} + \frac{\mathbf{1}}{\mathbf{2}} \int_{\mathbf{V}} \epsilon(\mathbf{E_{2i}^2} - \mathbf{E_{2f}^2}) \mathbf{d}\tau. \tag{A.7}$$

Combine equation A.7 and A.5, we have

$$\int_{\mathbf{r_i}}^{\mathbf{r_f}} q\mathbf{E_1} \cdot \mathbf{dr} = \sum_{\mathbf{i=1}}^{\mathbf{N}} \mathbf{V_i \Delta Q_i} = -\mathbf{q}[\psi(\mathbf{r_f}) - \psi(\mathbf{r_i})]. \tag{A.8}$$

This formula clearly shows the relationship between the induced charges on the collecting electrodes and auxiliary potential of the free moving charge. A simple case is that the potential of one of the contacts D is set to V_D, while all other contacts are grounded, then the charge accumulated on contact D becomes

$$Q_D V_D = -q[\psi(\mathbf{r_f}) - \psi(\mathbf{r_i})].$$

From equation A.1 and A.2, we know the auxiliary potential $\psi(\mathbf{r})$ is always proportional to V_i, for simplicity, we can set $V_D = 1$ (dimensionless), then $\psi(r)$ would also be dimensionless. So charge induced on electrode D is

$$Q_D = -q[\psi(\mathbf{r_f}) - \psi(\mathbf{r_i})]. \tag{A.9}$$

Here $\psi(\mathbf{r})$ is the dimensionless auxiliary potential, which satisfies following Laplacian equation with modified boundary conditions.

$$\nabla^2 \psi(r) = 0, \tag{A.10}$$

$$\psi|_{S_D} = 1, \psi|_{S_i} = 0 (S_i \neq S_D). \tag{A.11}$$

The name "weighting" comes from equation A.9 and the fact that the solution to above auxiliary potential is alway between 0 and 1 within the volume studied. From equation A.9, we can also calculate the induced current collected by the same contact,

$$I_D = \frac{dQ_D}{dt} = q\mathbf{E_1} \cdot \frac{\mathbf{dr}}{\mathbf{dt}} \tag{A.12}$$

Equation A.9 and A.12 involve no direct information of the instantaneous field $\mathbf{E}$, instead we use the charge-free weighting potential (field), which is much easier to calculate in reality. But as we mentioned in the beginning of the section, during the derivation, we do assume the electric field propagates (builds up) "instantaneously", or much faster than the movement of charges, and charges collected on contacts are induced charges, not the free moving charges themselves. This is the prerequisite when applying the Shockley-Ramo theorem.

Appendix B

B.1 WTe_2 Raman Spectroscopy

Raman spectroscopy is always used to identify different crystals or the thickness of layered materials, in which different peaks correspond to various phonon modes allowed by the symmetry. On the other hand, because of the quasi one dimensional nature of the 1T' WTe_2, its physical properties, such as the exotic magnetoresistance can have a large anisotropy both in- and out-of-plane. It is thus crucial to determine the actual crystal axes for consistency and better understanding of the system. In the bulk form, WTe_2 usually comes out in the form of a fine needle (see Fig.3.2c), of which the long axis is the tungsten chain or a-axis. However, when thinned down into few layers, it could end up in any shape, making it almost impossible to distinguish the crystal axes from the optical image. Other techniques, such as polarized Raman Spectroscopy are required in this case. With the help of transmission electron microscopy (TEM), one can establish the correspondence between the crystal axes and the polarized Raman Spectroscopy, which can be used latter as a fingerprint of the crystal axes without damage the thin flake.

For the rest of this section, I will present our polarized Raman Spectroscopy measurements on bulk WTe_2 first, and then show the low frequency Raman on a hBN covered monolayer WTe_2 sample. Figure B.1 shows the schematic polarized Raman setup we used in the experiment. The polarization of the excitation is rotated after the half wave plate (HWP), and we collect Raman signals for all polarizations. For low frequency Raman on monolayer WTe_2, we have two additional notch filters in front of the spectrometer to eliminate the Rayleigh signal.

Figure B.2a shows Raman spectroscopy measurements on a bulk WTe_2 sample, the excitation ($\lambda = 660\ nm$) is linearly polarized, in which θ is the angle between the polarization

and the a-axis of WTe_2 crystal. Four characteristic peaks above 100 cm^{-1} can be easily identified, which are located at 213, 165.5, 140.8 and 116.5 cm^{-1} respectively, consistent with previous reports [111, 112]. For linear excitation with different polarizations (θ), the peak frequencies almost do not change. However, the intensities strongly depend on the polarization as in Fig. B.2b. It is worth to mention that the polarization dependence of different peaks in the literature is rather complicated and depends on a lot of factors, such as the excitation energy [113] and the polarization configuration [114].

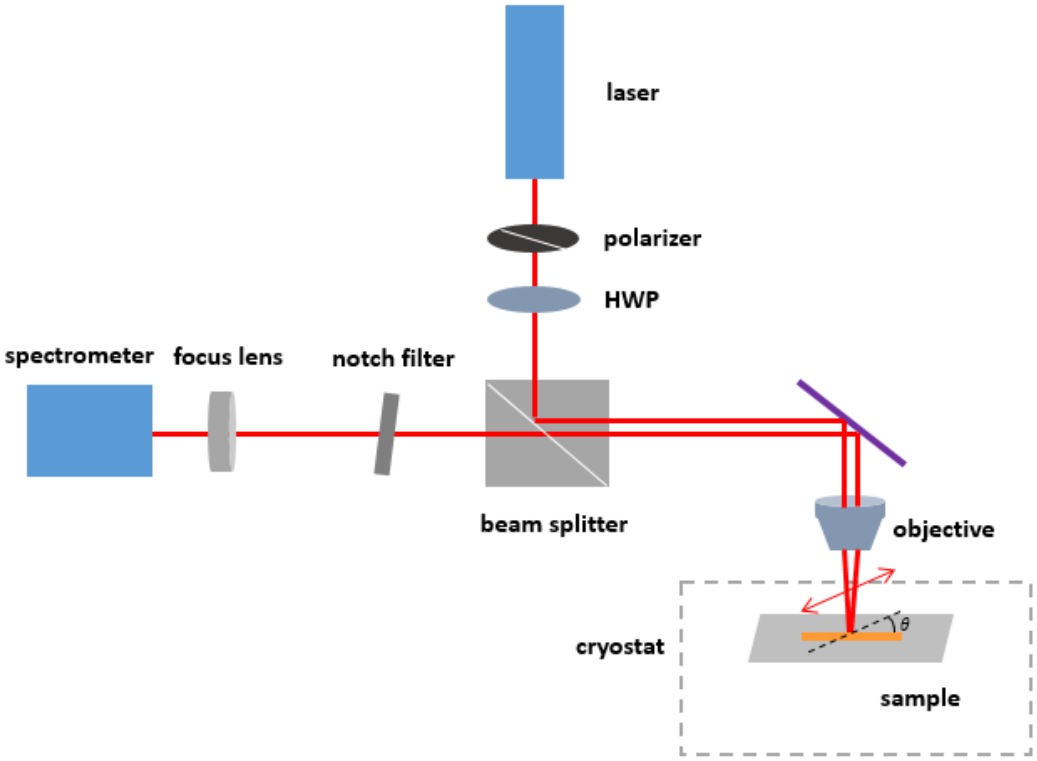

Figure B.1: Schematic setup for polarized Raman Spectroscopy

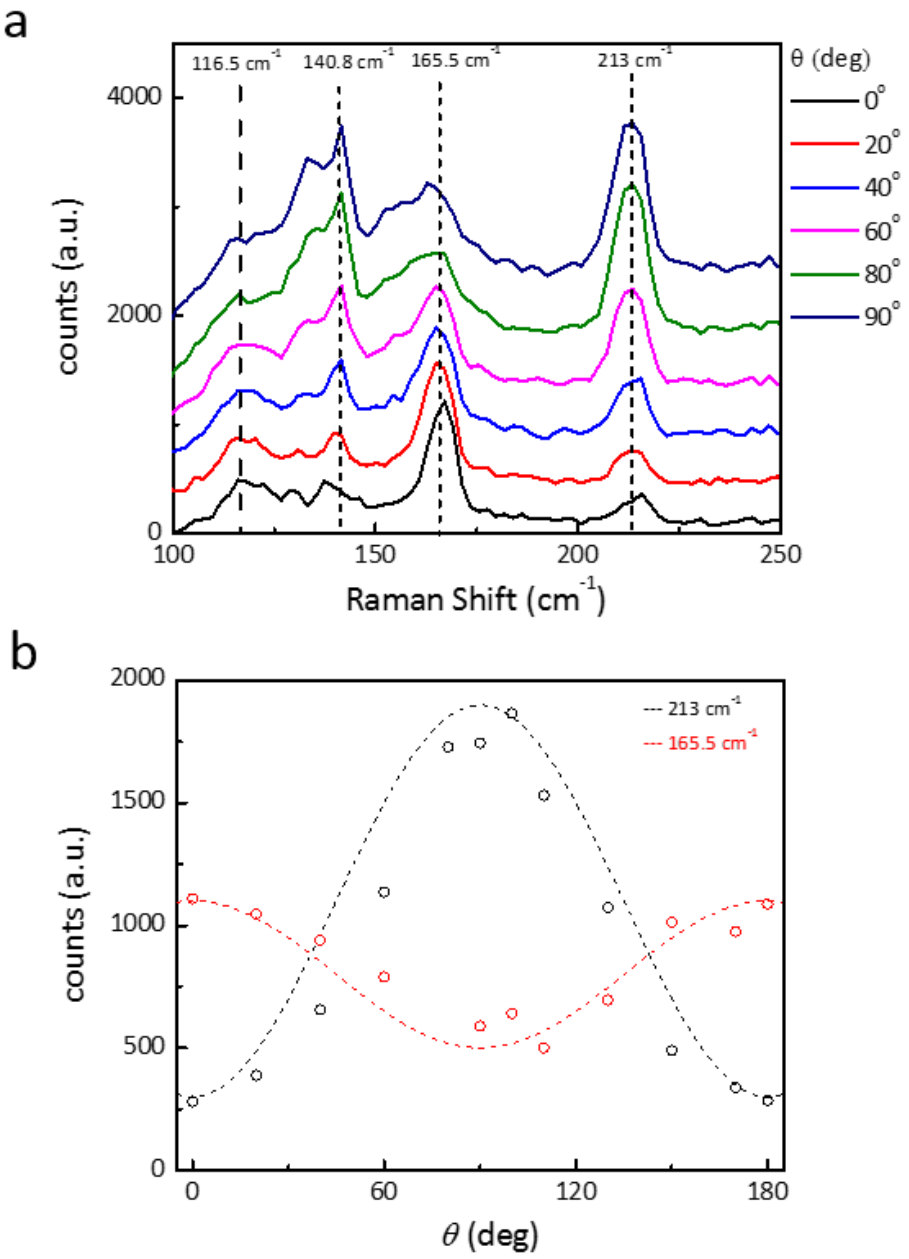

Figure B.2: a, Raman spectra of a bulk WTe_2 for different linear polarization; b, Angular dependence of the intensities of the Raman peaks at 213 and 165.5 cm^{-1} respectively.

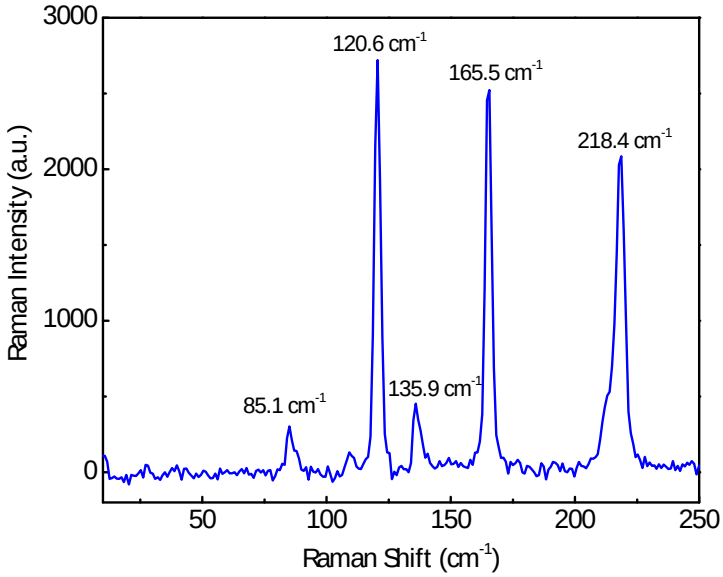

Figure B.3: Raman spectra of an encapsulated monolayer WTe_2. Five Raman peaks are clearly observed in the range 50 to 250 cm^{-1}, with wavenumbers 85.1, 120.6, 135.9, 165.5 and 218.4 cm^{-1} respectively.

When thinned down into few layers, the top surface of WTe_2 can degrade very fast and result in very different Raman spectra [113, 115]. To measure the intrinsic Raman spectra of a monolayer WTe_2, we encapsulated it using hBN flakes. Figure B.3 shows the Raman spectra of an encapsulated monolayer WTe_2, which is performed at 5 K with a 532 nm excitation laser.

Appendix C

C.1 Linear responses of monolayer and bilayer WTe_2 devices

Figures C.1 to C.4 are transfer characteristics of different edges from base temperature 1.6 K to near room temperature in monolayer devices MW1, MW2, MW3 and bilayer device BW1 respectively. A small enough ac bias of 100 μV was used to ensure linear response. As can be seen from the temperature dependences, the strength of the ZBA varies for different devices and edges. For the edge conductance values plotted in Fig. 4.10, we used the averaged value over a gate range of about 1 V (different for different edges) near $V_g = 0$, where the plateau presents. In the case of the shortest edge of at 10 K, a bulk contribution of 2 μS was subtracted.

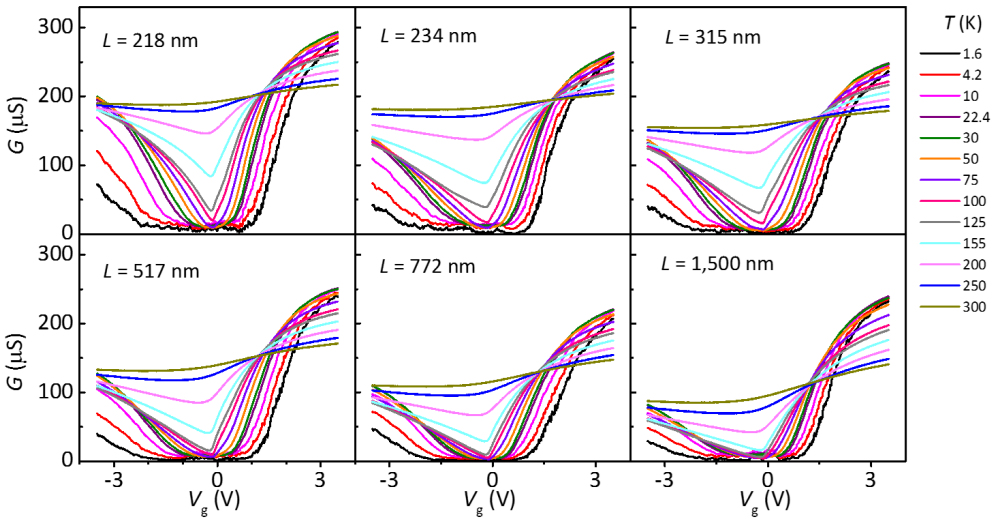

Figure C.1: Temperature dependence of transfer characteristics of different edges (adjacent contact pairs) in monolayer device MW1, with contact separation L ranging from 218 to 1,500 nm.

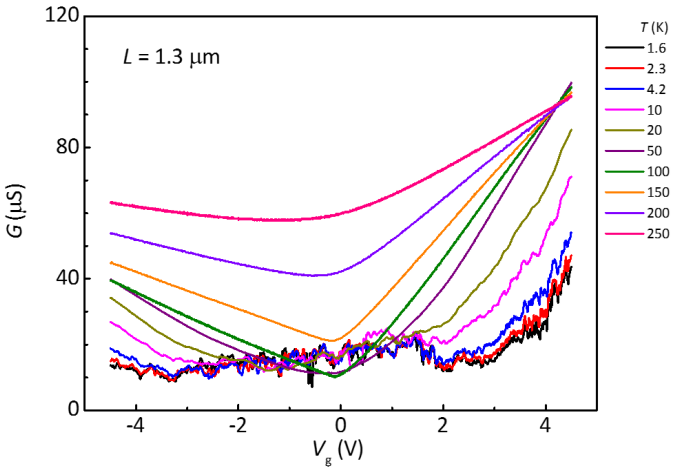

Figure C.2: Temperature dependence of the transfer characteristic of a particular edge in monolayer device MW2. The contact separation is 1.3 m.

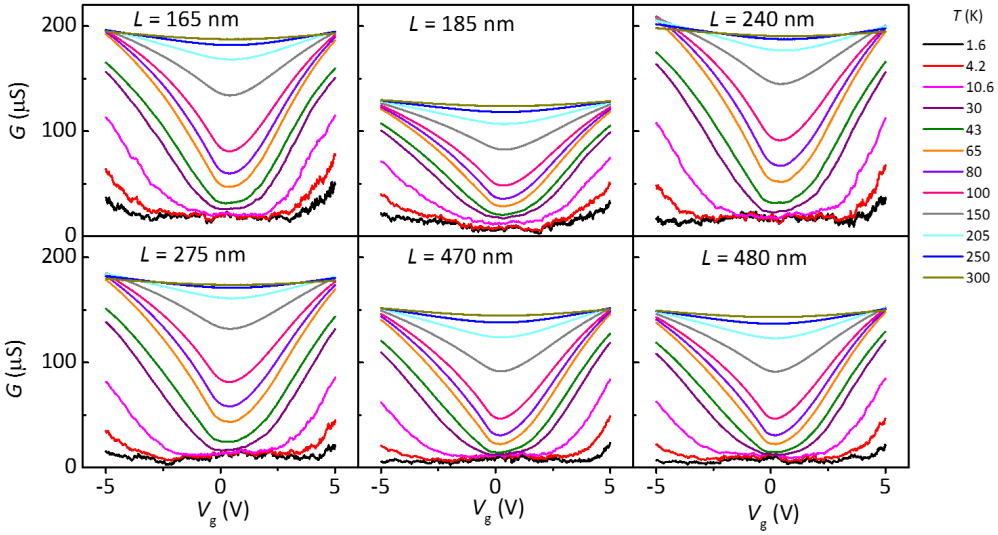

Figure C.3: Temperature dependence of transfer characteristics of different edges in monolayer device MW3, with contact separation L ranging from 165 to 480 nm.

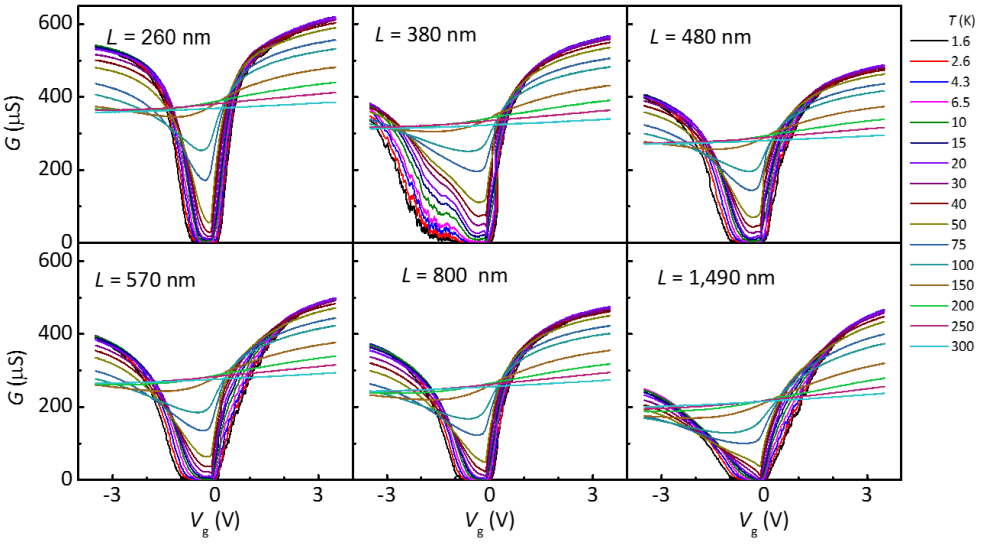

Figure C.4: Temperature dependence of transfer characteristics of different edges in bilayer device BW1, with contact separation L ranging from 260 to 1,490 nm.

VITA

Zaiyao Fei was Born in Maanshan, Anhui, China. He earned his Bachelor degree in Physics from University of Science and Technology of China in 2011. Then he joined the Physics department of University of Washington in Seattle, perusing his Ph.D degree in condensed matter experiment under the advising of Prof. David Cobden.